UC Riverside
UC Riverside Electronic Theses and Dissertations

Title
Analysis and Application of Silicon Nano-Particles Produced via Continuous Flow Non-Thermal Plasmas

Permalink
https://escholarship.org/uc/item/9bh3r2s8

Author
Lopez, Thomas David

Publication Date
2015

Peer reviewed|Thesis/dissertation

eScholarship.org Powered by the California Digital Library
University of California

UNIVERSITY OF CALIFORNIA
RIVERSIDE

Analysis and Application of Silicon Nano-Particles Produced via Continuous Flow Non-Thermal Plasmas

A Dissertation submitted in partial satisfaction
of the requirements for the degree of

Doctor of Philosophy

in

Mechanical Engineering

by

Thomas David Lopez

December 2015

Dissertation Committee:
Dr. Lorenzo Mangolini, Chairperson
Dr. Javier Garay
Dr. Phillip Christopher

Copyright by
Thomas David Lopez
December 2015

The Dissertation of Thomas David Lopez is approved:

____

____

____

Committee Chairperson

University of California, Riverside

Acknowledgements

The discussions and arguments that have shaped the way I look at the physical world, could not have happened, if the teachers of my past would not have been inspirational. I would like to thank Larry Cannon and Mark Dockin two high school teachers who were phenomenal at their jobs and a big inspiration to myself. Ben Stottrup, the best and worst undergraduate advisor one could possibly want, Rebekah Dupont and Dixie Schaffer who both have a talent for seeking out all who are talented. The only thing I can say to all of you is thank you for your continued support and inspiration that has allowed me to project myself to a place I never thought was possible.

I would like to thank my family: Mom, Dad, Jessica, Daniel, Taylor, Romelio and recently Lillian, for their support throughout the last 4 years and their continued confidence. It has been hard to be away from all of you, but at the same time it hasn't been too bad!

I would like to thank my advisor Professor Lorenzo Mangolini for his continued guidance and support, which none of this would have been possible without.

To Patrick Davis , Ozgul Yasar-Inceoglu, Lanlan Zhong, Stephen Exarhos, Michal Rieke , Alexis Penaloza, Alejandro Alaverez, Josh Rightnar, Devin Coleman, and Austin Woodward, I thank all of you for everything you have helped me with through the past years. I can give too many examples of times that any one of you has helped me out, I would like to say thanks for everything.

I would also like to recognize the research group at the Radio-Isotope Thermoelectric Research facility at the Jet Propulsion Laboratory in Pasadena fro all of their help and guidance; Dr. Sabah Bux, Dr. Jean-Pierre Fleurial, Dr. Jennifer Ni, George Nakatsukasa, and Gregory Gerig.

I dedicate my dissertation to Romelio Love;

As he once said “Look I’m doing science!”

And my family

ABSTRACT OF THE DISSERTATION

Analysis and Application of Silicon Nano-Particles Produced via Continuous Flow Non-Thermal Plasmas

by

Thomas David Lopez

Doctor of Philosophy, Graduate Program in Mechanical Engineering
University of California, Riverside, December 2015
Dr. Lorenzo Mangolini, Chairperson

Continuous flow non-thermal plasma reactors are being investigated for their ability to efficiently produce high quality nanoparticles. While many nanomaterials can be produced via continuous flow non-thermal plasma reactors, silicon is of particular interest, due to its abundance and relevance in many energy related fields. Significant gaps still exist in the understanding of the kinetics responsible for particle growth, structural evolution, and surface termination of continuous flow non-thermal plasma reactor produced particles. Particle interaction with plasma radicals results in the heating of the particles, which in turn affects the kinetics of particle growth, structural evolution, and surface termination during synthesis and processing. We have investigated the details of plasma-nanoparticle interaction by using in-flight and in-situ characterization

techniques. For the first time, we have measured the temperature of a free-standing particle immersed in a non-equilibrium processing plasma.

In parallel, we have utilized continuous flow non-thermal plasma reactor-produced nanoparticles to create bulk nanostructured materials. The ability to tune size, structure, and surface termination of the continuous flow non-thermal plasma reactor produced nanoparticles allows for significant control of the precursor powders used in the densification processes. Hot pressing processes allow for the production of samples with bulk-like densities while limiting grain growth, allowing for the creation of nanostructured bulk systems. Nanostructured bulk silicon represents an ideal system to study the role of nano-structuring on transport of charge carriers and phonons in bulk materials. Initial results show that small particle and narrow particle size distributions allows for the creation of bulk nanostructured silicon with high ZT values. This system has shown to be relevant for direct conversion of heat into electrical power, but is also a model for the optimization of phonon and charge carrier transport in similar material systems.

Table of Contents

Chapter 1 Overview

1.1 Introduction……1
1.2 Size……5
1.3 Structure……7
1.4 Surface termination……9
1.5 Particle heating due to particle surface termination……11
1.6 Bulk nanostructured systems……14
1.7 Scope of dissertation……17
1.7.1 Continuous flow nonthermal plasma reactors……17
1.7.2 Application of densified as produced silicon nanoparticles……18
1.8 References……19

Chapter 2: Low Activation Energy for the Crystallization of Amorphous silicon nanoparticles

2.1 Abstract……22
2.2 Introduction……23
2.3 Experimental Setup……25
2.4 Results……27
2.5 Discussion……46
2.5.1 Role of hydrogen……48
2.5.2 Particle agglomeration and coalescence……50
2.5.3Crystallization of amorphous silicon nanoparticles……52
2.5.4 Production of nanocrystals in non-thermal plasmas……53
2.6 Conclusion……54
2.7 Acknowledgements……55
2.8 References ……56

Chapter 3: On the nucleation and crystallization of nanoparticles in continuous flow non-thermal plasma reactors

3.1 Abstract…… 60
3.2 Introduction……62
3.3 Experimental setup……64
3.4 Results……67
3.5Disscussion……77
3.6 Conclusions……90
3.7 Acknowledgements……91
3.8 References ……92

Chapter 4: Thermal effects in the non-thermal plasma processing of nanoparticles

4.1 Abstract……95
4.2 Introduction……96
4.3 Experimental……97
4.4 Results and discussion……100
4.5 Conclusions……114
4.6 Reference……115

Chapter 5: Application of continuous flow non-thermal plasma produced particles for thermoelectric application

5.1 Abstract……117
5.2 Introduction……118
5.3 Experimental setup and procedures……120
5.3.1 Plasma process parameters……120
5.3.2 Powder processing……125
5.3.3 Dye preparation……127
5.4 Results……131
5.4.1 Doping……131
5.4.2 Thermal Conductivity……136
5.4.3 Figure of merit (ZT)……140
5.5 Preliminary structural results……142
5.6 Conclusion……144
5.7 References……145

Chapter 6 Conclusions and future works

6.1 Conclusions……147
6.1.1 Continuous flow non-thermal plasma reactors……147
6.1.2 Nanostructured bulk silicon systems……149
6.2 Future works……150
6.2.1 Continuous flow non-thermal plasma reactors……150
6.2.2 Nanostructured bulk silicon systems……151

Appendix A

A.1. Supplemental figures for chapter 2……153
A.2. Supplemental equations with explanations for chapter 2……162

List of figures

Chapter 1

1.1 **(a)** non thermal dusty plasma in parallel plate configuration [11] **(b)** Continous flow non thermal plasma reactor with argon silane hydrogen precusor gases........3

1.2 Average primary particle size as a function of the residence time and silane partial pressure. [9]..6

1.3 Dependence of ratio of $A_c/(A_c + A_a)$ on electrical power input for material produced using either silane or silicon tetrachloride as precursor. A_c and A_a are respectively the area of the peaks corresponding to the crystalline and amorphous signals in the Raman spectra. The ratio is proportional to the fraction of the material with crystalline structure. [12]..8

1.4 Normalized integrated absorbance of the absorption at 2087 cm ' in the silicon-hydrogen stretching region and the absorption at 910cm assigned to the silicon dihydride scissors mode as a function of annealing temperatures [25].................10

1.5 Heating and cooling events occurring on the silicon nanoparticle surface. Heating events are indicated with red dots on the nanoparticle surface while cooling events are shown as blue dots. The electron–ion recombination energy is equal to the argon ionization potential of 15.76 eV. Dangling bond passivation, hydrogen abstraction and hydrogen recombination deliver 3.1 eV, 1.41 eV and 4.5 eV, respectively. Cooling occurs mainly through collisions with colder gas atoms. At 900K and higher, thermal desorption of hydrogen starts to play a role, where the energy loss is equal to 1.69 eV for each desorbed hydrogen molecule. [26]........12

1.6 Excess temperature with respect to the background gas for 2 (top), 3(middle), and 10 nm(bottom) silicon nanoparticles [1]...13

1.7 Lattice thermal conductivity of ''nano-bulk'' Si (filled circles) is compared to a model for a single-crystal Si doped at similar carrier concentration (open diamonds). A calculated 90% reduction in thermal conductivity is represented by open squares. This corresponds to that of the ''nano-bulk'' Si. As a comparison, the lattice thermal conductivity of Si80Ge20 (filled triangles) is shown, demonstrating that nanostructuring can achieve significant reductions in the lattice thermal conductivity that rivals traditional point-defect methods of reduction. [27]..16

Chapter 2

2.1 (a) Bright field image of particle annealed in flight at a temperature of 720 C. Particles were collected onto a lacey carbon grid placed in the system exhaust line. (b) Dark field of (a), indicating a partial degree of crystallinity, as confirmed by the diffraction pattern in the inset showing the signal from the [111], [220] and [311] planes. (c) Bright field for particles annealed at 790 C. (d) Dark field of (c), indicating higher degree of crystallinity. This conclusion is supported by the

diffraction pattern in the inset, which show sharper features compared to that of the particles annealed at 720 C……………………………………………………………………28
2.2 Change in the Raman (a) and XRD (b) spectra for silicon nanoparticles produced under the conditions of 'sample A' (see Table 2.1), as a function of in-flight annealing temperature……………………………………………………………………………31
2.3 Fitting of the Raman data for sample A (see Table 2.1), annealed in flight at 760 C, using a variety of fitting models……………………………………………………………35
2.4 (a) Crystalline fraction measured using XRD and Raman measurements as a function of in-flight annealing temperature. The results from a variety of Raman fitting procedures are reported. (b) Plot of the logarithm of the crystalline fraction versus the inverse temperature in Kelvin (Arrhenius plot) for the data shown in (a)………………………………………………………………………………………………………37
2.5 Variation of the crystalline fraction, as measured using Raman data and the RWL model to predict the scattering from the crystalline phase, as a function of in-flight annealing temperature for three different particles sizes, produced under the conditions summarized in Table 2.1……………………………………………………………41
2.6 (a) Logarithm of the crystalline fraction xc (calculated from Raman data using the RWL peak profile for the crystalline peak) against inverse temperature for the particles produced under the condition for sample A (see Table 1), at three different pressures in the annealing stage. (b) Same as (a) normalized over the residence time in the high-temperature zone…………………………………………………44

Chapter 3

3.1 (a) Schematic of apparatus used for the sampling of particles at different positions along the plasma reactor. (b) Schematic of apparatus for the in-situ FTIR characterization of the system…………………………………………………………………66
3.2 TEM micrographs with selected area diffraction patterns for silicon particles extracted at distances equal to (a) -5 cm, (b) 3.5 cm, and (c) 37.5 cm with respect to the centerline of the upstream electrode (0 cm)…………………………………………69
3.3 Raman spectra for particles extracted from the plasma at (a) x=-50mm, (b) x=35 mm, and (c) x= 375 mm with respect of the upstream electrode. These positions correspond to the samples shown in Fig. 2……………………………………………………72
3.4 Particle size distribution for particles extracted from the plasma at (a) x=- 5 cm, (b) x= 3.5 cm, and (c) x = 37.5 cm with respect to the upstream electrode. The size distributions are based on the analysis of TEM micrographs……………………………74
3.5 FTIR for silane (first spectrum, collected upstream of the plasma volume) and for the positions as (a) x=-50mm, (b) x=35 mm, and (c) x= 375mm with respect of the upstream electrode…………………………………………………………………………………76
3.6 (a) Normalized absorption from SiH4 along the plasma reactor. (b) Average particle size along the plasma reactor, determined from the analysis of TEM

micrographs. (c) Fraction of the Raman spectroscopy intensity due to the silicon crystalline phase over the total Raman spectroscopy signal, determined by fitting the spectra with both the RWL and the three-peaks method (see text for details). The narrow bands indicate the position of the electrodes and the wider band indicates the distance over which the plasma extends by naked eye……………….79

3.7 FTIR spectra in the 1900-2500 cm^{-1} range sampling at (a) x= 5.5 cm, i.e., inside the plasma and at (b) x= = 32.5 cm, downstream of the plasma……………………………..87

Chapter 4

4.1 Schematic of reactor used for the *in-flight in-situ* characterization of silicon nanoparticles……………………………………………………………………………………………99

4.2 In-flight IR absorbance spectrum for silicon nanoparticles without plasma in the second reactor…………………………………………………………………………………………..102

4.3 2100 cm-1 (SiHx) peak intensity at increasing second plasma power……………….103

4.4 Integral absorbance from the 2100 cm-1 peak as a function of second plasma power, for the in-flight case and for the case of particles collected onto a filter placed in the second plasma……………………………………………………………………………106

4.5 Fractional hydrogen surface coverage on a silicon surface as a function of substrate temperature and for different values of atomic hydrogen density in the gas phase…………………………………………………………………………………………………..108

4.6 Measured atomic hydrogen density in the second plasma as a function of input power, for different values of parameter T_e (electron temperature)……………….111

4.7 Nanoparticle temperature as a function of plasma power density…………………..113

Chapter 5

5.1 Scaled up plasma reactor capable of producing 100's of milligrams an hour, plasma reactor control structure of particles from amorphous to crystalline, annealing furnace used to control hydrogen surface termination, collection point houses a stainless steel mesh filter between teo gate valves allowing for the transfer of particles under a controlled environment……………………………………………………122

5.2 Particle size distribution as a function of in-flight annealing temperature. The corresponding lines are Gaussian peak fits with the center depicted by an open triangle……………………………………………………………………………………………………..12

5.3 Hot press dye and sleeve schematic (A-bottom, F-top) blank graphite spacer, (B, E) grafoil sheet, (C, D) Graphite spacer with one side (facing the silicon particles) coated with boron nitride ………………………………………………………………………………128

5.4 Electrical resistivity as a function of temperature, with samples A-D and a calculated reference for single crystal silicon……………………………………………..132

5.5 Room temperature mobility versus carrier concentration………………………………133
5.6 Seebeck measurement as a function of temperature for samples A-D and a reference line of single crystal silicon………………………………………………………..135
5.7 Thermal conductivity as a function of temperature for samples A-D, Petermann [19], and Bux[6] ………………………………………………………………………………………..137
5.8 Lattice thermal conductivity as a function of temperature for samples A-D and Bux [6] ………..139
5.9 Figure of merit (ZT) as a function of temperature for samples A-D, Bux [6], and Ptermann[19] ………………………………………………………………………………………………141
5.10 (A) bright field TEM image showing crystallites ranging in size from 25-55 nm, (B) SEM image showing intergranular crack propagation with grains in the 100's of nm size range, (C) Scherrer first peak analysis from XRD data showing an estimated crystallite size as a function of in-flight annealing temperature………………………143

Chapter 6

6.1 Microstructure dependence on hot press maximum temperature…………………..152

Appendix A

A.1 (a) TEM micrograph of amorphous silicon particles produced under the conditions of 'sample A' (see Table 2.1) without any in-flight annealing. (b) Dark field micrograph of figure (a). (c) higher magnification micrograph for the sample, and (d) corresponding selected area diffraction (SAD) pattern. A lower magnification image was used to generate the diffraction pattern, so that a large number of particles interact with the electron beam. The combination of weak contrast in the dark field image, lack of fringes in the higher magnification image, and weak pattern in the SAD leads to conclude that the particle have an amorphous structure……………………………………………………………………………………………………153

A.2 (a) Raman scattering from samples produced under the conditions of 'sample A' (see table 2.1) without any in-flight annealing. (b) XRD for the same sample of (a). Both Raman and XRD data support the conclusion that the particles have an amorphous structure……………………………………………………………………………………154
A.3 Schematic of two phase reactor production parameters for the samples produced in this reactor are summarized in Table 2.1. (a) first stage allows for control of size and structure of produced particles (b) second stage annealing chamber with independently controlled temperature and annealing time……………………………155
A.4 Particle size distribution of Sample A at three different in-flight annealing temperatures………………………………………………………………………………………………156

A.5 Fitting of XRD data for the determination of the crystalline fraction. A five peaks procedure is used, with the center and width of the two peaks due to the amorphous phase determined using the XRD data for the sample that has not been annealed (see graph labeled as 'no annealing'). The five peaks fit is then performed by holding constant the position and width for the two peaks corresponding to the amorphous contribution, while fitting their amplitude together with that of the peaks arising from the crystalline structure. The crystalline fraction is quantified by calculating the ratio between the area under the three sharper peaks due to the crystalline structure (from the [111], [220] and [311] lattice planes) over the total area (area from the crystalline peaks summed with the area from the two amorphous features). The in-flight annealing temperatures are clearly labeled on the graphs……………………………………………157

A.6 (top) XRD data for sample produced and annealed under the condition of 'Sample A' (see Table 2.1), annealed at 800^0C. The curve fitted using Guassian profiles for each crystalline peak and for the peaks due to amorphous contribution. (bottom left) table with the crystalline peak position and their relative full width- half max (FWHM). (bottom right) Williamson- Hall Plot: a linear fit of the data has negligible slope (proportional to streee acting on the crystal)………………………………………158

A.7 (a) Bright-field TEM micrograph of particles produced under the conditions of 'sample A' (see Table 1) and annealed at 830�C. (b) Dark field micrograph corresponding to (a). (c) Higher magnification micrographs, fringes from the [111] lattice planes are clearly visible. (d) Selected-area diffraction pattern generated using a low-magnification image, so that a large number of particles interact with the electron beam. Rings from the [111], [220] and [311] lattice planes are clearly distinguishable. These images support the conclusion that a very large fraction of the particles have a crystalline structure……………………………………………………159

A.8 Arrhenius plot based on the data of figure 5. The activation energy for crystallization is 1 eV for the smaller particle size ranges (see table 2.1), and rapidly increases to 7.5 eV and 9.6 eV for increasingly larger sizes……………………………160

A.9 (top) FTIR absorbance from the plasma produced silicon nanoparticles, produced under the conditions of 'sample A' (see table 2.1) and without any in-flight annealing, as measured *in-situ* before air exposure. (bottom) Variation of the area under the ~2100 cm^{-1} peak, the ~630 cm^{-1} peak and the 800-900 cm^{-1}peaks with respect of the in-flight annealing temperature. The ~2100 cm^{-1} and the ~630 cm^{-1} peaks arise from SiH_x vibrational modes (x=1,2,3) while the 800-900 cm^{-1} peaks arise from SiH_2 and SiH_3 wag and scissor mode. Signal from the 800-900 cm^{-1} peaks diminishes faster than the signal from the ~2100 cm^{-1} and the ~630 cm^{-1} peaks, because of the lower thermal stability of higher surface hydrides…………………..161

List of Tables

Chapter 2

2.1 Summary of process parameters for the samples discussed in this contribution. Samples A, B, and C correspond to three different initial particle sizes produced by varying the residence time in the plasma reactor. The particle size listed at the exit of the tube furnace shows an increase due to particle agglomeration and coalescence……………………………………………………………………………………29

2.2 Activation energies for crystallization obtained using the data shown in Fig. 2.4. The residual and R-squared (R^2) for the fitting of the Raman data with various procedures are also reported………………………………………………………………39

Chapter 5

5.1 In-flight and hot press conditions of CFNTPR produced silicon nanoparticles…130

Chapter 1 Overview

1.1 Introduction

Plasma is defined as one of the four states of matter. Plasmas have properties that are not found in any of the other states of matter. By general definition matter is considered to be in a plasma state when there is a collection of positive and negative charged particles along with neutrals in a particular volume whose overall net charge is considered zero. Energy is readily transferred between particles within the plasma, in some cases this energy exchange reveals itself to the naked eye as light. Other phenomena occurring within the plasma that cannot be readily observed by the naked eye are the breakdown of molecular bonds, ionization, and recombination [1], to name a few. This seemingly hostile environment allows for many types of chemical and physical phenomenon to take place. This makes plasmas a unique and interesting state of matter to observe.

Plasmas can be generated in many different ways and in turn can have many different physical and chemical phenomena associated with them. One example of this is lightning. Lightning is an electrostatic plasma discharge that is created by charged species in a storm cloud. Once the electrostatic charge reaches a certain potential it will strike, discharging either to itself (cloud) or the ground [2]. Lightning discharges are comprised of positively or negatively charged species carrying a current as high as 120 kA,500 mega

joules of energy[3], and create massive amounts of light. Another example of plasma is a neon light. Other examples of plasmas include microwave and radio frequency (RF) plasmas. Microwave and RF plasmas utilize the high frequency power inputs to strike and maintain plasmas, they are used for many material processing applications; microwave plasma enhanced chemical vapor deposition (MPECVD)[4-6], plasma enhanced chemical vapor deposition (PECVD) [7-9],and nano particle synthesis [9,10], to name a few.

Figure 1.1a shows a non-thermal RF plasma in a parallel plate configuration. This particular plasma is consider a dusty plasma, i.e. nanoparticles are being produced in the discharge and thus refract light that is generated by the plasma[11]. Although particle nucleation within a plasma is not optimal for applications such as thin film growth, the optimization of these types of systems for the production of nanoparticles is of interest for its ability to create high yields of high quality nanoparticles[9,12-14]. These optimized systems have shown the ability to create high quality nanoparticles of germanium[15], copper sulfide[16], and carbon diamond[17].

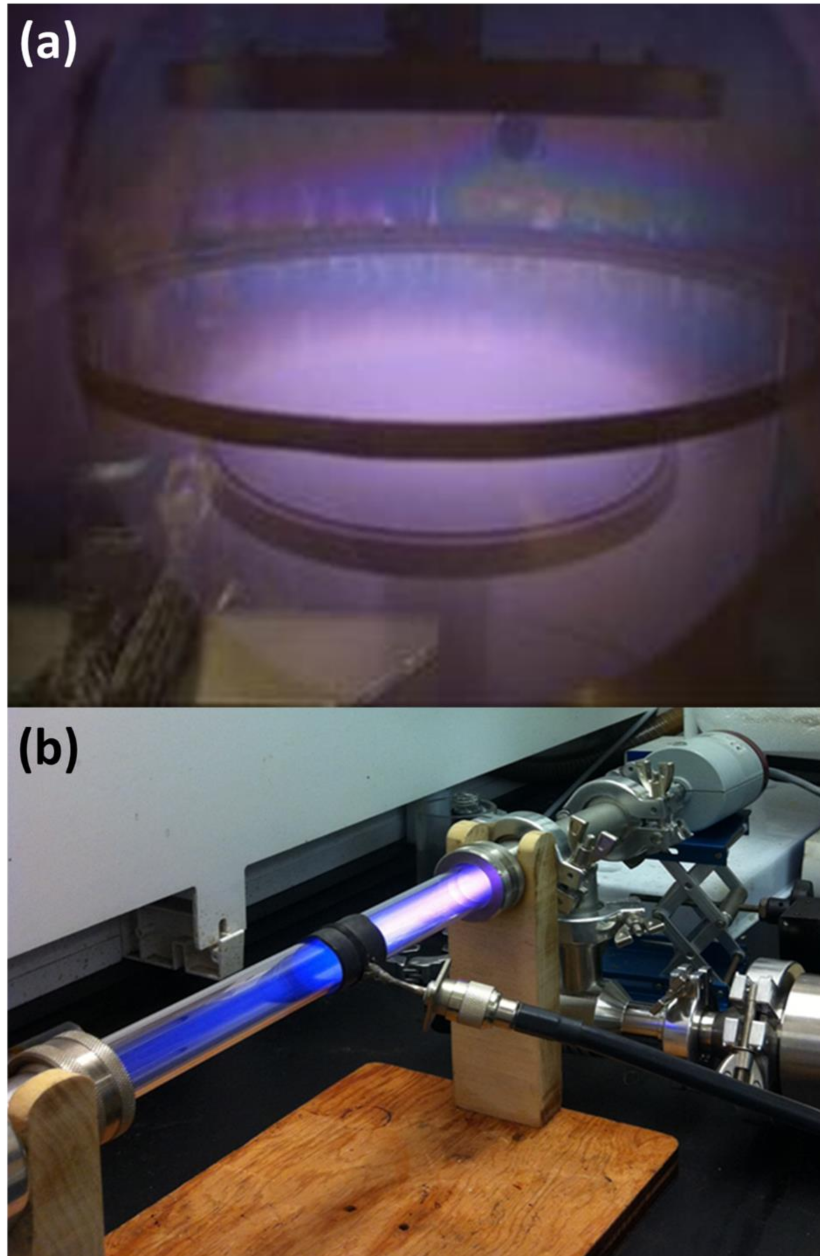

Figure 1.1 (a) non thermal dusty plasma in parallel plate configuration [11] (b) Continous flow non thermal plasma reactor with argon silane hydrogen precusor gases

One type of these optimized reactors is shown in Figure 1.1b, a continuous flow nonthermal plasma reactor (CFNTPR). This particular reactor utilizes a 13.56 MHz RF power generator to strike and maintain, in this case, an argon-silane-hydrogen plasma capable of creating high quality silicon nanoparticles. CFNTPRs have the ability to control size [9], structure [12], and surface termination [18, 19], based completely on process parameters.

The process parameters optimized for the production of nanoparticles via CFNTPRs has led to significant advances in many material systems including, the use of nano silicon for battery research[20], high efficiency solar cells[21], and other nano-device applications[22]. Although these significant material system advances have been made, the kinetics responsible for nucleation, growth, and structural evolution, is still not fully understood. The purpose of this dissertation is to extend the understanding of the physical and chemical kinetics responsible for the production of nanoparticles via CFNTPRs.

A Secondary study of nanostructured bulk silicon systems utilizing CFNTPR produced nanopowers as precursor materials for the study of transport phenomenon. Nanostructured bulk silicon represents an ideal system to study the role of nano-structuring on transport of charge carriers and phonons in bulk materials. This is relevant for many applications including, the direct conversion of heat into electrical power.

1.2 Size

CFNTPRs are unique in the fact that particle nucleation, growth, and structural changes all occur on a time scale of ~100 milliseconds. Particles made in non-thermal plasmas can range in size from a couple of nanometers [1, 9, 12] up to a couple of 100 of nanometers [23]. The growth kinetics in a non-thermal plasma is dependent on two factors: 1. Precursor partial pressure, 2. Residence time spent in the plasma. As these two parameters can be readily controlled particles produced in CFNTPRs can be made at any desired size within this range, as shown in figure 1.2.

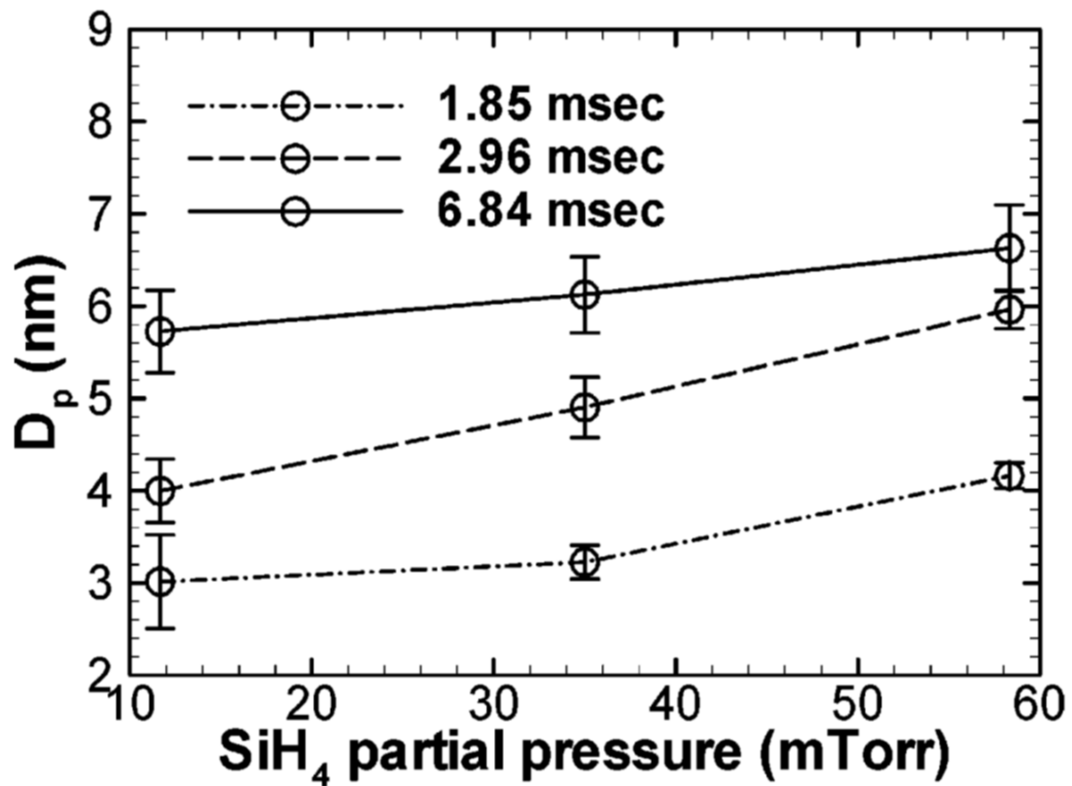

Figure 1.2 Average primary particle size as a function of the residence time and silane partial pressure. [9]

1.3 Structure

Nanoparticles produced via CFNTPRs have many applications, batteries [20], solar cells [21], LEDs [22],. Based on the application, structure can play a crucial role for the inherent properties of materials that are utilized. For example, amorphous silicon is used as a light trap in thin film solar cells [21]. The reasoning behind this is the absorption coefficient of amorphous silicon is larger compared to that of crystalline silicon allowing for a broader absorption range for silicon solar cells making them more efficient [24]. As shown by Ozgul et. al.[12], figure 1.3, CFNTPRs utilizing silicon precursors, silane (SiH_4) and silicon tetrachloride ($SiCl_4$), can produce amorphous to crystalline structures based on plasma power input. The structure of silicon nanoparticles can readily be produced to the structure of choice whether amorphous or crystalline, and any nominal fraction mixtures in-between. The result shown in figure 1.3 speaks to the controllability of CFNTPRs over structure as function of input parameters, in this case input power.

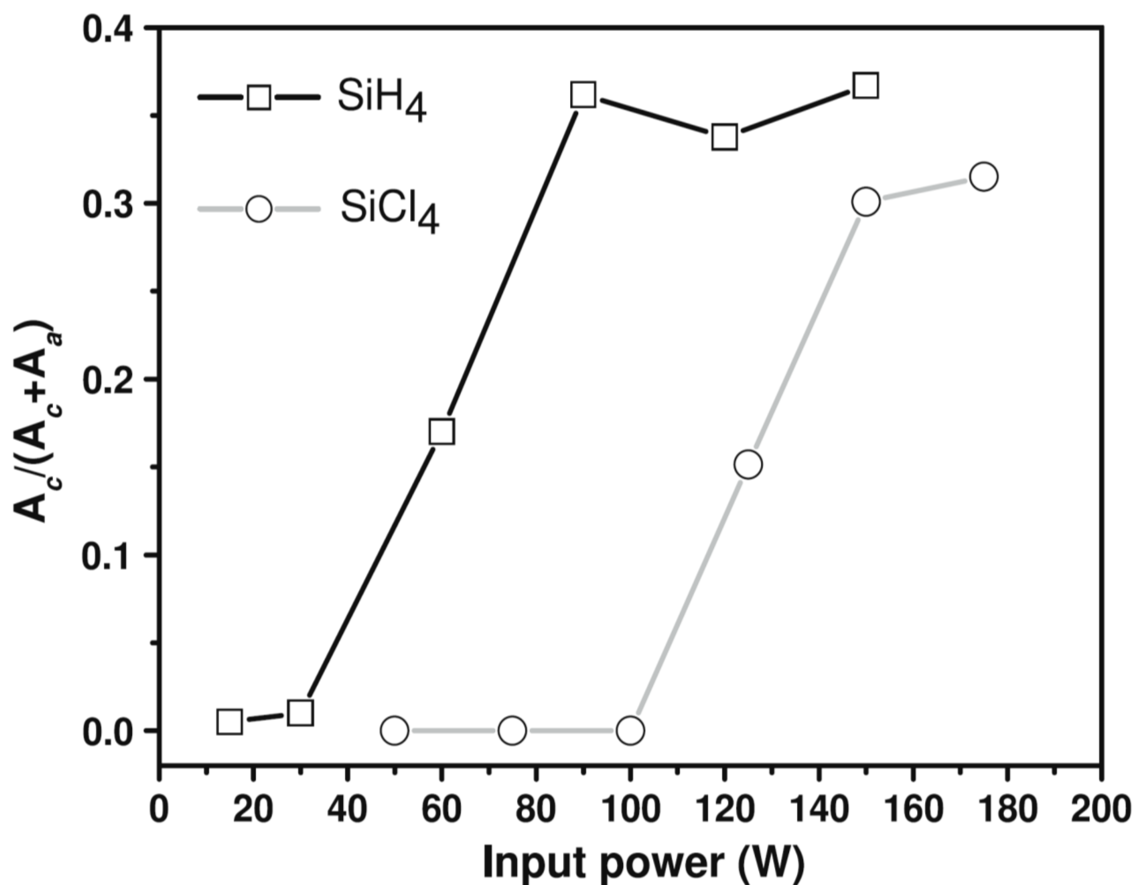

Figure 1.3 Dependence of ratio of $A_c/(A_c + A_a)$ on electrical power input for material produced using either silane or silicon tetrachloride as precursor. A_c and A_a are respectively the area of the peaks corresponding to the crystalline and amorphous signals in the Raman spectra. The ratio is proportional to the fraction of the material with crystalline structure. [12]

1.4 Surface termination

For the sake of the experiments presented in the following, a combination of argon, hydrogen, and silane gases are utilized. Using silane as the precursor gas in this system, the produced particles have a hydrogen surface termination [1, 9]. Surface termination plays a role in the chemistry that can be carried out on the surface of the particle whether carried out in the plasma or post-production [1, 12, 18]. Hydrogen termination of silicon is stable in ambient environments but is prone to oxidation within minutes [12]. In a controlled atmosphere the surface termination is stable and shows a dependence on temperature. Figure 1.4 shows the results of an annealing study carried out by Grupta et. Al., [25]. A piece of hydrogen terminated porous silicon was heated to different temperatures while IR absorbance measurements were made. The results show a decrease in hydrogen termination with an increase in temperature. Surface termination of nanoparticles produced via CFNTPRs can be tuned by precursor choice[12], secondary plasma processing[1,12,18], and post production annealing[24] for desired applications.

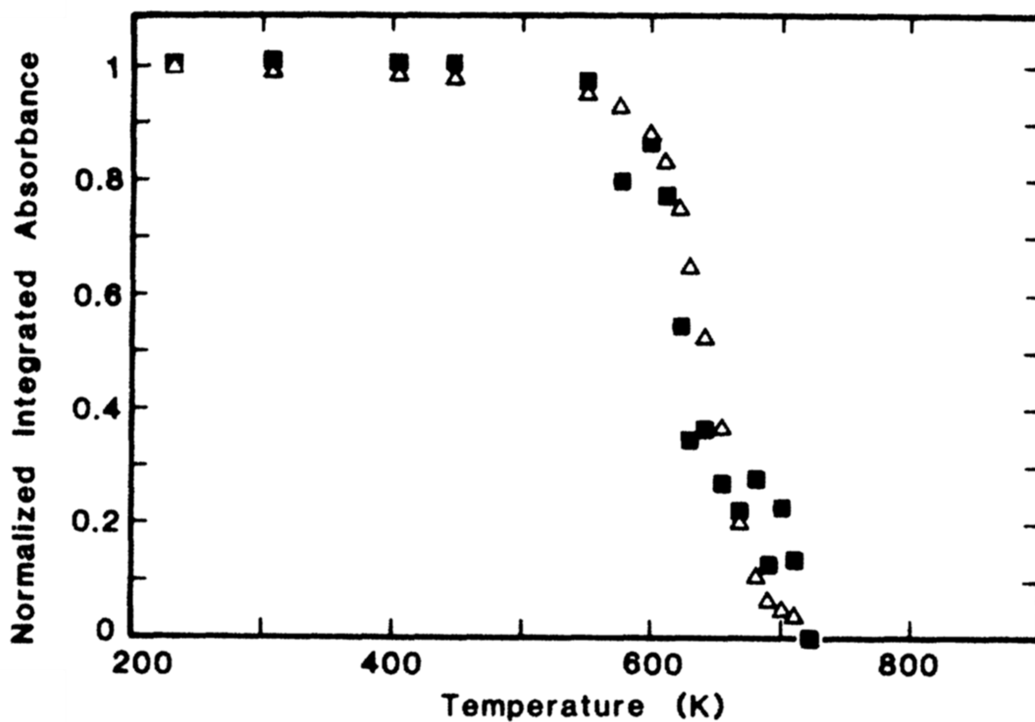

Figure 1.4 Normalized integrated absorbance of the absorption at 2087 cm ' in the silicon-hydrogen stretching region and the absorption at 910cm assigned to the silicon dihydride scissors mode as a function of annealing temperatures [25]

1.5 Particle heating due to particle surface interaction

CFNTPRs utilizing a mixture of argon, hydrogen, and silane gases to create the plasmas and the power inputs being used, particle surface interactions with elemental hydrogen, free radicals, and ions, can contribute to an increase in particle temperature [1]. Energies associated with these interactions are shown in Figure 1.5, taken from Kramer et. al. [26]. It has been theorized that the interactions occurring on the surface of the silicon particles cause the particles to heat up and achieve temperatures well above those of their surrounding carrier gases, which are assumed to be at or close to room temperature [1,26]. Figure 1.6 shows the results of a numerical model that is taking in to account these interactions. The numerical model presented by Mangolini et. al. [1], utilizes a Monte Carlo simulation that allows for the input of multiple parameters to simulate the plasma species the particles are interacting with. These parameters include particle size and carrier gas temperature. Ion and elemental hydrogen interaction are taken into account using probability distribution functions. Utilizing the probability of these interaction a simulation of surface interactions on the same time scale, ~100 milliseconds, that a particle is exposed to in a CFNTPR is possible. The results show that particles have the ability to well exceed the background temperature of the carrier gas, due to surface interaction alone.

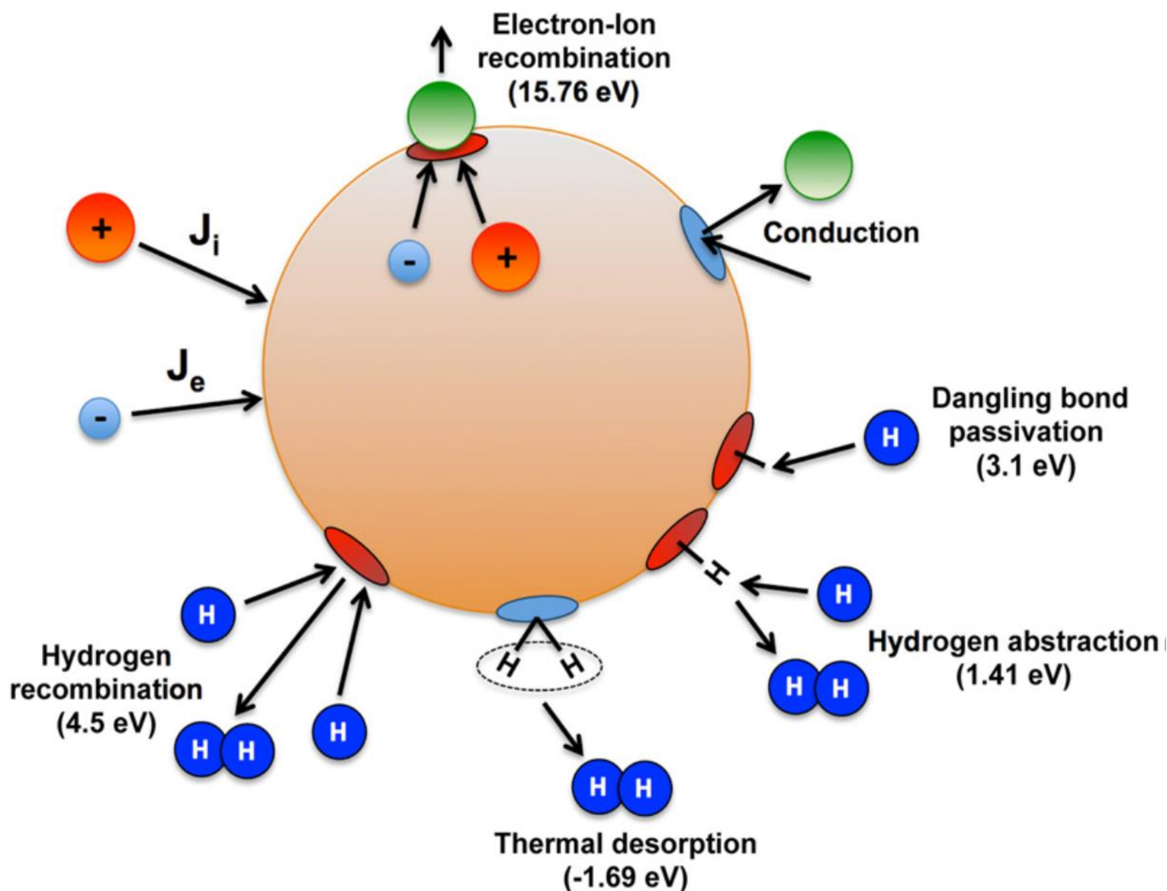

Figure 1.5 Heating and cooling events occurring on the silicon nanoparticle surface. Heating events are indicated with red dots on the nanoparticle surface while cooling events are shown as blue dots. The electron–ion recombination energy is equal to the argon ionization potential of 15.76 eV. Dangling bond passivation, hydrogen abstraction and hydrogen recombination deliver 3.1 eV, 1.41 eV and 4.5 eV, respectively. Cooling occurs mainly through collisions with colder gas atoms. At 900K and higher, thermal desorption of hydrogen starts to play a role, where the energy loss is equal to 1.69 eV for each desorbed hydrogen molecule. [26]

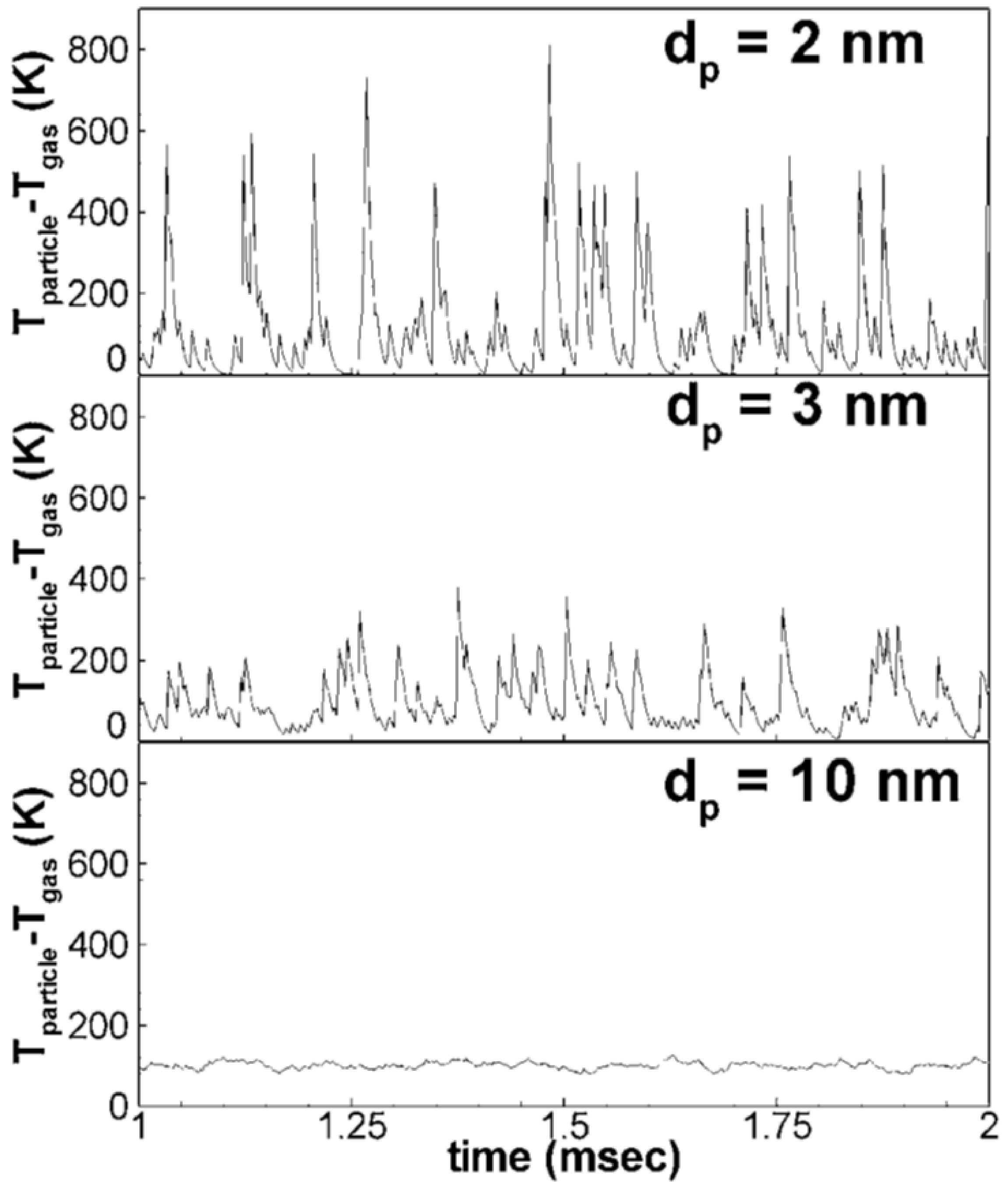

Figure 1.6 Excess temperature with respect to the background gas for 2 (top), (middle), and 10 nm(bottom) silicon nanoparticles [1]

1.6 Bulk nanostructured systems

As shown above, CFNTPRs have the capability to produce silicon nanoparticles with control of size, structure, and surface termination. In particular CFNTPR have the ability to create specific size ranges of amorphous or crystalline silicon nano particles that are hydrogen or chlorine terminated [1,9,12]. Using these particles as precursor powders for densification processes allows for the creation of a nanostructured bulk system. Silicon nanostructured bulk systems created from CFNTPR powders gives the capability to have control over the nanostructure of the bulk systems that are created.

It has been shown that phonon scattering occurs at grain boundaries and mismatch interfaces [27]. Bux et. al. has also shown that silicon under the correct processing parameters have the ability to reach high ZT values for thermoelectric applications. The increased ZT value was due to a 90% decrease in lattice thermal conductivity, see figure 1.7, due to phonon scattering at grain boundaries and crystallite interfaces. Bux et. al. reports a crystallite size range of 5-20nm for precursor powders and an average grain size of 75 nm samples. Simply stated the more interfacial boundaries, i.e. crystallites or grains, causes a decrease in thermal transport, leading a more efficient phonon scattering system. By utilizing CFNTPR produced particles it is possible to create a nanostructured bulk system from silicon nanoparticles that would have many more scattering points due to the number of small particles that would make up the system. Petermann et. al [28], also shows the same affects. Petermann utilizes

microwave plasma produced silicon nanoparticles as a precursor for thermoelectric applications. An in depth dicussion of Bux and Pettermann's finding in comparison with the preliminary results from CFNTPR produced precursor for nanostructured bulk systems will be given in chapter 5. Figure 1.7 shows the resulting ZT values for the samples produced by Bux and Petermann. Bux[27] currently posts the highest measure ZT for silicon and Petermann[28] is in a close second]. Based on these results a system utilizing a particle production system that has more control over particle size distributions, structure, and surface termination, it could be possible to tune the phonon scattering mechanisms within a nanostructured bulk system.

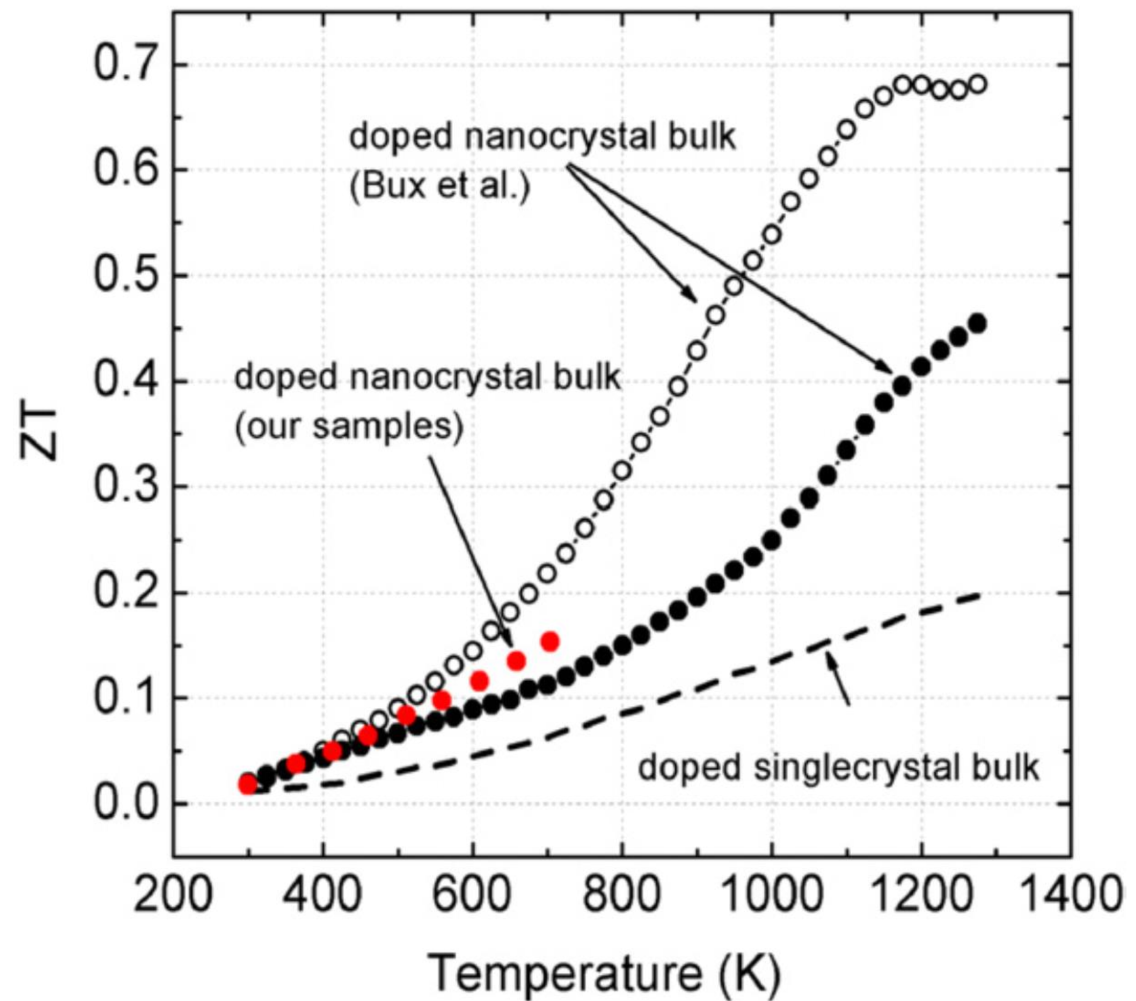

Figure 1.7 Plot reproduced from Petermann et al.[28]. Comparison of ZT values for single crystal doped silicon and two of the top published ZT values. Black open and closed circles represent the bulk processing of silicon samples produced by Bux[27], and the red circles represent the plasma synthesized field assisted sintering findings of Petermann et al.[28]

1.7 Scope of Dissertation

1.7.1 Continuous flow nonthermal plasma reactors

A report on the interaction of plasma produced particles and how plasma input parameters affect size, structure, and surface termination will be discussed in depth. There are three main objectives: First, determine activation energy for CFNTPR produced amorphous nano silicon based on a purely thermal process. Second, track the evolution of particles in CFNTPRs by: consumption of precursor, nucleation of particles, particle growth, and structural changes of particles, all as a function of their position within a plasma. Third, empirically measure the temperature of a particle is able to reach while in a CFNTPR as a function of plasma input power.

1.7.2 Application of densified as produced silicon nanoparticles

An overview of particle production, preparation, and densification procedures will be shown. Analysis of densified samples and their measured properties; thermal conductivity, electrical resistivity, Seebeck, along with calculated figure of merit, ZT values. The overall affect CFNTPR produced particles have on densification processes, ZT values, and preliminary structural outcomes will be discussed.

1.8 References:

1. Mangolini, Lorenzo, and Uwe Kortshagen. "Selective nanoparticle heating: Another form of nonequilibrium in dusty plasmas." *Physical Review E* 79.2 (2009): 026405.Saunders, C. P. R. "A review of thunderstorm electrification processes."*Journal of Applied Meteorology* 32.4 (1993): 642-655.

2. Hasbrouck, Richard. "Mitigating lightning hazards." *Science and Technology Review* (1996).

3. Choi, Won Seok, et al. "Effect of hydrogen plasma pretreatment on growth of carbon nanotubes by MPECVD." *Materials Science and Engineering: C* 26.5 (2006): 1211-1214.

4. Sung, S. L., et al. "The strengthening mechanism of DLC film on silicon by MPECVD." *Thin Solid Films* 315.1 (1998): 345-350.

5. Ye, Haitao, et al. "Nucleation and growth dynamics of diamond films by microwave plasma-enhanced chemical vapor deposition (MPECVD)." *Surface and Coatings Technology* 123.2 (2000): 129-133.

6. Meyyappan, Meyya, et al. "Carbon nanotube growth by PECVD: a review."*Plasma Sources Science and Technology* 12.2 (2003): 205.

7. Duerinckx, F., and J. Szlufcik. "Defect passivation of industrial multicrystalline solar cells based on PECVD silicon nitride." *Solar Energy Materials and Solar Cells* 72.1 (2002): 231-246.

8. Chang, Mei, et al. "Inlet manifold and methods for increasing gas dissociation and for PECVD of dielectric films." U.S. Patent No. 4,854,263. 8 Aug. 1989.

9. Mangolini, L., E. Thimsen, and U. Kortshagen. "High-yield plasma synthesis of luminescent silicon nanocrystals." *Nano letters* 5.4 (2005): 655-659.

10. Kortshagen, Uwe, et al. "Process and apparatus for forming nanoparticles using radiofrequency plasmas." U.S. Patent No. 8,016,944. 13 Sep. 2011.

11. http://www.ipe.ethz.ch/laboratories/ltr/research/index_EN (Image Figure 1.1a)

12. Yasar-Inceoglu, Ozgul, et al. "Silicon nanocrystal production through non-thermal plasma synthesis: a comparative study between silicon tetrachloride and silane precursors." *Nanotechnology* 23.25 (2012): 255604.

13. Gresback, Ryan, Tomohiro Nozaki, and Ken Okazaki. "Synthesis and oxidation of luminescent silicon nanocrystals from silicon tetrachloride by very high frequency nonthermal plasma." *Nanotechnology* 22.30 (2011): 305605.

14. Doğan, İlker, et al. "Ultrahigh throughput plasma processing of free standing silicon nanocrystals with lognormal size distribution." *Journal of Applied Physics* 113.13 (2013): 134306.

15. Gresback, Ryan, Zachary Holman, and Uwe Kortshagen. "Nonthermal plasma synthesis of size-controlled, monodisperse, freestanding germanium nanocrystals." *Applied Physics Letters* 91.9 (2007): 093119.

16. Thimsen, Elijah, Uwe R. Kortshagen, and Eray S. Aydil. "Plasma synthesis of stoichiometric Cu 2 S nanocrystals stabilized by oleylamine." *Chemical Communications* 50.61 (2014): 8346-8349.

17. Kumar, Ajay, et al. "Formation of nanodiamonds at near-ambient conditions via microplasma dissociation of ethanol vapour." *Nature communications* 4 (2013).

18. Mangolini, Lorenzo, and Uwe Kortshagen. "Plasma-Assisted Synthesis of Silicon Nanocrystal Inks." *Advanced Materials* 19.18 (2007): 2513-2519.

19. Mangolini, L., et al. "Plasma synthesis and liquid-phase surface passivation of brightly luminescent Si nanocrystals." *Journal of luminescence* 121.2 (2006): 327-334.

20. Zhong, Lanlan, Juchen Guo, and Lorenzo Mangolini. "A stable silicon anode based on the uniform dispersion of quantum dots in a polymer matrix." *Journal of Power Sources* 273 (2015): 638-644.

21. Zeman, M., et al. "Optical modeling of a-Si: H solar cells with rough interfaces: Effect of back contact and interface roughness." *Journal of Applied Physics*88.11 (2000): 6436-6443.

22. Oda, Shunri. "NeoSilicon materials and silicon nanodevices." *Materials Science and Engineering: B* 101.1 (2003): 19-23.

23. Boeuf, J. P. "Characteristics of a dusty nonthermal plasma from a particle-in-cell Monte Carlo simulation." *Physical Review A* 46.12 (1992): 7910.

24. Janai, M., et al. "Optical properties and structure of amorphous silicon films prepared by CVD." *Solar Energy Materials* 1.1 (1979): 11-27.

25. Gupta, P., V. L. Colvin, and S. M. George. "Hydrogen desorption kinetics from monohydride and dihydride species on silicon surfaces." *Physical Review B*37.14 (1988): 8234.

26. Kramer, N. J., et al. "Plasma-induced crystallization of silicon nanoparticles."*Journal of Physics D: Applied Physics* 47.7 (2014): 075202.

27. Bux, Sabah K., et al. "Nanostructured bulk silicon as an effective thermoelectric material." *Advanced Functional Materials* 19.15 (2009): 2445-2452.

28. Petermann, Nils, et al. "Plasma synthesis of nanostructures for improved thermoelectric properties." *Journal of Physics D: Applied Physics* 44.17 (2011): 174034.

Chapter 2

Low Activation Energy for the Crystallization of Amorphous Silicon Nanoparticles

2.1 Abstract

We have experimentally determined the crystallization rate of plasma produced amorphous silicon powder undergoing in-flight thermal annealing, and have found a significant reduction in the activation energy for crystallization compared to amorphous silicon thin films. This finding allows us to shed light onto the mechanism leading to the formation of high quality nanocrystals in non-thermal plasmas.

2.2 Introduction

Silicon nanoparticles have many interesting properties and relevant applications,[1] and have been successfully integrated in nanoelectronics,[2] light emitting devices[3,4] and photovoltaic devices.[5] They are excellent candidates for bio-related applications. [6,7] Nanostructures based on silicon are potentially compatible with large-scale applications, since silicon is the second most abundant element on Earth. Silicon nanoparticles have been produced using laser ablation of silicon targets,[8] pyrolysis of silane in tube furnaces,[9] laser pyrolysis of silane followed by electrochemical etching,[10,11] and finally using plasma reactors deliberately optimized for the production of nanoparticles.[12–15] Non-thermal plasma continuous flow reactors convert silane into silicon nanocrystals sufficiently small to show quantum confinement effects.[16] The particle structure can be tuned from amorphous to crystalline depending on the power input into the plasma (see Fig. 5 in ref. 17). This has important consequences on the particle optical properties,[18] which are critically important for many applications. Despite the fact that plasma-based techniques are promising candidates for the large volume synthesis of silicon nanocrystals, a detailed understanding of the correlation between plasma properties and nanoparticle structure is missing. The question remains of how the continuous flow reactor introduced in ref. 13 fully converts the silane precursor into particles with a crystalline structure within few milliseconds. Not only is the plasma–nanoparticle interaction complex,[19] but also the material system has not been characterized to the extent of, for instance, amorphous

silicon thin films. We address this issue by investigating the kinetics of crystallization of small amorphous silicon particles during thermal annealing.

2.3 Experimental Setup

We have developed a two-stage gas-phase reactor for the continuous production and in-flight annealing of silicon nanopowder. The first stage consists of a non-thermal plasma reactor analogous to the one described in ref. 13: a pair of ring electrodes are wrapped around a Pyrex tube and biased using a radio frequency (RF, 13.56 MHz) power supply. We use silane (1.37% in argon by volume) as silicon precursor. The discharge is sustained using a power of 10 watts, which is sufficiently low to avoid the formation of nanocrystals in the plasma and which results in the production of amorphous powder (see TEM micrographs in Appendix A, figure A.1, Raman and XRD data in figure A.2). An orifice separates the first and second stages of the reactor. Depending on the orifice size, the pressure in the plasma reactor is varied between 7.5 and 3.7 Torr. Since the total flow through the reactor is kept constant and equal to 100 standard cubic centimeters per minute (sccm), varying the pressure allows controlling the residence time in the plasma, which allows adjusting the nanoparticle size.[13] In addition, we also vary the diameter of the tube for the plasma reactor, with the same purpose of controlling the residence time. For the samples described in this paper, we control the synthesis parameters to obtain amorphous nanoparticles at the exit of the first stage with an average size of 4, 7 and 11 nm.

The second stage of the reactor consists of a 25.4 mm quartz tube placed inside a tube furnace with a heated length of 40 cm. The tube furnace temperature is precisely

controlled up to 1000 ^{0}C. An automatically controlled butterfly valve is placed downstream of the heating stage to adjust the pressure between 1 and 2 Torr, thus controlling the flight time through the furnace (i.e. the annealing time). Under these conditions the flow across the orifice is chocked, so that the particle synthesis and annealing conditions can be varied independently. The production parameters for the samples discussed in this paper are summarized in Table 2.1. This design allows us to (a) produce particles of varying sizes in the first stage and (b) independently control annealing temperature and annealing time in the second stage (see schematic Appendix A figure A.3). The particles are collected downstream of the tube furnace by filtering. A small part of the flow at the furnace exit is sampled and sent into a small six-way cross evacuated using a turbopump, where the particles are impacted onto a KBr target for *in situ* FTIR measurements.[17]

The particle size and structure is determined using transmission electron microscopy (TEM), X-ray diffraction (XRD) and Raman spectroscopy. A detailed description of the methodology used for the determination of the crystalline fraction and of the activation energy for crystallization is given in the following section.

2.4 Results

In figure 2.1 we show TEM micrographs of silicon nanoparticles produced using the conditions for ‘sample A’ in Table 2.1, and processed through the tube furnace at two different annealing temperatures, 720 ^{0}C and 790 ^{0}C. The particles are originally produced in the plasma with an amorphous structure, as confirmed by extensive Raman, XRD and TEM characterization (see Appendix A, figures A.1 and A.2). Bright field images in figures 2.1a and 2.1c, show that the particles are between 5 and 10 nm in size. Particle size distributions have been generated by analyzing several TEM micrographs, (figure A.4 in Appendix A show a size distribution for sample A). The average size is 7 nm for the sample shown in figure 2.1a and 9 nm for the sample shown in figure 2.1c. The increase in contrast in the dark field image (figures 2.1b and 2.1d) and the increase in sharpness of the selected area diffraction patterns (insets) indicates that a change in the particle structure has occurred as the annealing temperature has been increased.

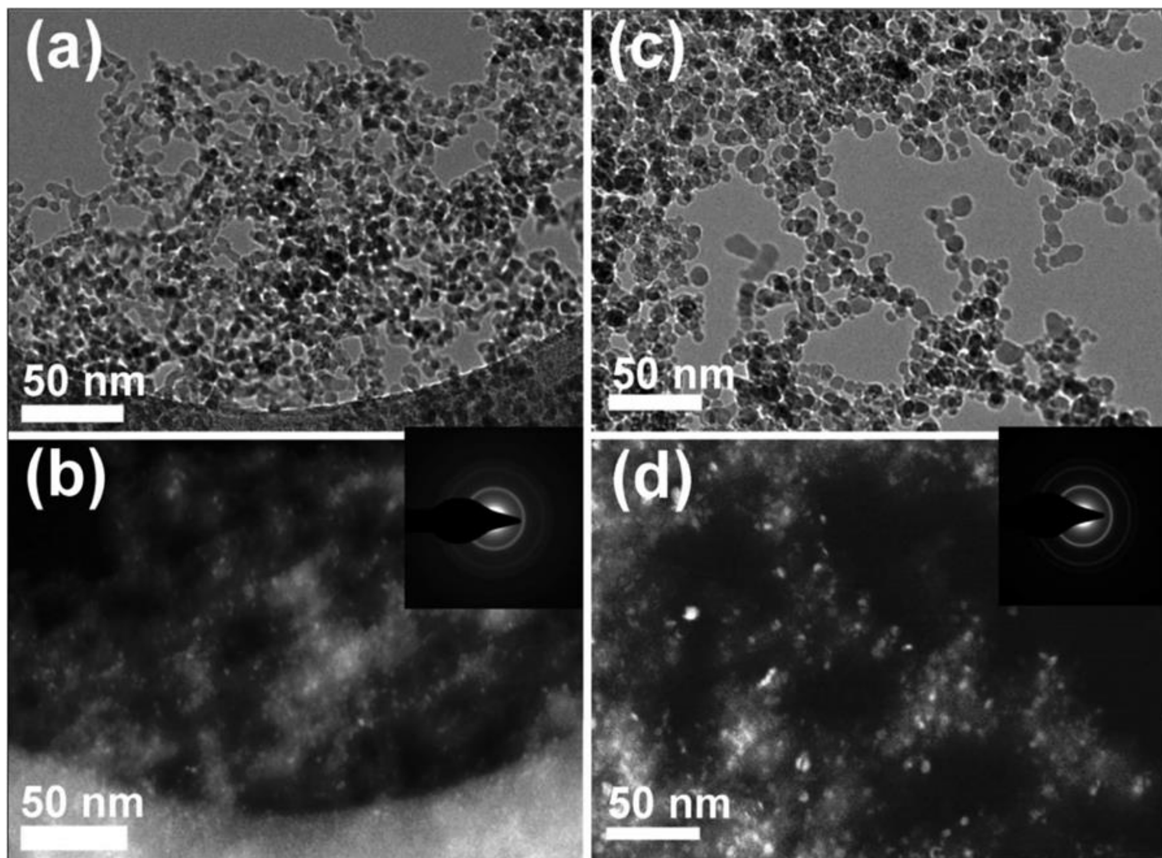

Figure 2.1: (a) Bright field image of particle annealed in flight at a temperature of 720 C. Particles were collected onto a lacey carbon grid placed in the system exhaust line. (b) Dark field of (a), indicating a partial degree of crystallinity, as confirmed by the diffraction pattern in the inset showing the signal from the [111], [220] and [311] planes. (c) Bright field for particles annealed at 790 C. (d) Dark field of (c), indicating higher degree of crystallinity. This conclusion is supported by the diffraction pattern in the inset, which show sharper features compared to that of the particles annealed at 720 C.

Table 2.1: Summary of process parameters for the samples discussed in this contribution. Samples A, B, and C correspond to three different initial particle sizes produced by varying the residence time in the plasma reactor. The particle size listed at the exit of the tube furnace shows an increase due to particle agglomeration and coalescence

Sample	Particle size at exit of plasma (nm)	Particle size at exit of tube furnace (nm)	Argon flow rate (sccm)	SiH_4 flow rate (1.37% in Argon) (sccm)	Tube diameter for the first stage (mm)	Orifice diameter (mm)	Pressure in the first stage (Torr)	Residence time in the first stage (ms)
A	4	9	70	30	9.525	1.5	3.7	4
B	7	13	70	30	9.525	1.0	7.5	8
C	11	18	70	30	25.4	1.0	7.1	55

Pressure range in the second stage (Torr)	Temperature range (°C) during annealing	Residence time in the second stage (ms) (annealing time)
1–2	680–830	It varies depending on temperature and pressure: 120 ms at 1 Torr, 810 °C 270 ms at 2 Torr, 680 °C.

Regarding the growth in particle size during annealing (the particle size for sample A is around 4 nm at the plasma exit), we should point out that the rate with which the powder is collected at the exhaust of the whole system, measured in mg per hour, does not depend on annealing condition. The production rate has been calculated by measuring the mass change of the filter placed on the system exhaust line over a given period of time. Moreover, this type of plasma reactor fully consumes the silane precursor, as reported in ref. 13. This suggests that the precursor is depleted by the time the particles enter the annealing stage of the reactor. This rules out the possibility that size growth occurs *via* deposition of unreacted precursor onto the particle surface (growth via chemical vapor deposition), and it also rules out that nucleation of new particles occurs during the annealing step. The particle size increases because of agglomeration and coalescence of the particles during the in-flight annealing step. We will discuss more extensively the influence of coalescence on crystallization later in this paper.

While TEM provides qualitative evidence that structural changes occur to the plasma-produced particles as they travel through the annealing stage, we aim at obtaining a quantitative measurement of the activation energy (E_a) for nanoparticle crystallization. For this purpose, a measurement of the crystalline fraction (x_c) is necessary. We use a combination of Raman and XRD characterization to achieve this. Figure 2.2 shows the Raman and XRD spectra for the 7 nm silicon particles as a function of annealing temperature.

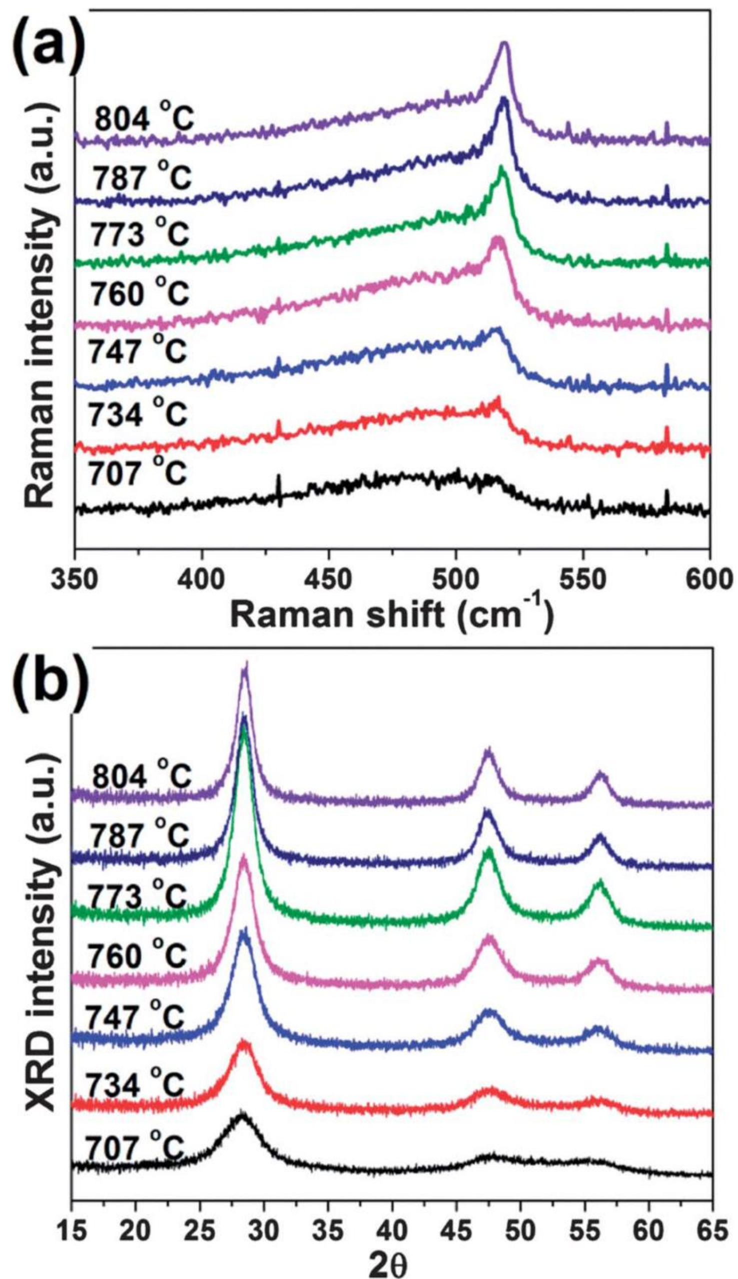

Figure 2.2 Change in the Raman (a) and XRD (b) spectra for silicon nanoparticles produced under the conditions of 'sample A' (see Table 2.1), as a function of in-flight annealing temperature.

For the Raman measurement, the laser (48mW at 532 nm) is attenuated with a 0.1% transmittance filter to avoid sample heating and subsequent broadening of the spectra. The laser spot size is 2 µm. The sample is prepared by pressing the powder onto a copper-coated silicon wafer. The copper coating eliminates any contribution from the underlying silicon substrate. For XRD, a PANalytical EMPYREAN system with a CuK_{α} source is used. The powder is pressed onto a zero-background substrate. Figure 2.2 confirms that a gradual change in the particle structure occurs as the annealing temperature in the second stage of the reactor is increased. In figure 2.2 we also report the annealing temperatures as measured using a thermocouple placed in contact with the quartz tube at the center of the tube furnace length. Obtaining a quantitative measurement of crystalline fraction in the sample using the data shown in figure 2.2, especially with respect of the Raman data, is not trivial. As pointed out by the authors in ref. 20 and 21, the cross section for interaction of the amorphous and crystalline structure with the Raman excitation source is different. Raman characterization applied to silicon overestimate the volume fraction of amorphous material. Moreover, the Raman response of the nanocrystalline material is modulated by the presence of stress. We point out that for the determination of the activation energy for crystallization, the presence of a constant scaling factor (A) in the crystalline fraction measurement $(A * x_c)$ does not affect the value of E_a as determined via the Arrhenius plot $\left(ln(A * x_c)\right) = \left(ln(A) + ln(x_c)\right)$The constant scaling factor introduces an offset in the semi logarithmic plot without affecting the slope of the plot, which corresponds to the activation energy. It is

important to verify that any scaling factor 'A' in the crystalline fraction measurement performed using Raman is actually constant in the temperature interval of interest. To verify this we compare the activation energy obtained by Raman with that obtained by XRD.

Quantifying the crystalline fraction from Raman measurements presents the additional challenge of fitting the experimental data with a model that appropriately describes the behavior of such small crystalline volumes. We have fitted the raw Raman data using a variety of models that include phonon confinement effects to predict the Raman line shape for nanocrystals, and we have compared the crystalline fraction obtained using Raman to that obtained using XRD. In figure 2.3 we show the same Raman spectrum for powder annealed at a tube furnace temperature of 760 ^{0}C, fitted using a variety of methods to predict the shape and intensity of the contribution from crystalline silicon (peak position between 512 cm^{-1} and 521 cm^{-1}). The different models are clearly labelled in the figure. We use a Gaussian peak profile for the contribution from amorphous silicon, with a peak position centered between 475 cm^{-1} and 485 cm^{-1}. The RWL model was first introduced by Richter, Wang and Ley[22] to account for the relaxation of the selection rules for phonon excitation in small volumes. Paillard et al.[23] proposed an improved version of the RWL model based on a modified phonon dispersion relation. More recently, Faraci et al.[24,25] proposed yet another model with the goal of obtaining a better fit between the experimentally observed shift in the Raman peak position as a function of particle size. The mathematical expressions and explanations for these models

are located in Appendix A, see Equations A.1, A.2, and A.3. In figure 2.3 we also use a simple Gaussian peak profile for the crystalline contribution (see graph labelled as '2 Gaussian peaks'), and we also use a third Gaussian peak centered between 500 cm^{-1} and 510 cm^{-1} to account for the scattering intensity at intermediate wavenumbers between the amorphous and the crystalline peak (see graph labelled as '3 Gaussian peaks'). Although this last methodology lacks clear theoretical motivation, it is often used in the literature to obtain a good numerical fit with the experimental data,[26–28] and the third peak centered between 500 cm^{-1} to 510 cm^{-1} is often attributed to strained bonds at the surface of nanocrystals.

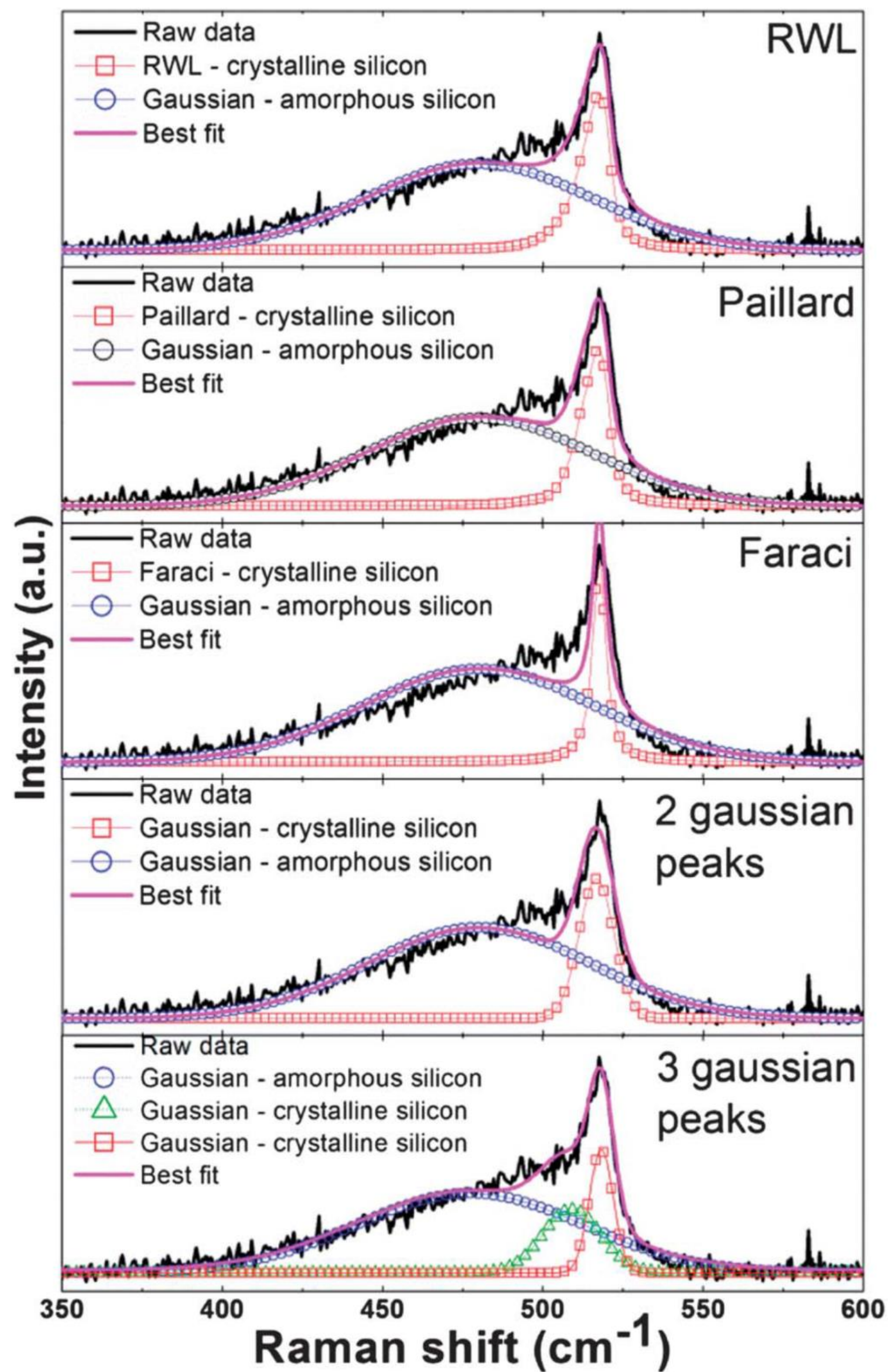

Figure 2.3 Fitting of the Raman data for sample A (see Table 2.1), annealed in flight at 760^0 C, using a variety of fitting models.

The crystalline fraction x_c is calculated as $A_{520}/(A_{520} + A_{480})$ for all the fitting procedures except for the '3 Gaussian peaks' procedure, for which it is calculated as $(A_{520} + A_{500})/(A_{520} + A_{500} + A_{480})$. A_{520}, A_{500} and A_{480} are the areas under the curves centered at ~520 cm^{-1}, ~500 cm^{-1} and ~480 cm^{-1} respectively. We would like to stress that the theoretical derivation of the Raman peak shape and position as a function of the physical properties of the nanocrystals (size, shape, interface with other materials etc.) is an area of on-going research and goes beyond the scope of this work. Our approach is to use a variety of fitting models and monitor the influence of the fitting procedure on the calculated value of activation energy. The crystalline fraction has been measured from XRD data using the procedure described in ref. 29 (see figure A.5 in Appendix A for details on the XRD data fitting). In figure 2.4a we compare the crystalline fraction x_c using the different fitting procedure and the XRD data, as a function of annealing temperature.

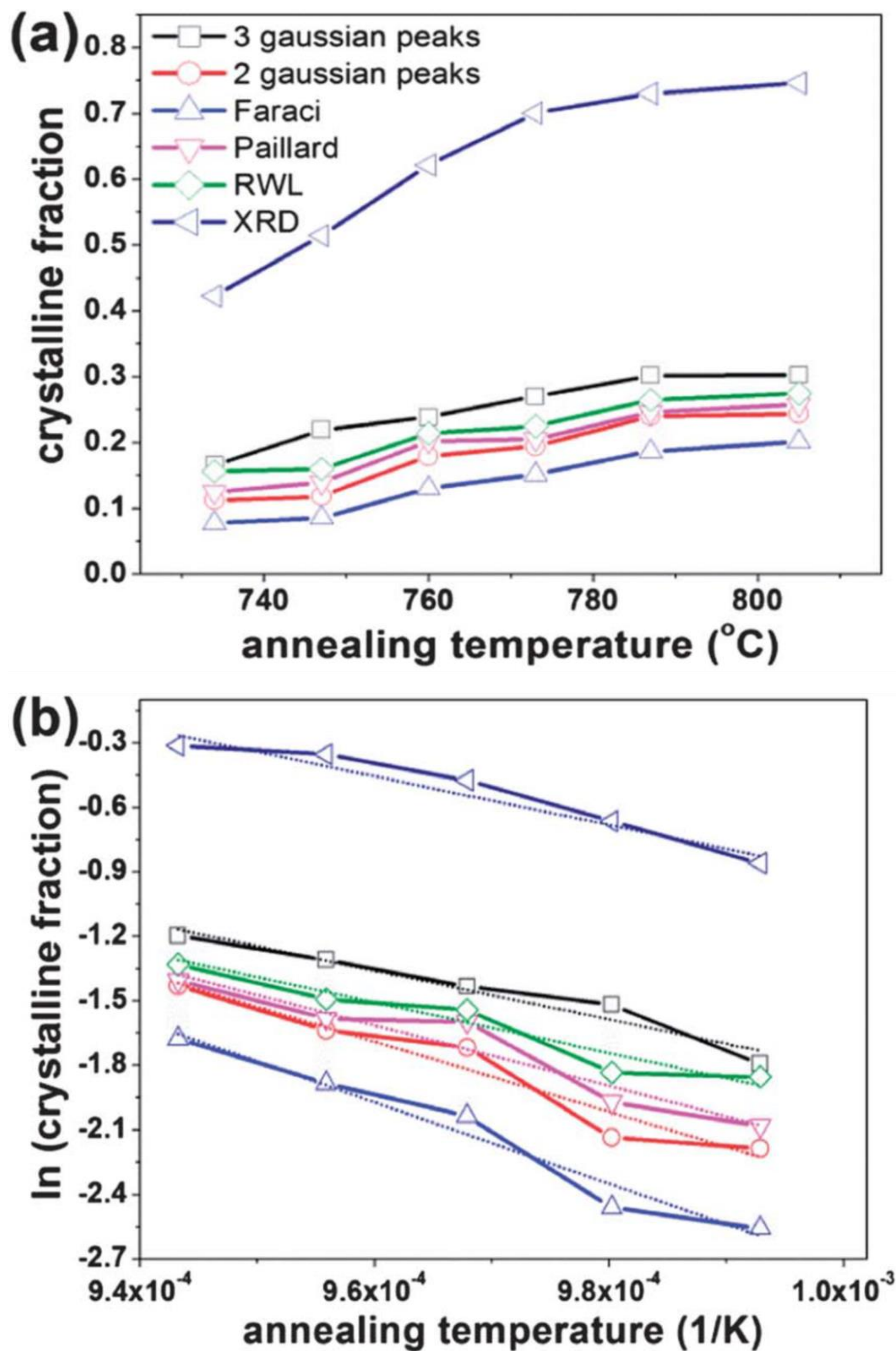

Figure 2.4 (a) Crystalline fraction measured using XRD and Raman measurements as a function of in-flight annealing temperature. The results from a variety of Raman fitting procedures are reported. (b) Plot of the logarithm of the crystalline fraction versus the inverse temperature in Kelvin (Arrhenius plot) for the data shown in (a).

As expected, there is a significant spread in the values of crystalline fraction, with the values obtained from Raman being significantly lower than those obtained from XRD. In figure 2.4b we generate the Arrhenius plot using the data points from figure 2.4a. There is an offset between the different lines but the spread in the slope of the linear fit (which corresponds to the activation energy for phase transformation) is relatively small.

In Table 2.2 we summarize the results obtained from the analysis of the Raman and the XRD data. We also report the residual and R-squared (R^2) for the different Raman fitting procedures. We find that the '3 Gaussian peaks' fitting procedure reproduces the Raman measurement closely, although both RWL and Paillard peak profiles also generate reasonably good fits. Fitting of the crystalline fraction x_c calculated using these three methods results in an activation energy of 0.97, 0.968 and 1.21 eV respectively. The '2 Gaussian peaks' and the Faraci method give a slightly lower R^2, a higher residual between the raw data and the fitting profile, and higher values of activation energy (1.4 and 1.63 eV). The activation energy obtained from the crystalline fraction measured via XRD is equal to 0.977 eV, in good agreement with the Raman measurements processed using the '3 Guassian peaks', the RWL and the Paillard methods.

Table 2.2 Activation energies for crystallization obtained using the data shown in Fig. 2.4. The residual and R-squared (R^2) for the fitting of the Raman data with various procedures are also reported

Raw data – fitting procedure	E_a (eV)	Residual ($\times 10^3$)	R^2
Raman – 3 Gaussian peaks	0.97	14.3	0.9648
Raman – 2 Guassian peaks	1.4	24.53	0.9396
Raman – Faraci	1.63	37.5	0.9076
Raman – Paillard	1.21	22	0.9457
Raman – RWL	0.968	16.67	0.9504
XRD	0.977	—	

The fact that there is good agreement between activation energies measured from the Raman data and the XRD data is likely a consequence of the fact that there is no additional effect on the Raman spectra induced by stress. XRD measurements on our powders and their processing via the Willamson–Hall method (see figure A.6 in Appendix A) suggest that the stress in the nanocrystals is negligible. This is an important difference compared to the case of nanocrystalline silicon thin films in which stress can induced in the film depending on the growth parameters.[21]

The activation energy for crystallization is strongly dependent on particle size. In Fig. 2.5 we plot the crystalline fraction obtained from Raman data fitted using the RWL method mentioned above for samples produced under conditions A, B and C from Table 2.1. The particle sizes at the exit of the plasma are 4, 7 and 11 nm respectively for these three experimental conditions. As already discussed, agglomeration and coalescence lead to an increase in particle size during the annealing process. For sample A, the average

particle size grows to 7 nm at 740 ^{0}C and to 9 nm by the time the temperature has reached 830 ^{0}C. For sample B, the particle size ranges from 11 nm at 790 ^{0}C to 13 nm at 820 ^{0}C. Finally for sample C the size ranges from 15 nm at 820 ^{0}C to 18 nm at 850 ^{0}C.

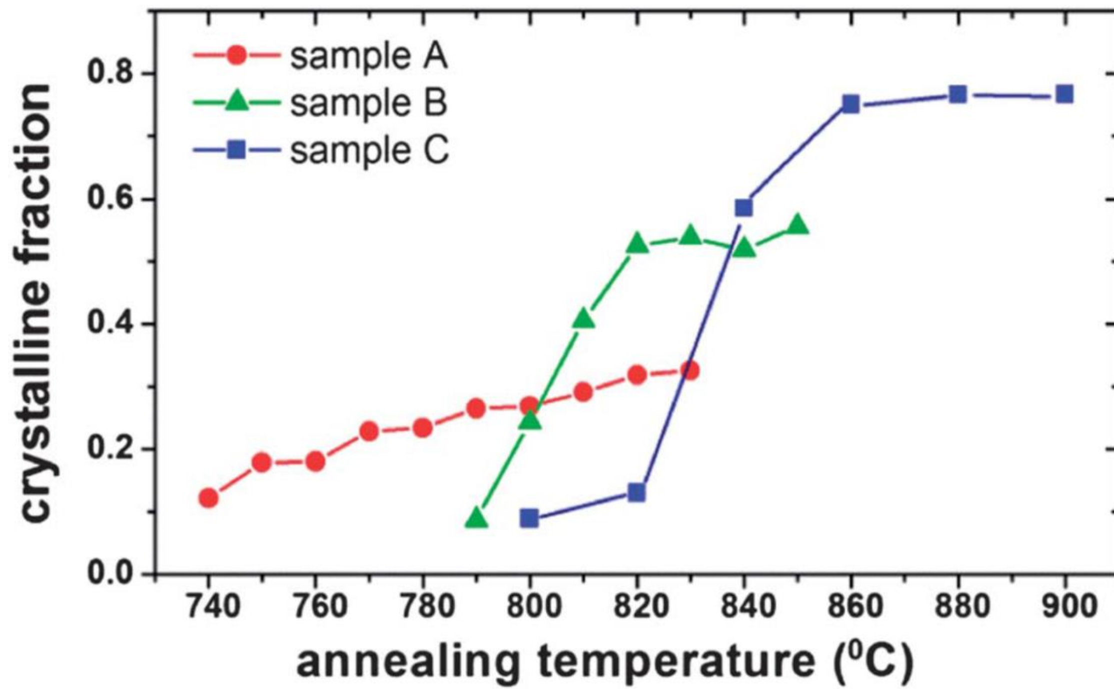

Figure 2.5 Variation of the crystalline fraction, as measured using Raman data and the RWL model to predict the scattering from the crystalline phase, as a function of in-flight annealing temperature for three different particles sizes, produced under the conditions summarized in Table 2.1.

The dependence of the crystalline fraction over annealing temperature is clearly different for the three sizes. Smaller particles crystallize at lower temperature and over a broader temperature interval. The crystalline fraction x_c reaches ~0.33 at 830 ^{0}C for the 7–9 nm size range. High resolution TEM micrographs, in combination with selected area diffraction patterns confirm that at this temperature a very high fraction of the particles has crystalline structure (see Appendix A, figure A.7). This is consistent with the behavior observed in figure 2.4, which suggests that Raman consistently underestimates the crystalline fraction because of the strongest interaction between the Raman excitation source and the amorphous silicon matrix. The Arrhenius plot for the data shown in Fig. 2.5 is reported in Appendix A (see figure A.8). We observe a rapid increase in activation energy with particle size. A more detailed investigation of the dependence of activation energy with particle size, with measurements over a wider size range and with smaller difference between particle sizes, is currently on-going and will be subject of a future contribution.

We have then focused on the particles produced under the conditions for sample A (see Table 2.1), whose average size is between 7 nm and 9 nm during the annealing process. We have performed additional in-flight annealing experiments for three different pressures in the annealing stage. Since the total flow rate is kept constant, varying the pressure is equivalent to adjusting the residence time in the annealing zone (from ~120 ms to ~240 ms, based on the flow velocity, for a constant annealing temperature of 790 ^{0}C). In figure 2.6a we plot the logarithm of the crystalline fraction x_c

defined earlier against the inverse of the annealing temperature. We have used the RWL model to predict the peak profile for the crystalline contribution to the Raman signal. We then calculate the ratio between x_c and the residence time in the annealing zone and plot it against the inverse temperature in figure 2.6b.

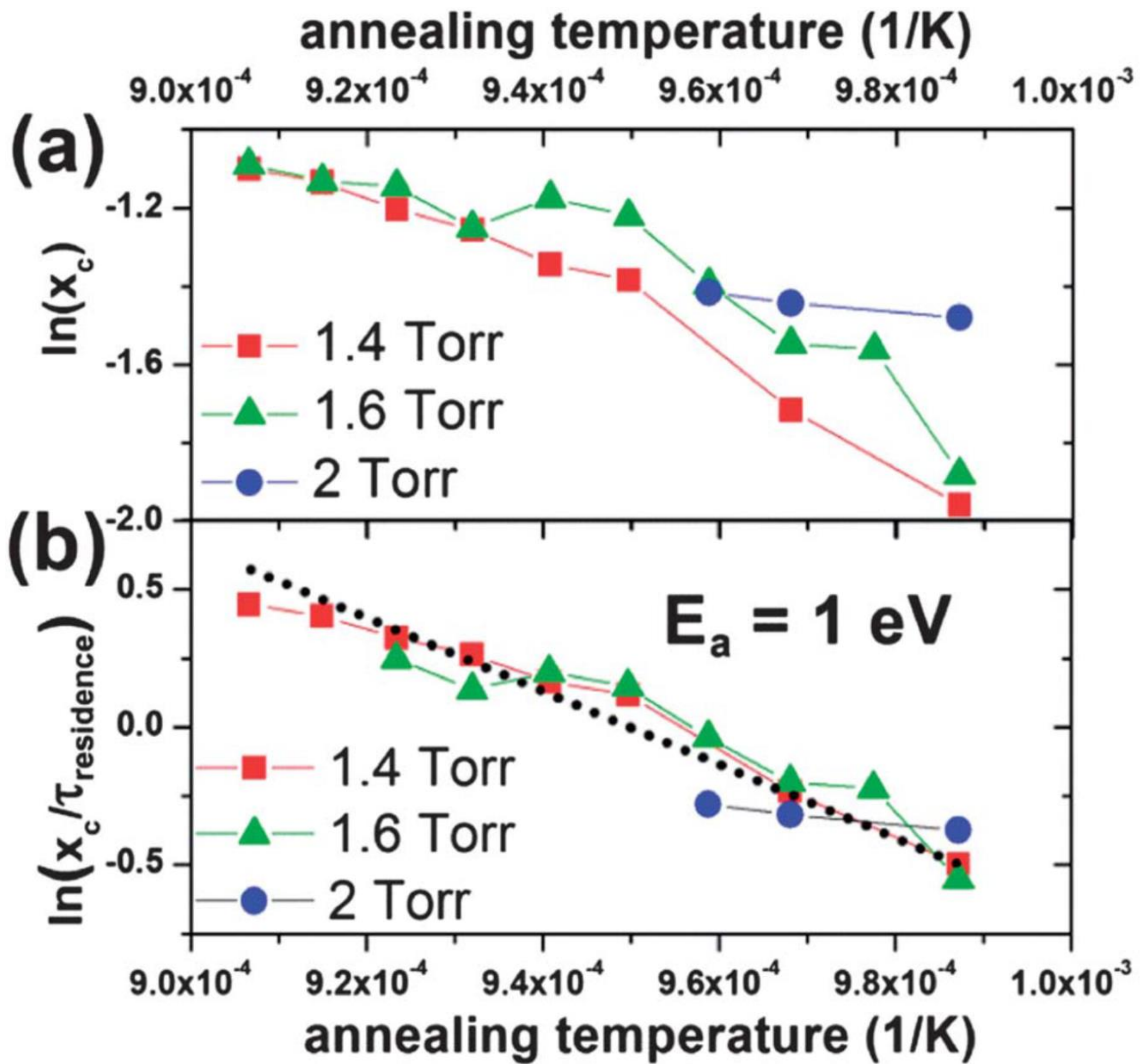

Figure 2.6 (a) Logarithm of the crystalline fraction x_c (calculated from Raman data using the RWL peak profile for the crystalline peak) against inverse temperature for the particles produced under the condition for sample A (see Table 2.1), at three different pressures in the annealing stage. (b) Same as (a) normalized over the residence time in the high-temperature zone.

This is an Arrhenius plot which is well fit by an exponential dependence with activation energy of 11 853 K, corresponding to roughly 1 eV, and a pre-exponential term with a value of 7.77 x 10^4 per second. This is a lower bound for the crystallization rate of small silicon particles for the case of thermal annealing, since it is based on Raman determination of the crystalline fraction, which, as already extensively discussed, underestimates the crystalline fraction value. Since TEM data (see figure A.5 in Appendix A) further supported by the XRD data shown in figure 2.4 for similar size range, suggests that for the higher annealing temperature the sample is composed of nanocrystals, we can rescale the pre-exponential factor so that the crystalline fraction at 830 ^{0}C goes from 0.33 to 1. The following expression reasonably predicts the crystallization rate for free-standing silicon nanoparticles under the conditions of thermal annealing:

Equation 2.1:

$$\frac{\mathrm{d}x_{\mathrm{c}}}{\mathrm{d}t}\left[\sec^{-1}\right] = 2.33 \times 10^{5}\left[\sec^{-1}\right]\ \exp\left(-\frac{11853}{T[K]}\right)$$

2.5 Discussion

The main conclusion of this study is that a significant reduction in the activation energy for structural change (amorphous to crystalline) is observed for small silicon particles. Let's consider the case of crystallization of amorphous silicon thin films. A comprehensive overview on the crystallization of amorphous silicon is discussed in ref. 30: the kinetics of crystallization are rate-limited by the nucleation of small crystalline nuclei within the amorphous matrix. According to the authors, the minimum value of activation energy associated with the formation of the nuclei is ~2 eV. The ~1 eV activation energy that we reproducibly measure for our smallest particles is significantly lower than this value.

We should point out that the reduction of the melting point in nanostructures[31,32] is not expected to play a role in our system. For the case of 7 nm silicon particles, theory predicts a melting point of 1100 ^{0}C for silicon, well above the annealing temperatures utilized in this study for any of the considered size ranges. This implies that the phase transformation in our system does not occur *via* melting and re-solidification of the particles.

Other groups have investigated the crystallization of small silicon particles. Hirasawa et al.[33] used an apparatus similar to the one described in this paper, except for the use of laser ablation of a solid silicon target to produce silicon particles. They observed a reduction in the temperature necessary to observe full crystallization of the particles

during in-flight annealing, consistent with our results. Several reports have investigated the structural changes in nanostructures using in-situ TEM characterization,[31,32] although these annealing experiments fail to capture the crystallization kinetics over short time scales (tens to hundreds of milliseconds). Our results instead capture the kinetics at time scales which are comparable to the residence time of continuous flow non-thermal plasma reactors.

Still, there are several effects that are known to affect the rate of structural changes in silicon. Ion bombardment is well known to increase the crystallization rate for the case of amorphous silicon films grown using plasma enhanced chemical vapor deposition (PECVD),[30] but in our case the particles undergo a purely thermal annealing process. The presence of hydrogen in the amorphous matrix affects its structural stability, and this effect will be discussed more extensively in the next section. The effects of agglomeration and coalescence of free-standing silicon particles on their crystallization rate will also be discussed.

2.5.1 Role of hydrogen

The interaction between hydrogen and amorphous silicon thin films grown by PECVD has been extensively investigated.[34–41] Addition of hydrogen to the gas mixture is known to lead to a transition from growth of hydrogenated amorphous silicon to growth of microcrystalline silicon.[37] Exposure of the amorphous silicon film to plasma-generated atomic hydrogen leads to inclusion of hydrogen into the amorphous silicon matrix, which relaxes the structure and leads to an increased crystallization rate during thermal annealing.[42] In addition, exposure to atomic hydrogen has been shown to increase the crystallization rate during growth of the film itself,[41] leading to the growth of microcrystalline thin films.

Our case is very different from that of PECVD-grown hydrogenated amorphous silicon films. First of all the annealing process is a purely thermal process, and the particles are not exposed to an atomic hydrogen flux during while the structural change is taking place. Second, we have performed *in-situ* FTIR absorption measurements on silicon particles which have not been annealed (see figure A.9 in Appendix A), and have found sharp features corresponding to various Si–H vibrational modes. The small width of these peaks and the absence of a wide feature in the 2000–2050 cm^{-1} range, which is usually a signature of the presence of hydrogen in the bulk of the amorphous silicon matrix,[36,43] strongly indicate that hydrogen is present solely at the surface of these particles. The same conclusion has been reached by Jariwala et al.,[44] who performed a detailed FTIR

study on silicon nanoparticles produced using the continuous-flow non-thermal plasma reactor design introduced in ref. 13. We have also investigated the thermal stability of the hydrogen passivation by monitoring the value of the area under the various peaks related to silicon-hydrogen moieties as a function of the in-flight annealing temperature (see figure A.9 (top) in Appendix A). Thermally induced desorption effectively removes the hydrogen from the particle surface for a temperature as low as 650 ^{0}C, which is below any of the annealing temperatures considered here. Hydrogen may still be present in the initial part of the annealing tube. Still, the fact that the particles are not exposed to atomic hydrogen during annealing and the fact that hydrogen is present solely at the particle surface suggest that it does not play a significant role in the crystallization process observed in our system.

2.5.2 Particle agglomeration and coalescence

It is difficult to completely eliminate particle agglomeration and coalescence during in-flight annealing. The coalescence process has been extensively investigated by the group of Zachariah, who found that coalescence leads to a net energy release and to an increase in the particle temperature because of the reduction in specific surface area as two particles fuse into one.[45–47] The same group also found that the rate with which this energy is released depends on the particle surface termination, with a hydrogen termination leading to a significant reduction in the coalescence rate and to a reduction in the temperature increase during the process. The role of surface hydrides on the structure of silicon nanoparticles has been investigated by Holm and Roberts in ref. 48: the authors use a non-thermal plasma source identical to the one described in ref. 13 to produce small nanocrystals, and perform in-flight annealing studies with a tube furnace. They find that spherical, single crystal particles are formed as a consequence of agglomeration and coalescence only after hydrogen has been fully desorbed from the surface ($T > 750\ ^{0}C$), while polycrystalline agglomerates are observed at lower temperatures. The authors in ref. 49 also observed a surface termination-dependent kinetic of coalescence, with large spherical particles produced under conditions that lead to an hydroxyl surface termination. These reports support the conclusion that the particle surface termination can affect its rate of coalescence, which in turn affects that rate with which energy is release during the process.

The important question for this study is whether the energy released during the coalescence process taking place during the in-flight annealing affects the particle crystallization rate. We have addressed this issue by performing measurements with varying silane dilution ratios. This was done by varying the amount of high purity argon that was supplied to the nonthermal plasma together with the argon–silane mixture, while keeping the total flow rate constant. Instead of using a mixture of 70 sccm or argon with 30 sccm of 1.37% silane in argon, we have supplied 100 sccm of 1.37% silane in argon to the reactor. It was shown in ref. 13 that the nanoparticle size depends weakly on the silane concentration. By varying the silane dilution, we do not affect the particle size at the entrance of the annealing stage, but we vary their density. The particle agglomeration rate strongly depends on the particle density ($\sim N^2$, where N is the particle volumetric density).[50,51] Our measurements indicate that the crystallization rate does not change when we vary the particle density, suggesting that the energy released during the coalescence process does not affect the crystallization kinetic, at least for the process parameters considered here.

2.5.3 Crystallization of amorphous silicon nanoparticles

Based on the discussion above, we conclude that many of the processes that can increase the crystallization rate in amorphous silicon thin films (ion bombardment, presence of hydrogen in the matrix, exposure to atomic hydrogen) do not play a role in the thermal annealing process investigated here. While at this time we cannot offer a detailed explanation for the reduction of activation energy for crystallization at small particle sizes, we point out that an increase in the probability of crystallization for the case of nanostructured silicon has been theoretically predicted by the group of Giulia Galli:[52] the authors used molecular dynamics simulation to show that systems with high surface area can accommodate the volume expansion induced by the phase transformation (crystallization) for the case of silicon, resulting in a decrease in the Gibbs free energy of formation of a crystalline nucleus in the vicinity of the system surface.

2.5.4 Production of nanocrystals in non-thermal plasmas

The motivation of this study is to elucidate the mechanism leading to the formation of high quality crystalline nanoparticles in continuous flow non-thermal plasma reactors such as the one described in ref. 13. In ref. 19 it was proposed that interaction with various plasma-produced species (ions and radicals) leads to a significant increase in the nanoparticle temperature, and it was proposed that these exothermic processes lead to the formation of crystalline particles. Still, the average particle temperature in the plasma was predicted to be around 100 ^{0}C higher than the background gas temperature, which does not deviate much from room temperature. Given the short residence time in the plasma (tens of microseconds), and given the results reported here (full crystallization is observed at T ~ 800 ^{0}C for annealing time >100 ms), we conclude that the thermal annealing of the nanoparticles resulting from their interaction with plasma-produced active species cannot justify the formation of particles with a crystalline structure. A more detailed study which incorporates the crystallization rate obtained here (see equation (1)) into the numerical model described in ref. 19 goes beyond the scope of this contribution.

2.6 Conclusions

We have experimentally determined the rate of crystallization of ultrafine amorphous silicon powder. We observe a significant reduction in the activation energy for crystallization as the particle size decreases, which we tentatively attribute to the surface-induced effect predicted theoretically in ref. 52. The results of this study shed light into the mechanisms that lead to the formation of high quality single crystals in continuous flow non-thermal plasma reactors.

2.7 Acknowledgements

This work is supported by the U.S. Department of Energy, Office of Basic Energy Sciences, Division of Materials Sciences and Engineering under Award DE-SC0008934.

2.8 References

1. L. Mangolini, *J. Vac. Sci. Technol., B: Microelectron. Nanometer Struct.–Process., Meas., Phenom.*, 2013, **31**, 020801

2. S. Oda, *Mater. Sci. Eng., B*, 2003, **101**, 19–23

3. K.-S. Cho, N.-M. Park, T.-Y. Kim, K.-H. Kim, G.-Y. Sung and J. H. Shin, *Appl. Phys. Lett.*, 2005, **86**, 071909

4. K.-Y. Cheng, R. Anthony, U. R. Kortshagen and R. J. Holmes, *Nano Lett.*, 2011, **11**, 1952–1956

5. C.-Y. Liu, Z. C. Holman and U. R. Kortshagen, *Nano Lett.*, 2009, **9**, 449–452

6. F. Erogbogbo, C. W. Chang, J. L. May, L. W. Liu, R. Kumar, W. C. Law, H. Ding, K. T. Yong, I. Roy, M. Sheshadri, M. T. Swihart and P. N. Prasad, *Nanoscale*, 2012, **4**, 5483–5489

7. F. Erogbogbo, K. T. Yong, I. Roy, R. Hu, W. C. Law, W. W. Zhao, H. Ding, F. Wu, R. Kumar, M. T. Swihart and P. N. Prasad, *ACS Nano*, 2011, **5**, 413–423

8. T. Seto, Y. Kawakami, N. Suzuki, M. Hirasawa and N. Aya, *Nano Lett.*, 2001, **1**, 315–318

9. M. L. Ostraat, J. W. De Blauwe, M. L. Green, L. D. Bell, H. A. Atwater and R. C. Flagan, *J. Electrochem. Soc.*, 2001, **148**, G265–G270

10. X. Li, Y. He, S. S. Talukdar and M. T. Swihart, *Langmuir*, 2003, **19**, 8490–8496

11. X. Li, Y. He and M. T. Swihart, *Langmuir*, 2004, **20**, 4720–4727

12. A. Bapat, M. Gatti, Y.-P. Ding, S. A. Campbell and U. Kortshagen, *J. Phys. D: Appl. Phys.*, 2007, **40**, 2247–2257

13. L. Mangolini, E. Thimsen and U. Kortshagen, *Nano Lett.*, 2005, **5**, 655–659

14. D. Mariotti and R. M. Sankaran, *J. Phys. D: Appl. Phys.*, 2010, **43**, 323001

15. I. Dogan, N. J. Kramer, R. H. J. Westermann, K. Dohnalova, A. H. M. Smets, M. A. Verheijen, T. Gregorkiewicz and M. C. M. van de Sanden, *J. Appl. Phys.*, 2013, **113**, 134306

16. D. Jurbergs, E. Rogojina, L. Mangolini and U. Kortshagen, *Appl. Phys. Lett.*, 2006, **88**, 233116

17. O. Yasar-Inceoglu, T. Lopez, E. Farshihagro and L. Mangolini, *Nanotechnology*, 2012, **23**, 255604

18. R. Anthony and U. Kortshagen, *Phys. Rev. B: Condens. Matter Mater. Phys.*, 2009, **80**, 115407

19. L. Mangolini and U. Kortshagen, *Phys. Rev. E: Stat., Nonlinear, Soft Matter Phys.*, 2009, **79**, 026405

20. Z. Iqbal and S. Veprek, *J. Phys. C: Solid State Phys.*, 1982, **15**, 377–392

21. C. Ossadnik, S. Veprek and I. Gregora, *Thin Solid Films*, 1999, **337**, 148–151

22. H. Richter, Z. P. Wang and L. Ley, *Solid State Commun.*, 1981, **39**, 625–629

23. V. Paillard, P. Puech, M. A. Laguna, R. Carles, B. Kohn and F. Huisken, *J. Appl. Phys.*, 1999, **86**, 1921–1924

24. G. Faraci, S. Gibilisco, A. R. Pennisi and C. Faraci, *J. Appl. Phys.*, 2011, **109**, 074311

25. G. Faraci, S. Gibilisco, P. Russo, A. R. Pennisi and S. L. Rosa, *Phys. Rev. B: Condens. Matter Mater. Phys.*, 2006, **73**, 033307

26. Q. J. Cheng, S. Y. Xu, S. Y. Huang and K. Ostrikov, *Cryst. Growth Des.*, 2009, **9**, 2863–2867

27. Z. Li, W. Li, Y. Jiang, H. Cai, Y. Gong and J. He, *J. Raman Spectrosc.*, 2011, **42**, 415–421

28. D. Han, J. D. Lorentzen, J. Weinberg-Wolf, L. E. McNeil and Q. Wang, *J. Appl. Phys.*, 2003, **94**, 2930–2936

29. S. Veprek, Z. Iqbal and F. A. Sarott, *Philos. Mag. B*, 1982, **45**, 137–145

30. C. Spinella, S. Lombardo and F. Priolo, *J. Appl. Phys.*, 1998, **84**, 5383–5414

31. A. N. Goldstein, C. M. Echer and A. P. Alivisatos, *Science*, 1992, **256**, 1425–1427

32. A. N. Goldstein, *Appl. Phys. A: Mater. Sci. Process.*, 1996, **62**, 33–37

33. M. Hirasawa, T. Orii and T. Seto, *Appl. Phys. Lett.*, 2006, **88**, 093119

34. W. M. M. Kessels, A. H. M. Smets, D. C. Marra, E. S. Aydil, D. C. Schram and M. C. M. van de Sanden, *Thin Solid Films*, 2001, **383**, 154–160

35. S. Agarwal, S. Sriraman, A. Takano, M. C. M. van de Sanden, E. S. Aydil and D. Maroudas, *Surf. Sci.*, 2002, **515**, L469–L474

36. W. M. M. Kessels, D. C. Marra, M. C. M. van de Sanden and E. S. Aydil, *J. Vac. Sci. Technol., A*, 2002, **20**, 781–789

37. G. Dingemans, M. N. van den Donker, D. Hrunski, A. Gordijin, W. M. M. Kessels and M. C. M. van de Sanden, *Appl. Phys. Lett.*, 2008, **93**, 111914

38. D. C. Marra, E. A. Edelberg, R. L. Naone and E. S. Aydil, *J. Vac. Sci. Technol., A*, 1998, **16**, 3199–3210

39. S. Ramalingam, D. Maroudas and E. S. Aydil, *J. Appl. Phys.*, 1998, **84**, 3895–3911

40. S. Sriraman, S. Ramalingam, E. S. Aydil and D. Maroudas, *Surf. Sci.*, 2000, **459**, L475–L481

41. S. Sriraman, S. Agarwal, E. S. Aydil and D. Maroudas, *Nature*, 2002, **418**, 62–65

42. C. Godet, N. Layadi and P. R. I. Cabarrocas, *Appl. Phys. Lett.*, 1995, **66**, 3146–3148

43. S. Agarwal, A. Takano, M. C. M. van de Sanden, D. Maroudas and E. S. Aydil, *J. Chem. Phys.*, 2002, **117**, 10805–10816

44. B. N. Jariwala, N. J. Kramer, M. C. Petcu, D. C. Bobela, M. C. M. van de Sanden, P. Stradins, C. V. Ciobanu and S. Agarwal, *J. Phys. Chem. C*, 2011, **115**, 20375–20379

45. K. E. J. Lehtinen and M. R. Zachariah, *Phys. Rev. B: Condens. Matter Mater. Phys.*, 2001, **63**, 205402

46. K. E. J. Lehtinen and M. R. Zachariah, *J. Aerosol Sci.*, 2002, **33**, 357–368

47. T. Hawa and M. R. Zachariah, *Phys. Rev. B: Condens. Matter Mater. Phys.*, 2005, **71**, 165434

48. J. Holm and J. T. Roberts, *J. Phys. Chem. C*, 2009, **113**, 15955–15963

49. V. Švrček, D. Mariotti, K. Kalia, C. Dickinson and M. Kondo, *J. Phys. Chem. C*, 2011, **115**, 6235–6242

50. S. K. Friedlander and C. S. Wang, *J. Colloid Interface Sci.*, 1966, **22**, 126–132

51. S. K. Friedlander, *Smoke, dust and haze*, Oxford University Press, 2000

52. T. S. Li, D. Donadio, L. M. Ghiringhelli and G. Galli, *Nat. Mater.*, 2009, **8**, 726–730

Chapter 3

On the Nucleation and Crystallization of Nanoparticles in Continuous-Flow Nonthermal Plasma Reactors

3.1 Abstract

The use of nonthermal plasmas for the processing of nanomaterials remains the focus of ongoing investigations because of the many advantageous properties of this class of processes. Silicon nanoparticles in particular are easily produced using continuous flow nonthermal plasma reactors. This has become a technologically relevant technique especially because silicon is an earth abundant material with important applications in many energy-related fields. Still, there are significant gaps of knowledge in the dynamics of nucleation, growth, and structural evolution of nanoparticles in continuous flow nonthermal plasma reactors. In this contribution, the authors address these issues by performing *in-situ* infrared absorption measurements to monitor the rate with which the silicon precursor, silane, is consumed by the plasma. At the same time, the authors extract nanoparticles from the plasma volume at different stages of their growth and monitor their structural evolution. The authors find that particle nucleation occurs rapidly and that as soon as the silane is fully consumed the particles have grown to almost their final size. At the end of this phase, the particles have an amorphous structure. The crystallization then occurs in the plasma on a time scale of 120 ms for the conditions used for this study. By using an experimentally determined crystallization rate for free-standing silicon

nanopowders, the authors estimate the particle temperature in the plasma. The authors find that the plasma heats the particle to a temperature of over 1100 K, exceeding estimates based on the reaction between the nanoparticle surface and plasma-generated ions and radicals.

3.2 Introduction

The issue of particle nucleation in low-pressure nonthermal plasmas has been actively investigated for several years.[1–5] While the original focus was on the formation of micron-sized dust particles in silane-containing discharges in parallel plate-type of reactors, lately continuous flow nonthermal plasma reactors have attracted significant attention because of their capacity of producing high-quality nanoparticles with high production rates.[6–9] Plasma-produced silicon particles are relevant because of the abundance of silicon, which makes them important candidates for energy-related applications,[10–12] although continuous flow nonthermal plasmas are also capable of producing high-quality nanoparticles of germanium,[13] copper sulfide,[14] indium phosphide,[15] zinc oxide,[16] and carbon diamond,[17] to name a few. Continuous flow reactors typically consist of a glass or quartz tube with one of multiple sets of ring-electrodes which are biased using an appropriate power source, most commonly radio frequency (RF, 13.56 MHz), although very high frequency (144 MHz) sources have also been used.[8] The simplicity of the design of these reactors and the ease of obtaining high quality nanocrystals are making this approach increasingly popular. Despite this, several details are still poorly understood regarding the nucleation and growth of particles in this type of reactors. For instance, in the early work by Bouchoule and Boufendi,[18] silicon particles are extracted from a parallel plate plasma reactor at different stages of the growth process. This simple experiment provides important information on the particle nucleation and growth. To our knowledge, such experiment has never been reported in the literature for the case of continuous flow

discharges. Also, it is well known that these types of reactors are capable of producing nanopowders with precise control over their structure, varying from amorphous to crystalline depending on the input electrical power.[7] This is remarkable for a system which operates near room temperature and for which the particle residence time in the plasma volume, based on the flow velocity, can be as low as few milliseconds.[6] Heating models, which include a basic set of reactions occurring at the nanoparticle surfaces, such as ion recombination and reactions with plasma-produced radicals, predict that significant heating occurs to the particles while they are immersed in the ionized gas,[19,20] although a correlation between these heating models and the particle structural evolution is missing. In this work, we address these issues by performing an experimental study of an argon–silane plasma generated in a 1 in. continuous flow reactor. We have used an aerodynamic extraction probe to sample the dusty plasma at different stages of particle nucleation and growth, i.e., at different axial positions along the plasma length. The nanoparticles have been carefully characterized using transmission electron microscopy (TEM) and Raman spectroscopy. At the same time, we have used *in-situ* Fourier transform infrared spectroscopy (FTIR) to directly monitor the rate with which silane is consumed by the discharge. Correlating the results from these measurements allows us to reach important conclusions on the kinetics of particle formation and structural evolution in nonthermal plasmas.

3.3 Experimental set-up

The set-up consists of a 1 in. outer-diameter, 0.8 in. inner diameter glass cross with a length of 33 in. along the flow direction, and with a length of 7.5 in. along the direct perpendicular to the flow. Two 1.2 in. (30 mm) wide copper electrodes are placed on the outside of the tube. The distance between the electrodes is 3 in. The upstream electrode (i.e., the first electrode in the gas flow direction) is biased using a RF (13.56 MHz) power supply, while the other electrode is grounded. The cross design allows us to either extract particles from the plasma or to perform in-situ FTIR measurements on the system at different axial positions. This is achieved by changing the position of the electrodes with respect of the sampling point. In figure. 1, we show the schematics of these two configurations. The plasma input power can be adjusted over a wide range of values. For the data presented in this paper, the input power is kept equal to 90 W. Under this condition, the reactor produces silicon nanoparticles with 100% crystalline fraction, as verified by extensive Raman spectroscopy, XRD, and TEM data. The argon flow rate is 70 standard cubic centimeters per minute (SCCM) and the silane flow rate (1.37% diluted in argon) is equal to 30 SCCM. The particles are extracted from the plasma volume using the approach shown in figure. 3.1(a). An extraction probe with an outer diameter of 5/8 in. is inserted into the four-way cross. The probe has a hemispherical tip with a 1mm diameter orifice. The pressure in the plasma region is controlled using a butterfly valve downstream of the plasma, and it is equal to 3 Torr for the experiments discussed here. Suction through the extraction probe is generated using a second vacuum pump. The pressure downstream

of the orifice is equal to 0.2 Torr. By monitoring the change in the butterfly valve position when flow is extracted through the extraction probe, we estimate that roughly 10% of the gas flow is pumped through the probe during the sampling experiments. This design allows achieving a high pressure gradient at the extraction point, necessary to efficiently sample the particle from the plasma, as it will be discussed in greater details later in the manuscript. After extraction, the particles are either collected onto a TEM grid placed 17 in. downstream from the orifice, or they can be collected onto a stainless steel mesh to collect enough material for structural characterization.

For the acquisition of the IR spectra, figure 3.1(b), we use a modular FTIR system from Newport-Oriel equipped with a deuterated triglycine sulfate detector. Potassium bromide (KBr) windows are mounted on the vacuum fittings to allow transmission of the infrared signal. The IR beam diameter is limited by the opening size on the KBr window/vacuum flange assembly and it is equal to 11/16 in. The optical absorption length is equal to the plasma diameter, i.e., 1 in. The data discussed in this manuscript have been acquired with a resolution of 8 cm^{-1}, with a scanning frequency of 40 kHz and averaged over 1000 acquisitions to achieve a satisfactory signal-to-noise ratio.

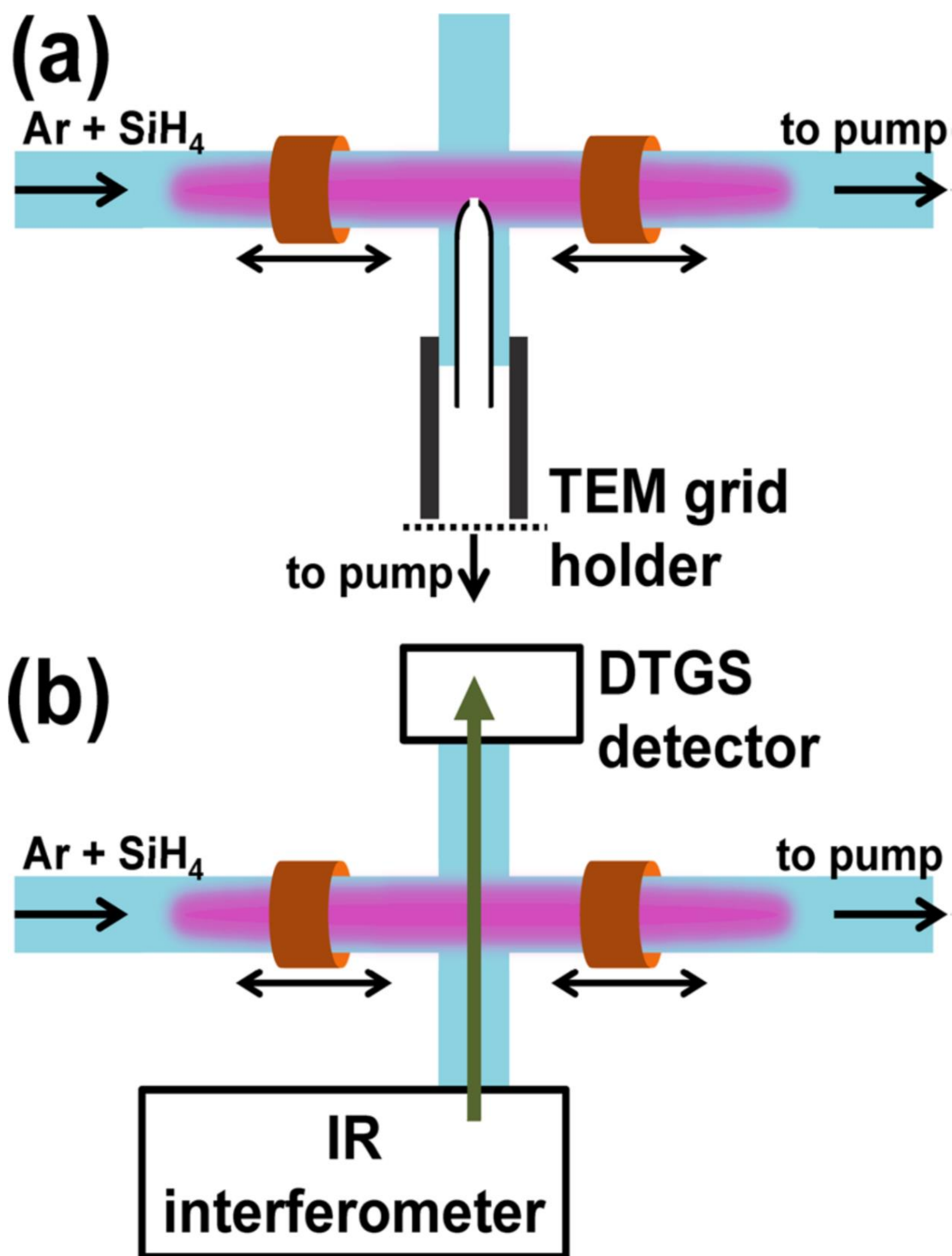

Figure 3.1. (a) Schematic of apparatus used for the sampling of particles at different positions along the plasma reactor. (b) Schematic of apparatus for the in-situ FTIR characterization of the system.

3.4 Results

Figure 3.2 summarizes the results obtained from the aerodynamic extraction probe measurements. Although we have sampled the dusty plasma at several positions along the length of the reactor, for simplicity, we show the data related to three extraction points: upstream of the first ring electrode (-5cm compared to the midline of the first ring electrode), downstream of the first ring electrode (+3.5 cm compared to the midline of the first ring electrode), and downstream of the plasma volume (+37.5 cm compared to the midline of the first ring electrode).

For each of the sampling points, we show bright field TEM micrographs and selected area diffraction patterns obtained using a large area aperture (so that several hundreds of particles are used to form the pattern). In figure 3.2(a), we show these data for the sampling point closest to the first electrode. The particles are in a size range of 5–10 nm, with poorly defined shape and with an amorphous structure, as clearly indicated by the selected area diffraction pattern. In figure. 3.2(b), we show the same data for the second sampling point. Due to the geometry of the sampling design, we could sample the dusty plasma closer to the first electrode (at -3.5 cm), but for this data point, we have inevitably observed significant breakdown of the gas downstream of the extraction probe orifice (i.e., coupling between the RF biased electrode and the metal flange holding the probe used to sample the aerosol). This secondary plasma leads to a modification of the particle structure as it impinges directly onto them as they collected either on a TEM grid or on a filter. Therefore, we are reporting only the data points for which the plasma does not extend

significantly downstream of the orifice (i.e., it extinguishes shortly downstream of the orifice into the extraction channel, without reaching the particles collection point). The nanoparticles shown in figure 3.2(b) have a better defined shape compared to the ones shown in figure 3.2(a), and have a crystalline structure. Finally, in figure 3.2(c), we show the particles sampled 37.5 cm from the first electrode, downstream of the plasma volume. The particles are crystalline with size that is close to the one for the particles in figure 3.2(b).

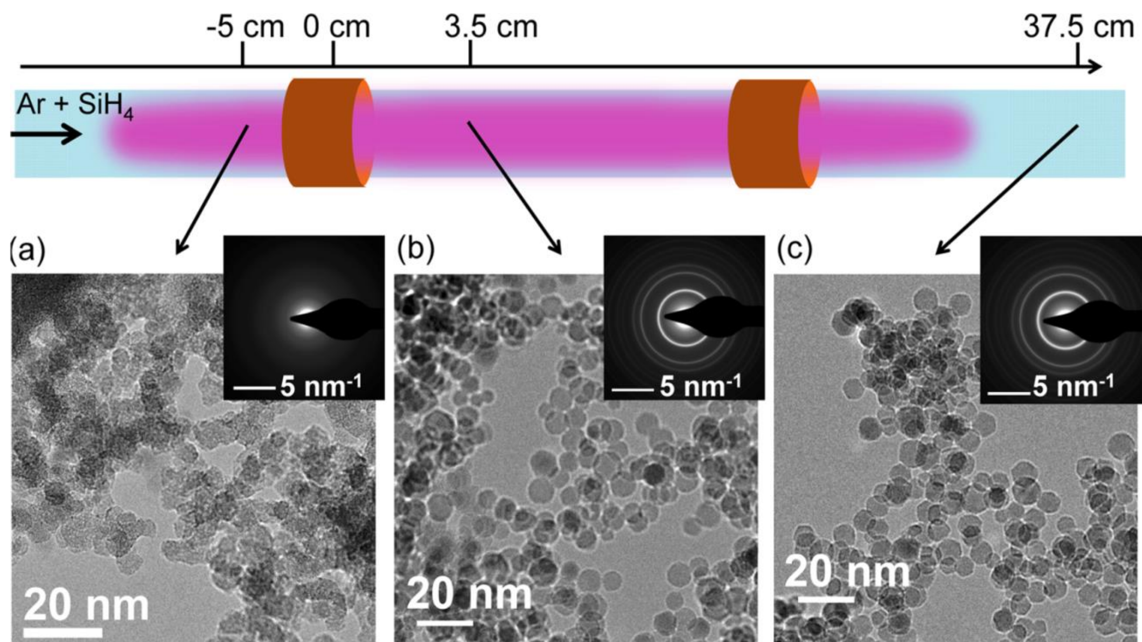

Figure 3.2. TEM micrographs with selected area diffraction patterns for silicon particles extracted at distances equal to (a) -5 cm, (b) 3.5 cm, and (c) 37.5 cm with respect to the centerline of the upstream electrode (0 cm).

The Raman spectra for the three positions discussed in figure 3.2 are shown in figure 3.3. Consistently with the TEM data shown in figure 3.2, particles sampled upstream of the first electrode, figure 3.3(a) have an amorphous structure, since the main feature in the spectra is the 480 cm^{-1} peak associated with amorphous silicon.[21] For the next data point figure 3.3(b), Raman spectroscopy clearly indicate that a fraction of the sample has a crystalline structure, since a peak at 518 cm^{-1} is distinguishable. Finally, the Raman spectra for the powder extracted downstream of the plasma is shown in figure 3.3(c). A well-defined peak at 518 cm^{-1} is observed, typical of crystalline silicon[21] with a shift to lower wavenumbers compared to its bulk counterpart (521 cm^{-1}) because of the small size of the crystals. XRD spectra not shown here for brevity reasons confirm this trend. We should point out that small silicon crystals typically show the asymmetric peak signature shown in figure 3.3.[7,21–23] This makes the interpretation of the Raman spectra and the determination of contributions from amorphous and crystalline phases rather challenging. A variety of theoretical models and approaches have been proposed to accurately predict the Raman signature from silicon nanostructures.[24–27] In figure 3.3, we deconvolute the Raman signal into the sum of a Gaussian profile centered between 480 and 485 cm^{-1}, attributed to the amorphous phase, and a peak centered between 512 and 521 cm^{-1}, corresponding to the crystalline phase, whose shape is generated using the model described by Richter et al.[24] In our experience, this approach gives an optimal fit of the experimental data, although it consistently finds a significant contribution to the overall signal due to amorphous phase, see shoulder in the 450–500 cm^{-1} range in figure 3.3(c). We have collected several high-

magnification TEM images (both bright and dark field micrographs) and selected area diffraction patterns, and we conclude that the sample collected at the exit of the plasma, corresponding to the Raman spectrum shown in figure. 3.3(c), consists of crystalline particles. Upstream of the first electrode, the particles are fully amorphous while the Raman spectrum shown in figure 3.3(b), corresponding to the sample shown in figure 3.2(b), suggests that the particles are transitioning from having an amorphous structure to a crystalline one.

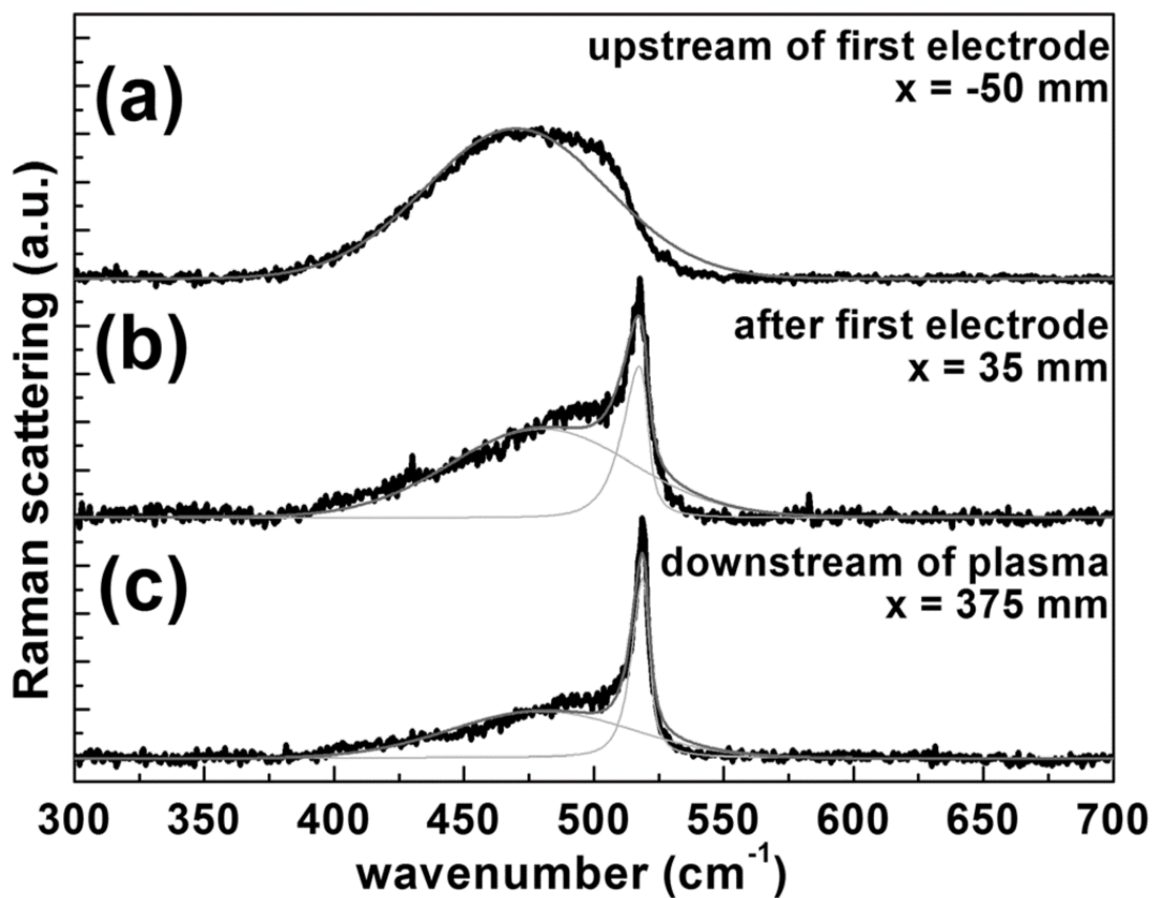

Figure 3.3. Raman spectra for particles extracted from the plasma at (a) x=-50mm, (b) x=35 mm, and (c) x= 375 mm with respect of the upstream electrode. These positions correspond to the samples shown in figure 3.2

Figure 3.4 shows the particle size distribution as measured by analysis of several bright field TEM images such as the ones shown in figure 3.2. The average size of the particles extracted before the upstream electrode is 5.5 nm and the arithmetic standard deviation for this sample is 0.8 nm. These values change to 8 and 1.1 nm, respectively, for particles extracted after the first electrode, and to 8.2 and 1.18 nm, respectively, for the particles collected downstream of the plasma. Therefore, the particles have already grown significantly by the time they reach the first electrode.

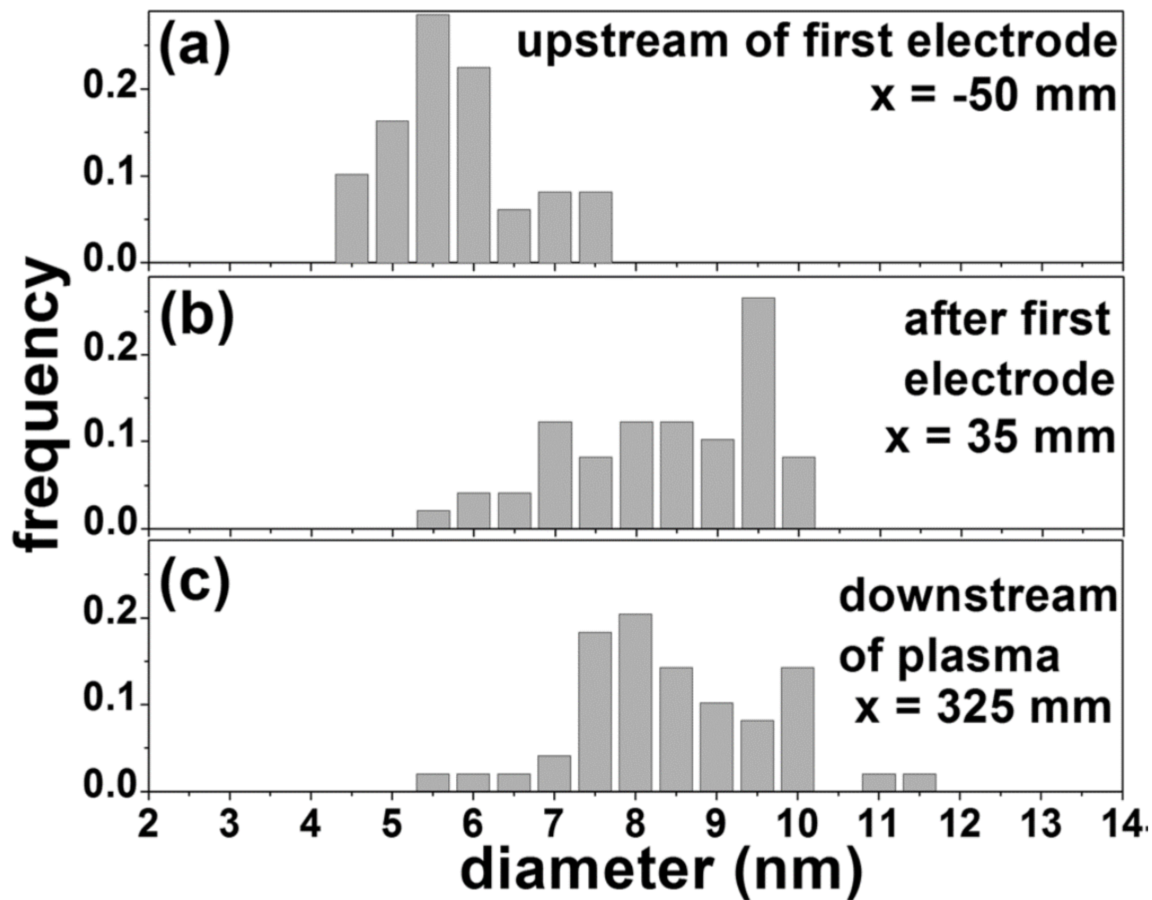

Figure 3.4. Particle size distribution for particles extracted from the plasma at (a) x=- 5 cm, (b) x= 3.5 cm, and (c) x = 37.5 cm with respect to the upstream electrode. The size distributions are based on the analysis of TEM micrographs

In figure 3.5, we show the results of *in-situ* FTIR measurements for the same three positions discussed in figures 3.2 and 3.3. We also show a scan for a position several millimeters upstream of the plasma to show the signal from the unconsumed precursor (SiH_4). The vertical scale is the same for each of these spectra, and the background is measured using pure argon without igniting the plasma in the reactor. It is not necessary to show the full spectrum (from 500 to 4000 cm^{-1} for our system) since the prominent feature is the one coming from the silane precursor, which has a well known absorption peak at 2187 cm^{-1} (Q-branch) with two side bands (P- and R-bands)[28,29] clearly observable in the first spectra of figure 3.5. We stress that the two satellite bands shown in the first spectrum of figure 5 around the 2187 cm^{-1} peak are absorption features induced by the precursor, and not by gas-phase silyls or by surface hydride groups, since the same spectrum is observed for the case of silane without plasma. The feature due to silane is undetectable (below to noise level) for the other three positions. The detection limit in our system is well below 10^{-3}. We could not detect the signature from surface hydride species (SiH_X with $1 \geq X \geq 3$), which we expect to appear in the 2050–2150 cm^{-1} range. A more extensive discussion of this result can be found in section 3.5.

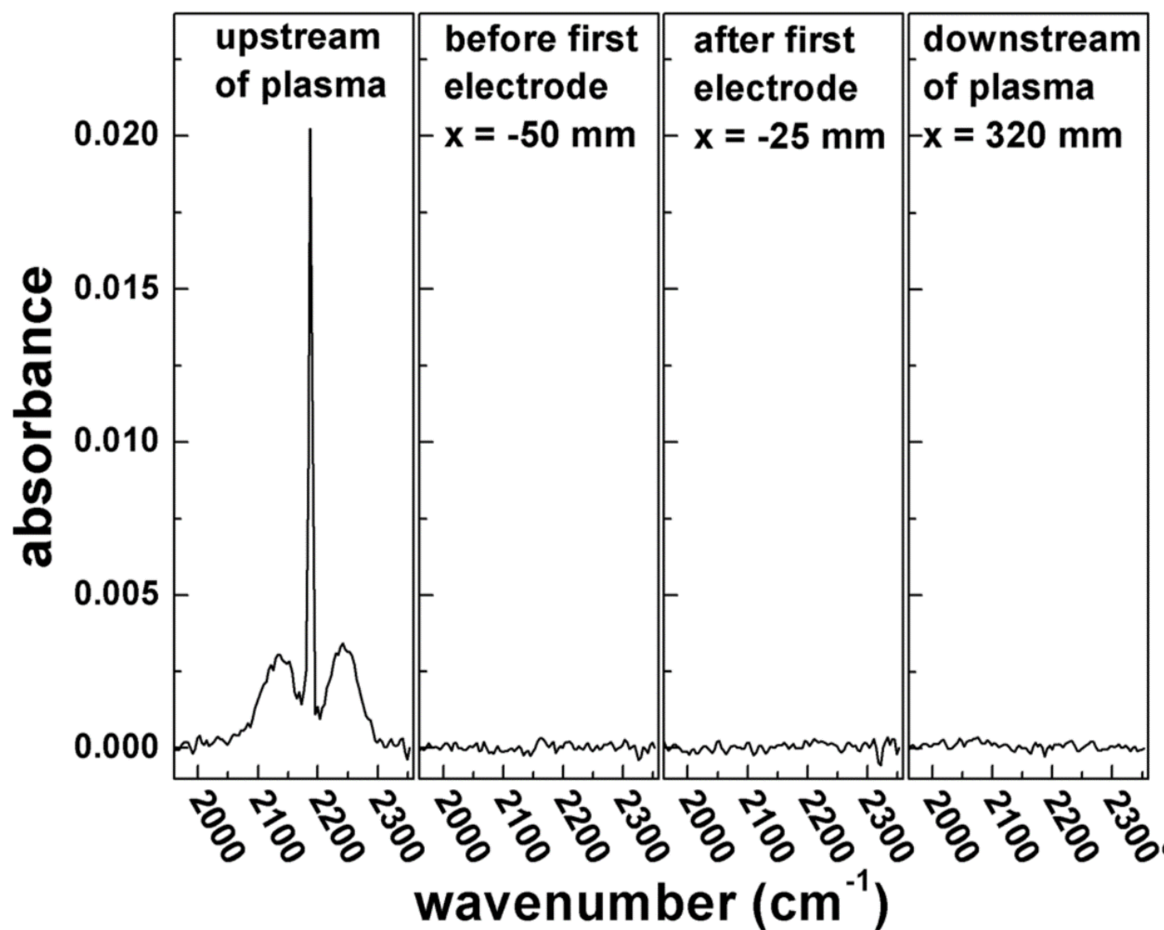

Figure 3.5. FTIR for silane (first spectrum, collected upstream of the plasma volume) and for the positions as (a) x=-50mm, (b) x=35 mm, and (c) x= 375mm with respect of the upstream electrode.

3.5 Discussion

The same data shown in figures 3.2–3.5 have been acquired at several locations along the plasma length. The result of their analysis is summarized in figure 3.6. In figure 6(a), we plot the normalized absorbance from the silicon precursor, silane, along the length of the plasma. The data have been normalized over the silane absorbance without plasma. This plot corresponds to the utilization of silicon precursor by the discharge. Since most of the precursor in this kind of reactor is converted into nanoparticles,[7] this plot gives information on the kinetics of particle nucleation. The normalized silane concentration drops from practically 100% to zero within a distance of ~40 mm. Given a flow velocity of 0.8 m/s for the conditions described in this manuscript, this corresponds to a time interval of ~50 ms. While this consumption rate may appear rapid, similar nucleation times have been reported in the early studies of dust formation in silane containing discharges for parallel-plate reactors.[18,30,31] By the end of the nucleation phase, the particles have already reached an average size of 5.5 nm, see figure 3.6(b), and they further grow to an average size of roughly 8 nm within few centimeters before growth stops. This suggests that by the end of the nucleation phase (i.e., when the silane is fully consumed) the particles have already grown to a significant fraction of their final size. The absence of silane beyond the x= -50 mm point suggest that the particle grown from 5.5 to 8 nm via an agglomeration and coalescence process, in contrast to growth via chemical vapor deposition of unconsumed precursor onto the particle surface. We should point out that we are not suggesting that particles are instantaneously nucleated with a size of 5.5 nm. It is challenging with our

apparatus to probe smaller particles prior to the x = -50mm position because of rapid diffusional losses to the inside walls of the extraction probe.

One contribution of this work is in monitoring the particle structure during the nucleation and growth process. At a position corresponding to x= -50mm (before the first electrode), the silane has been fully depleted and the particles have an amorphous structure, see figures 3.2(a) and 3.3(a). This allows us to conclude that the formation of crystalline material in this kind of reactor is not induced by the fast nucleation and growth process, i.e., the release of the heat of condensation does not lead to the formation of particles with a crystalline structure. We have monitored the evolution of the particles structure as they travel along the length of the discharge using Raman spectroscopy, see figure 3.3. Raman spectroscopy is a quick and convenient technique for monitoring the particle structural evolution, although care should be taken when using it for the determination of the crystalline fraction within a sample. The Raman spectroscopy sensitivity to different silicon structures is modulated by stress;[32] moreover, Raman spectroscopy has also been shown to be sensible to the chemical termination of silicon nanoparticle surfaces.[23] In addition, the development of theoretical models for the precise prediction of the Raman spectra for nanostructured silicon is still an active area of research.[27] Therefore, our use of Raman spectroscopy as a characterization technique is limited to monitoring the relative changes in the particle structure as they are sampled at different axial positions, i.e., as they interact with the nonthermal plasma.

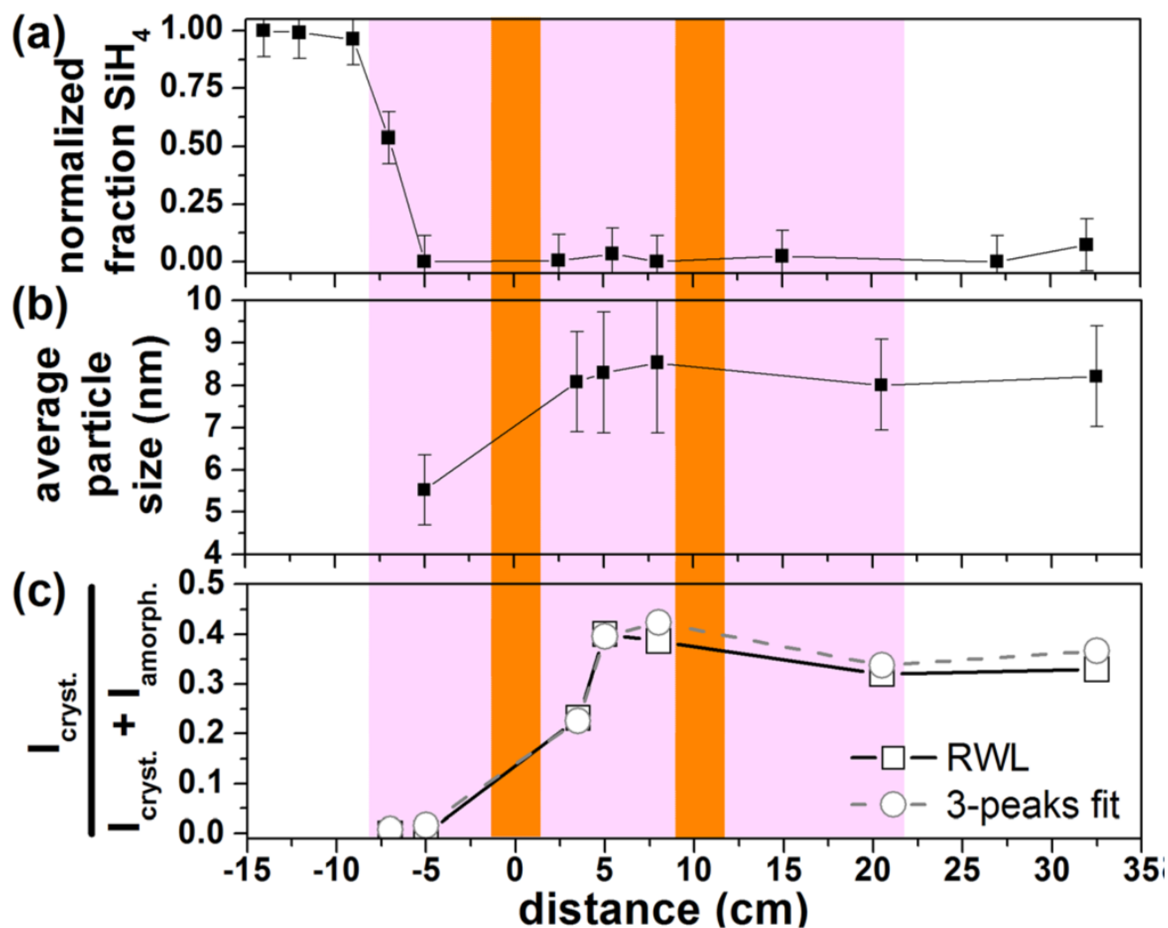

Figure 3.6. (a) Normalized absorption from SiH4 along the plasma reactor. (b) Average particle size along the plasma reactor, determined from the analysis of TEM micrographs. (c) Fraction of the Raman spectroscopy intensity due to the silicon crystalline phase over the total Raman spectroscopy signal, determined by fitting the spectra with both the RWL and the three-peaks method (see text for details). The narrow bands indicate the position of the electrodes and the wider band indicates the distance over which the plasma extends by naked eye.

In figure 3.6(c), we plot the fraction of the signal intensity due to crystalline contribution over the total area under the Raman spectroscopy signal, i.e., $I_{cryst.}$/ ($I_{cryst.}$+$I_{amorph.}$). We calculate this ratio using two different approaches. First, we use the model introduced by Richter et al.[24] (Richter-Wang-Ley, or RWL, model) to predict the shape of the crystalline peak while using a Gaussian profile centered around 480 cm^{-1} for the amorphous phase. Alternatively, we calculate the ratio with a three-Gaussian peaks fitting procedure which uses a ~480 cm^{-1} peak to predict the contribution from the amorphous phase, and two peaks centered in the 512–521 cm^{-1} range and in the 500–512 cm^{-1} range to predict the contribution from the crystalline phase. The inclusion of the intermediate peak has been used in the literature to include the effect of strained bond at the surface of small crystals.[33, 34] Both approaches yield similar results. The particles have an amorphous structure immediately at the end of the nucleation phase, consistently with the TEM image shown in figure 3.2(a). The particle structure then changes and the ratio $I_{cryst.}$/ ($I_{cryst.}$+$I_{amorph.}$) reaches a maximum value after the particles have passed the first electrode. The value then slightly decreases and reaches a plateau. Based on our TEM observation figure 3.2(c) and several other images not shown for brevity, the particles at this stage have a crystalline structure. We have reproducibly observed that the ratio $I_{cryst.}$/ ($I_{cryst.}$+$I_{amorph.}$) reaches a maximum within the discharge and then decreases slightly. This phenomenon is not understood at this point and we continue to investigate it. We note that Raman spectroscopy is sensitive not only to the particle structure but to its surface as well,[23] so our measurement may be sensitive to changes in the particle surface during

exposure to the nonthermal plasma. Nevertheless, the structure evolves from amorphous (before the first electrode, at x= -50 mm) to crystalline (at x= +50 mm) over a length of 10 cm, equivalent to a time interval of 120 ms. Under the assumption that the plasma behaves solely as a heating source because of the exothermic reaction between the particles surface and plasma-generated ions and radicals,[19,20,35,36] one can estimate the particle temperature once the nanoparticle crystallization rate is known. We have recently experimentally determined the crystallization rate for particles of the same size by performing careful in-flight thermal annealing experiments,[22] and we have found the rate to be:

Equation 3.1

$$\frac{dx_c}{dt}[\mathrm{sec}^{-1}] = 2.33 \times 10^5[\mathrm{sec}^{-1}]\exp\left(-\frac{11853}{T_p[\mathrm{K}]}\right)$$

where x_c is the crystalline fraction within the sample and T_p is the particle temperature in Kelvin. For full crystallization to occur in 120 ms and for the case of purely thermal annealing, the particles need to be heated to 1160K for the duration of the process. This value largely exceeds the nanoparticle temperature predicted in Ref. 19 when including heating via ion recombination and via reactions with atomic hydrogen. More extensive measurements of the plasma properties recently reported by the Kortshagen group[20] have led to the conclusion that 5 nm particles can be heated to a constant temperature of 750K while in the plasma. Our estimate exceeds this prediction by more than 400 K. There can be various reasons for this discrepancy. First of all the calculations reported in Ref. 20 are for particles with a maximum size of 5 nm while the particle average size in our study is

around 8 nm. The authors in the same contribution have also found that plasma properties and atomic hydrogen densities strongly depend on particle size. A more comprehensive study of the plasma properties for the case under consideration in this report will be discussed in a future contribution. In addition, our prediction of the particle temperature depends on the assumption that the phase transformation is due to a thermal annealing process. Particle heating is induced by the recombination of plasma produced species at the nanoparticle surface.[19,20] Our prediction of the particle temperature does not consider chemical effects such as the hydrogen insertion into strained Si–Si bonds, which is likely going to enhance the crystallization rate.[37] Finally, our temperature estimate may actually suggest that additional heating mechanisms, not limited to the reaction between the particle surface and species such as ion and hydrogen radicals, may be unaccounted for in the heating model used in Refs. 19 and 20. We should also mention that the particle size is not constant during the crystallization phase, with the average size growing from 5.5 to 8nm. This growth process is likely due to agglomeration and coalescence, as discussed earlier. Coalescence is well known to induce heating of the particle because of the decrease in specific surface area during growth.[38–40] Temperature increases as high as several hundred of degree Kelvin have been predicted during the sintering of small clusters (few hundreds of atoms), but in our case, the particles are much bigger (a 5.5 nm particle contains 4300 atoms) therefore the change in specific surface area during the sintering process is not as dramatic as for the case of small particles. To further verify that the sintering process itself does not heat the particles to the temperatures necessary to

observe structural transformation, we perform a simple calculation of the total energy released during the sintering of three 5.5 nm particles to give one 8 nm particles (the volume ratio between a 8 and a 5.5 nm particle is 3.077). The total surface area reduction during the process is equal to ~90 nm^2 (per particle at the end of the process). Using a value for the surface energy of silicon[41] equal to 0.9 J/m^2, we obtain a total energy release of 8.210 x 10^{-17} J per 8 nm particle. At steady state, we can estimate the amount of energy needed to maintain the estimated particle temperature of 1160K for 120 ms by calculating the energy loss to the background gas via conduction. The cooling rate is equal to:

Equation 3.2:

$$\dot{Q} = \frac{1}{4} n_{\text{gas}} S \sqrt{\frac{8 k_B T_{\text{gas}}}{\pi m_{\text{gas}}}} \cdot \frac{3}{2} k_B (T_p - T_{\text{gas}})$$

where n_{gas} is the background gas density, S is the particle surface area, T_{gas} is the background gas temperature, assumed to be 300 K, m_{gas} is the mass of the argon atom, and T_p is the particle temperature. Using this approach, which underestimates the amount of energy needed to maintain a temperature of 1160K because it neglects radiative cooling, we calculate a value of 4.11 x 10^{-12} J, which is several orders of magnitude larger than the energy released by the coalescence process.

A recurring question with respect of these kinds of reactors is whether the calculation of the particle residence time in the plasma based on the gas flow velocity is accurate, i.e., whether particles are trapped in plasma. This has important consequence

with respect of nucleation, growth and crystallization kinetics. For instance, if the particles were trapped in the plasma, the actual crystallization time would exceed the 120 ms used above to predict the particle temperature. We have found no evidence of particle trapping in our study. This conclusion is supported qualitatively by the fact that when the particles are extracted using the set-up shown in figure 3.1, the coverage of the TEM grids with particles is very similar at all the different axial positions examined here, see images in figure 3.2. More quantitatively, we have placed a filter downstream of the extraction probe, collected powder for 5 minutes and measured the amount of mass extracted at two different axial position: immediately after the second electrode while still in the plasma, and several centimeters downstream of the plasma. We have collected 0.28 mg/min in the first position and 0.3 mg/min in the second position. The error bar for these measurements, estimated by repeating the measurement ten times at each collection point, is around 0.05 mg/min. The fact that no particle trapping is observed does not necessarily mean that the particles are not negatively charged while in the plasma. If that was the case it would be possible to observe deposition of particles on the reactor wall, which we never observe. A more reasonable explanation is that the decay in the plasma density downstream of the second electrode must be sufficiently slow to avoid the formation of an electric field strong enough to trap the particles.

The appropriateness of our extraction probe design for the sampling of particles from the plasma volume also needs to be discussed. Negatively charged particles can be extracted from the plasma if the aerodynamic drag force can overcome the electrostatic

repulsion due to the presence of the sheath at the extraction orifice. We have eliminated this problem by simply using a large orifice (1mm diameter). Using reasonable estimates of plasma properties ($n_0 = 10^{10}$ cm^{-3} and $T_e = 4$ eV) one obtains a Debye length of 150 μm, much smaller than the size of the orifice. To further support the conclusion that charged particles have been successfully extracted from the plasma reactor, we report that we have always observed a faint glow extending from the plasma into the extraction probe, suggesting that the ionized gas was also extracted from the plasma reactor, likely carrying the negatively charged particles with it.

To our knowledge, FTIR has already been used for the characterization of silane-containing nonthermal plasma. Kroesen et al.[28] used an approach very similar to ours to monitor the dissociation of silane and the growth of silicon nanoparticles in a parallel- late type of reactor. The silane dissociation was monitored by observing the intensity of the 2187 cm^{-1} line. They reported that as soon as the silane was dissociated in the discharge it was possible to observe the onset of absorption in the 2100 cm^{-1} range due to surface silicon hydrides. In our case, we clearly observe a decrease in the SiH_4 signal but we do not detect any signal from surface hydrides when acquiring data from the discharge, see figure 3.5. Despite achieving a detection limit that is comparable to the one obtained by Kroesen et al.[28] (absorbance < 10^{-3}) our system is limited by the short absorption length, which is equal to the 1 in. discharge diameter. In Ref. 28, the absorption length was equal to the discharge diameter, i.e., 12 cm. Nevertheless we have performed additional measurements at lower acquisition frequency (25 vs 40 kHz) and with longer averaging (10000 vs 1000

acquisitions) compared to the ones used for the measurements shown in figure 3.5 with the goal of detecting the nanoparticle surface termination. We have performed this measurement at two locations, in the middle of the discharge length (at x = 5.5 cm) and downstream of the plasma (at x = 32.5 cm). The results, focusing on the 1900–2500 cm^{-1} range, are shown in figure 3.7.

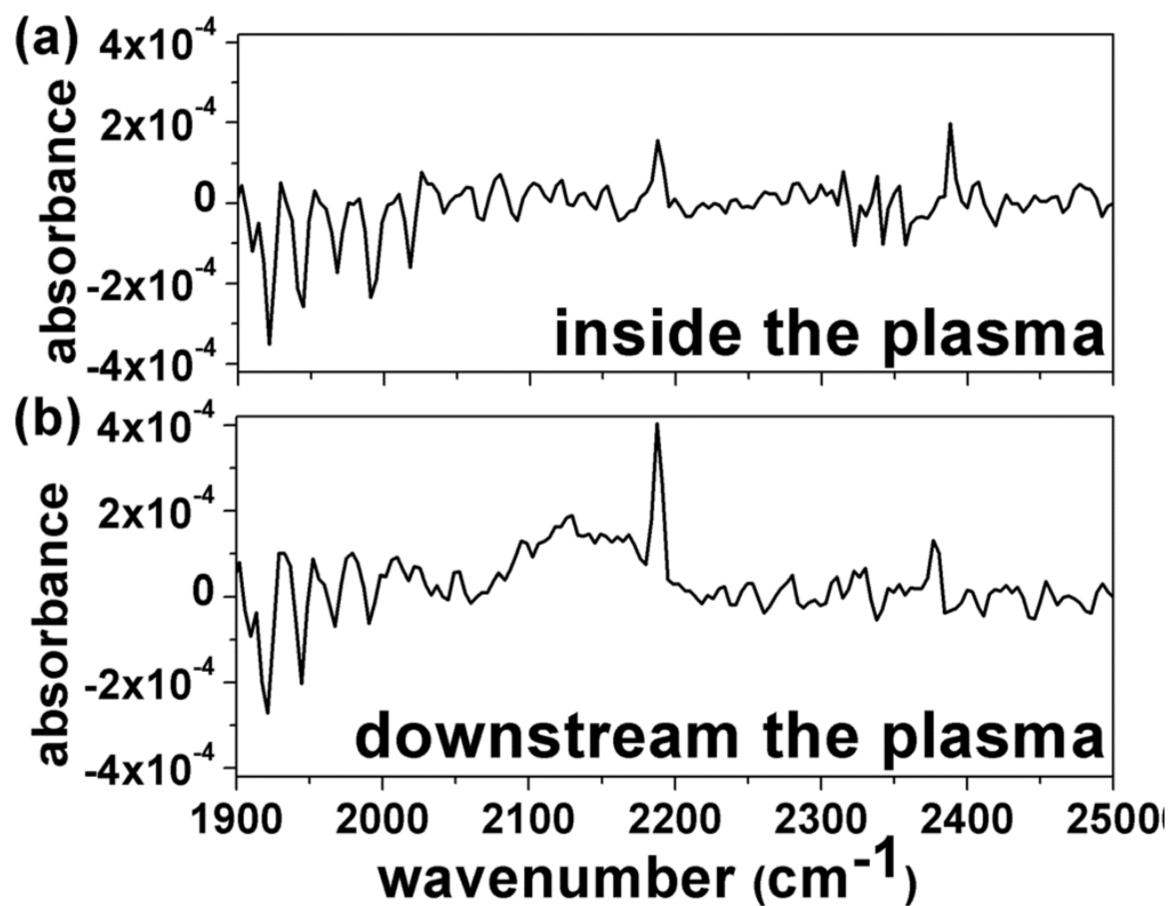

Figure 3.7. FTIR spectra in the 1900-2500 cm^{-1} range sampling at (a) x= 5.5 cm, i.e., inside the plasma and at (b) x= = 32.5 cm, downstream of the plasma

In figure 3.7(a), we can observe a detectable absorption from water in the 1900–2000 cm^{-1} range, which is likely due to a change compared to the baseline spectrum as water is desorbed from the KBr windows as the system is operated for several minutes. At the same time, small fluctuations in the CO_2 level are likely to give rise to a peak close to 2400 cm^{-1}. Absorption from residual silane is also clearly observable at 2187 cm^{-1}, although the absorbance is 2×10^{-4} compared to an absorbance of 2×10^{-2} obtained upstream of the plasma, see figure 3.5. On the left side of the silane peak, in the 2050–2150 cm^{-1} range where the signature from surface hydride species is expected to appear, there is no detectable signal above the noise level. On the other hand, in figure 3.7(b), we show the same data but acquired at x = 32.5cm position, i.e., downstream of the plasma. There is a clear signal above the noise level in the 2050–2150 cm^{-1} range. Small absorbance from silane is observed but at a much lower level than what is measured upstream of the discharge (4×10^{-4} vs 2×10^{-2}). At this point, we cannot conclude that the particles have a hydrogen-free surface as they are immersed in the plasma because of limitation in our detection limit. We are continuously working on improving the sensitivity of the system. On the other hand, the data shown in figure 3.7 indicate that a stronger absorption from surface Si-H_x moieties is measured after the particles exit the plasma volume. This behavior is consistent with the fact that particles in the plasma may be too hot to have a high degree of hydrogen termination. Hydrogen desorption from silicon surfaces is well-known to occur at temperatures higher than 600 ^{0}C (900K). In Ref. 22, we have performed in-flight annealing experiments and we have confirmed that significant hydrogen desorption from

the surface of silicon nanoparticles occurs by the time they are heated to 600 ^{0}C. The fact that the signal from surface silicon hydride is detectable when the particles are outside of the plasma but not when they are immersed in the plasma supports the conclusion that significant nanoparticle heating occurs in the discharge. The fact that Kroesen et al.[28] successfully detect surface hydride species in their measurements is likely due to the longer absorption length, as discussed earlier, but also due to the fact that the power density in the parallel plate reactor used for their study (3 W input power for a 12 cm diameter discharge with a 5 cm gap, corresponding to ~5 x 10^{-3} W/cm^3) is significantly lower than the one used in our reactor (90 W input power for a 2 cm diameter column with a length of 20 cm, equal to 1.4 W/cm^3), leading to substantially lower nanoparticle temperatures.

3.6 Conclusion

We have performed *in-situ* FTIR measurements to monitor the consumption of silane in a continuous flow nonthermal plasma reactor. In combination with this measurement, we have extracted and characterized the size and structure of the particles as they are carried along the length of the plasma. We have found that silane is consumed within few tens of milliseconds. At the end of the nucleation phase, the particles have an amorphous structure. Crystallization takes place as the particles interact with the partially ionized gas over a time period of 120 ms for the conditions under consideration. Using a recently measured crystallization rate for silicon particles of the same size, and under the assumption that the phase transformation is due to the heating induced by the recombination of plasma-produced species at the particle surface, we can estimate the particle temperature in the plasma. We find this value to be ~1160K for these particular conditions. We also observe an increase in the absorption from surface silicon hydride species when the particles exit the discharge, suggesting that sufficient nanoparticle heating occurs in the plasma to induce hydrogen desorption. These measurements underlie that a precise understanding of the interaction between nanoparticles and nonthermal plasmas has yet to be reached.

3.7 Acknowledgements

This work was supported by the U.S. Department of Energy, Office of Basic Energy Sciences, Division of Materials Sciences and Engineering under Award No. DESC0008934.

3.8 References

1. A. Bouchoule, A. Plain, L. Boufendi, J. P. Bloundeau, and C. Laure, J. Appl. Phys. 70, 1991 (1991).

2. M. Shiratani, S. Matsuo, and Y. Watanabe, Jpn. J. Appl. Phys., Part 1 30, 1887 (1991).

3. U. Kortshagen, J. Phys. D: Appl. Phys. 42, 113001 (2009).

4. Y. Watanabe, J. Phys. D: Appl. Phys. 39, R329 (2006).

5. L. Mangolini, J. Vac. Sci. Technol., B 31, 020801 (2013).

6. L. Mangolini, E. Thimsen, and U. Kortshagen, Nano Lett. 5, 655 (2005).

7. O. Yasar-Inceoglu, T. Lopez, E. Farshihagro, and L. Mangolini, Nanotechnology 23, 255604 (2012).

8. R. Gresback, T. Nozaki, and K. Okazaki, Nanotechnology 22, 305605 (2011).

9. I. Dogan, N. J. Kramer, R. H. J. Westermann, K. Dohnalova, A. H. M. Smets, M. A. Verheijen, T. Gregorkiewicz, and M. C. M. van de Sanden, J. Appl. Phys. 113, 134306 (2013).

10. C.-Y. Liu, Z. C. Holman, and U. R. Kortshagen, Nano Lett. 9, 449 (2009).

11. K.-Y. Cheng, R. J. Anthony, U. Kortshagen, and R. J. Holmes, Nano Lett. 10, 1154 (2010).

12. L. Zhong, J. Guo, and L. Mangolini, J. Power Sources 273, 638 (2015).

13. R. Gresback, Z. Holman, and U. Kortshagen, Appl. Phys. Lett. 91, 093119 (2007).

14. E. Thimsen, U. R. Kortshagen, and E. S. Aydil, Chem. Commun. 50, 8346 (2014).

15. R. Gresback, R. Hue, W. L. Gladfelter, and U. R. Kortshagen, Nanoscale Res. Lett. 6, 68 (2011).

16. P. Felbier, J. H. Yang, J. Theis, R. W. Liptak, A. Wagner, A. Lorke, G. Bacher, and U. Kortshagen, Adv. Funct. Mater. 24, 1988 (2014).

17. A. Kumar, P. Ann Lin, A. Xue, B. Hao, Y. Khin Yap, and R. M. Sankaran, Nat. Commun. 4, 2618 (2013).

18. A. Bouchoule and L. Boufendi, Plasma Sources Sci. Technol. 2, 204 (1993).

19. L. Mangolini and U. Kortshagen, Phys. Rev. E 79, 026405 (2009).

20. N. J. Kramer, R. J. Anthony, M. Mamunuru, E. S. Aydil, and U. R.Kortshagen, J. Phys. D: Appl. Phys. 47, 075202 (2014).

21. Z. Iqbal and S. Veprek, J. Phys. C: Solid State Phys. 15, 377 (1982).

22. T. Lopez and L. Mangolini, Nanoscale 6, 1286 (2014).

23. C. M. Hessel, J. Wei, D. Reid, H. Fujii, M. C. Downer, and B. A. Korgel,J. Phys. Chem. Lett. 3, 1089 (2012).

24. H. Richter, Z. P. Wang, and L. Ley, Solid State Commun. 39, 625 (1981).

25. V. Paillard, P. Puech, M. A. Laguna, R. Carles, B. Kohn, and F. Huisken, J. Appl. Phys. 86, 1921 (1999).

26. G. Faraci, S. Gibilisco, P. Russo, A. R. Pennisi, and S. La Rosa, Phys. Rev. B 73, 033307 (2006).

27. G. Faraci, S. Gibilisco, A. R. Pennisi, and C. Faraci, J. Appl. Phys. 109, 074311 (2011).

28. G. M. W. Kroesen, J. denBoer, L. Boufendi, F. Vivet, M. Khouli, A. Bouchoule, and F. J. deHoog, J. Vac. Sci. Technol., A 14, 546 (1996).

29. R. Bartlome, A. Feltrin, and C. Ballif, Appl. Phys. Lett. 94, 201501 (2009).

30. L. Boufendi and A. Bouchoule, Plasma Sources Sci. Technol. 3, 262 (1994).

31. T. Fukuzawa, H. Kawasaki, M. Shiratani, and Y. Watanabe, Jpn. J. Appl. Phys., Part 1 33, 4212 (1994).

32. C. Ossadnik, S. Veprek, and I. Gregora, Thin Solid Films 337, 148 (1999).

33. Q. J. Cheng, S. Y. Xu, S. Y. Huang, and K. Ostrikov, Cryst. Growth Des. 9, 2863 (2009).

34. Z. Li, W. Li, Y. Jiang, H. Cai, Y. Gong, and J. He, J. Raman Spectrosc. 42, 415 (2011).

35. J. E. Daugherty and D. B. Graves, J. Vac. Sci. Technol., A 11, 1126 (1993).

36. D. B. Graves, J. E. Daugherty, M. D. Kilgore, and R. K. Porteous, Plasma Sources Sci. Technol. 3, 433 (1994).

37. S. Sriraman, S. Agarwal, E. S. Aydil, and D. Maroudas, Nature 418, 62 (2002).

38. M. R. Zachariah and M. J. Carrier, J. Aerosol Sci. 30, 1139 (1999).

39. K. E. J. Lehtinen and M. R. Zachariah, Phys. Rev. B 63, 205402 (2001).

40. K. E. J. Lehtinen and M. R. Zachariah, Aerosol Sci. 33, 357 (2002).

41. T. Hawa and M. R. Zachariah, J. Chem. Phys. 121, 9043 (2004).

Chapter 4

Thermal effects in the non-thermal plasma processing of nanoparticles

4.1 Abstract

It has been theoretically predicted that nanoparticles can exceed the background gas temperature by several hundreds of degrees while suspended in a non-thermal plasma. The implications of this non-equilibrium condition on the materials processing capabilities of such systems are still far from fully understood. Moreover, the temperature of a nanoparticle dispersed in processing dusty plasma has never been experimentally determined. We have addressed this unresolved issue by monitoring the evolution of the surface termination of silicon nanoparticles immersed in an argon-hydrogen plasma via *in-situ*, *in-flight* FTIR. We have found that the hydrogen surface coverage monotonically decreases as the plasma power is increased. Control experiments indicate that the loss of hydrogen from the particle surface is the result of a thermally induced desorption process. By using well-established kinetic rates for hydrogen interactions with silicon surfaces (attachment, abstraction and desorption), we estimate the nanoparticle temperature to be in the 650K-750K range for the conditions of this study. This range is in agreement with previous theoretical prediction and confirms the potential of dusty plasmas as a nanopowder synthesis and processing technique.

4.2 Introduction

The number of contributions reporting the synthesis of high-quality nanoparticles using non-thermal plasmas is rapidly increasing. These novel plasma processing systems are capable of producing nanocrystals of silicon[1] and silicon-based alloys[2, 3], zinc oxide[4], carbon diamond[5], metal sulfides[6, 7], to name a few. In these type of processes, the precursor is fully consumed and converted into nanocrystals within tens of milliseconds, while the background gas temperature remains close to room temperature[8]. Theory predicts that recombination of plasma-produced species (ions and radicals) lead to substantial heating, with nanoparticle temperature exceeding the background gas temperature by a few hundred kelvin[9-11]. This likely leads to the formation of high-quality crystalline nanostructures even for high melting point materials. In this contribution, we use *in-flight* FTIR to monitor the surface of silicon nanoparticles immersed in a non-thermal plasma. For the first time, empirically confirming that significant particle heating occurs in this class of non-equilibrium materials processing system.

4.3 Experimental

The reactor used for this study is based on the design described in [8], and its schematic is shown in figure 4.1. The reactor consists of two consecutive plasma reactors, each one with its own set of independently powered electrodes. The first reactor is composed of a 9.5 mm diameter Pyrex tube with a pair of radio frequency biased (RF, 13.56 MHz) ring electrodes, and converts silane into silicon nanocrystals with an average size of 5 nm, as confirmed via extensive TEM characterization (not shown here for brevity). The silane (1.37% by volume in argon) flow rate, for the dataset discussed in this manuscript, is 70 sccm. An additional inlet is placed at the exit of the first plasma to add 30 sccm of hydrogen to the gas mixture. The addition of hydrogen immediately at the exit of the plasma has been shown to lead to a higher degree of passivation of the surface[12]. The nanoparticles are then aerodynamically dragged to a 90° angle and into the second plasma, where they are treated *in-flight* with varying RF plasma input power. The second reactor consists of a 50 cm long Pyrex tube with a 25.4 mm outer diameter. Two flat, 30 cm long copper plates are used as electrodes to sustain the discharge in the second reactor. An automatically controlled valve is used to maintain the reactor pressure at 3.5 Torr. UHV fittings designed to host IR-transparent potassium bromide (KBr) windows are placed at either ends of the second reactor. An IR beam is sent through the length of the second reactor to monitor changes in the surface of the nanoparticles produced in the first plasma via *in-flight*, open-path FTIR, as a function of the plasma input power to the second discharge. The long optical path of this design optimizes the sensitivity for

monitoring the nanoparticle surface. IR spectra are acquired using a modular FTIR system from Newport-Oriel with a 4 cm^{-1} resolution and averaged over 2000 acquisitions to maximize the signal to noise ratio.

The second reactor is fitted with a side port to gain access to the second plasma for additional characterization. The side port is used to perform ion density measurement via a capacitive probe [13]. A 1 mm diameter copper wire with an exposed length of 3 mm is placed in the center of the secondary plasma and connected in series to a 30 pF capacitor. The circuit is biased at 16 MHz using an RF amplifier. The signal is amplitude-modulated with a 60 kHz square wave. The ion density measurement is obtained by monitoring the discharge rate of the capacitor during the off-phase of the square wave modulation.

Optical emission spectroscopy measurements of the second discharge are performed using an optical fiber and a Newport-Oriel 1/4m monochromator with a silicon photodetector. The monochromator and photodiode are controlled via Labview. The system response is calibrated using a NIST traceable white light source from Ocean Optics Inc.

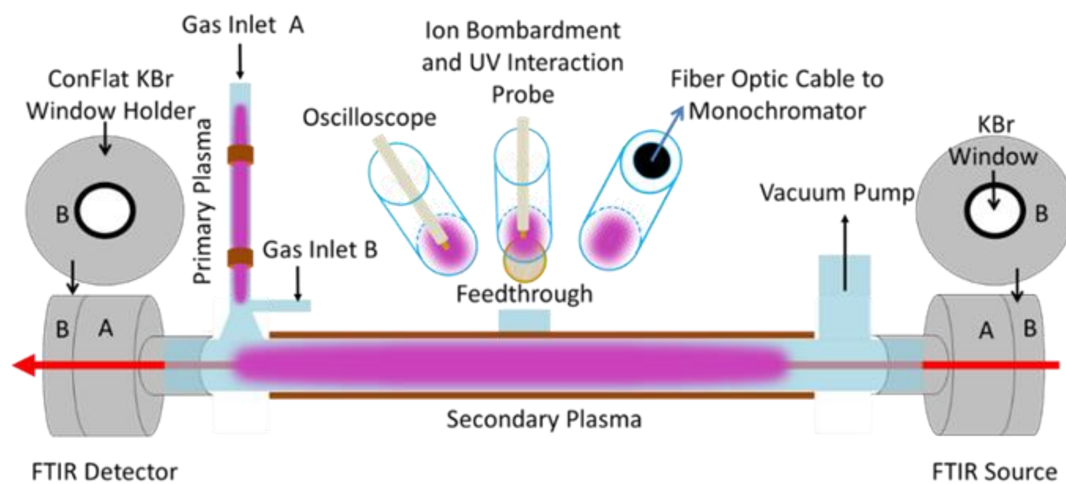

Figure 4.1. Schematic of reactor used for the *in-flight in-situ* characterization of silicon nanoparticles.

4.4 Results and discussion

Figures 4.2, 4.3, and 4.4 summarize the results of the FTIR measurements performed using the system described above. In figure 4.2 we show the absorbance spectrum of silicon nanoparticles without any power supplied to the second reactor (plasma off). The use of silane as precursor leads to silicon nanoparticles with a hydrogen-terminated surface[14]. The peaks at 868 cm^{-1} and 906 cm^{-1} can be attributed to deformation and wagging modes of SiH_3 and SiH_2 surface groups[15]. The broader peak centered around 2100 cm^{-1} is attributed to SiH_x ($1 < x < 3$) stretching modes[15]. We point out that the sharp peak at 2187 cm^{-1} is due to the absorbance from silane[16]. Without the first plasma on (i.e. without consuming the precursor) we measure an absorbance from silane around 3×10^{-2}, confirming that the precursor is practically fully consumed in the first plasma and that the nanoparticles are exposed to an argon-hydrogen plasma in the second reactor. The signal-to-noise ratio is minimized around 2000 cm^{-1}, since the IR source has maximum intensity in this region of the spectrum. The noise level at 2000 cm^{-1}, measured by acquiring two consecutive scans when only argon is flowing and by calculating the corresponding absorbance, is below 10^{-4}. There is residual absorbance from CO_2 at 2250 cm^{-1} and water at 1500 cm^{-1} in the scan shown in figure 4.2. . Their appearance in the spectra does not imply that CO_2 and water are present in the plasma reactor, rather, CO_2 and water cannot be completely eliminated from the instrument compartment even after extensive purging. Extreme care is taken to minimize leakage

rate of the reactor assembly, and all the gasses used in this study are ultra-high purity grade.

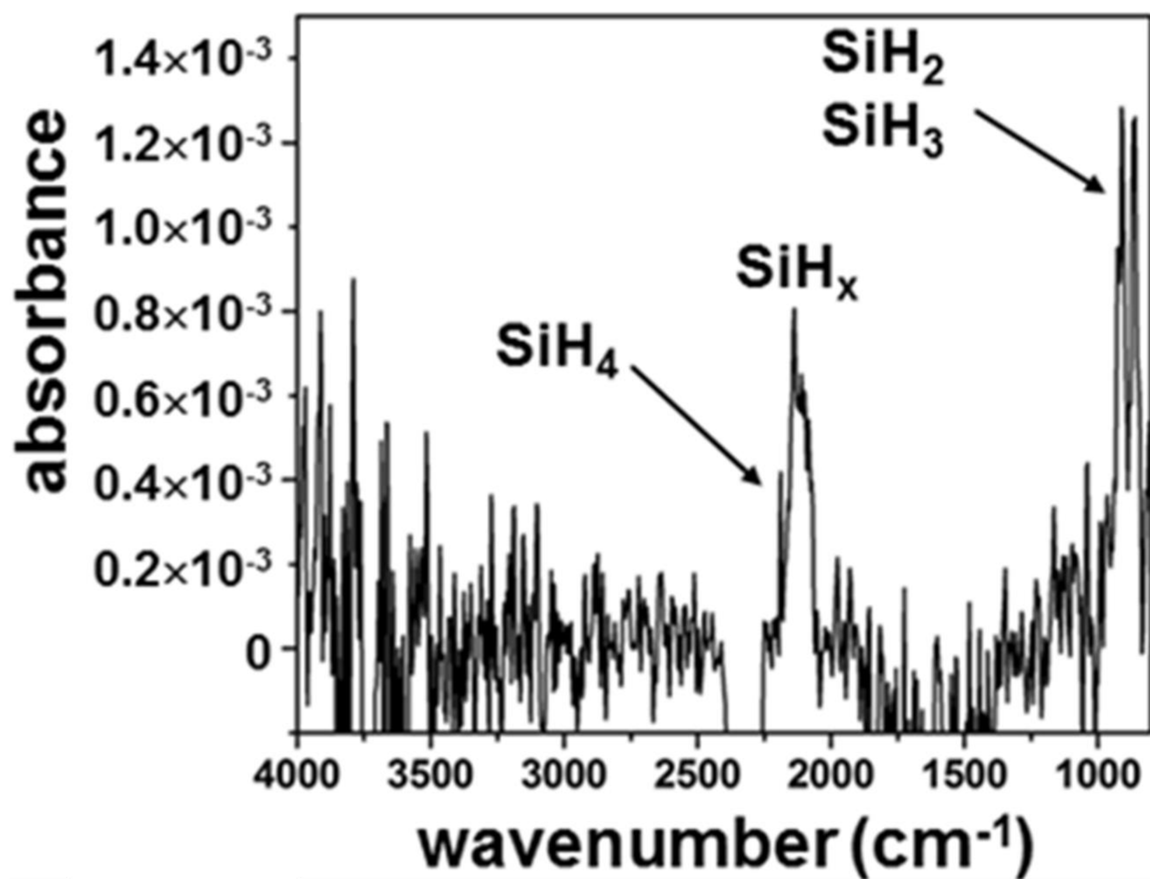

Figure 4.2. In-flight IR absorbance spectrum for silicon nanoparticles without plasma in the second reactor.

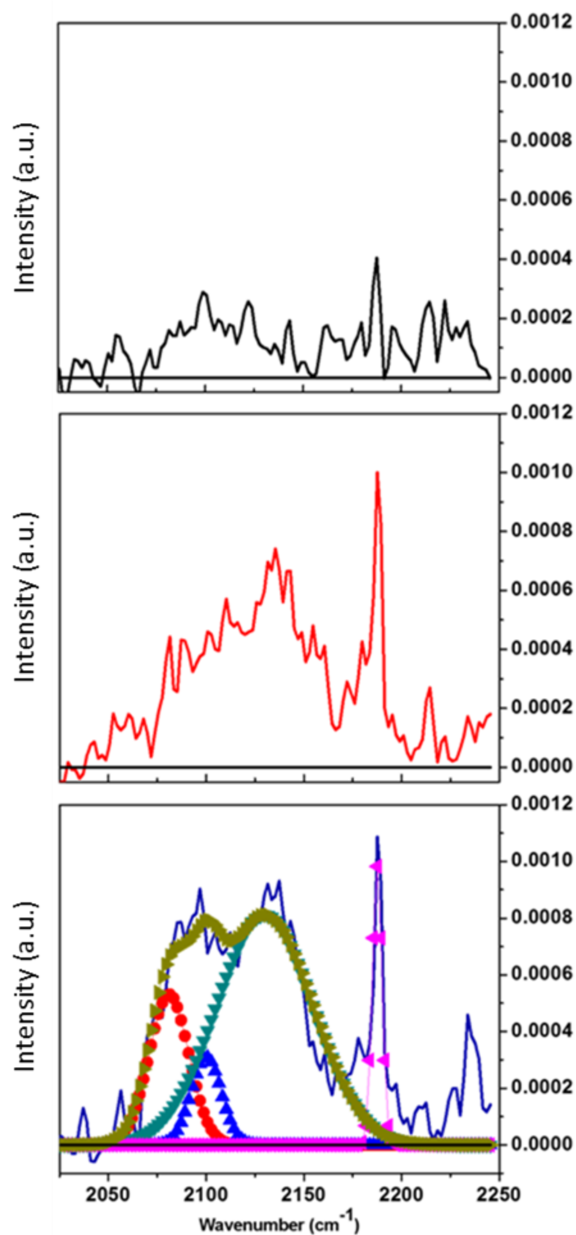

Figure 4.3. 2100 cm-1 (SiHx) peak intensity at increasing second plasma power (Power increase from bottom to top)

Figure 4.3 shows the absorbance from the SiH_x peak centered at 2100 cm^{-1}, measured at increasing power in the second plasma. The peak centered at 2100 cm^{-1} has been fitted using three Gaussian peak profiles centered at 2080 cm^{-1} (SiH), 2110 cm^{-1} (SiH_2) and 2135 cm^{-1} (SiH_3)[15]. The total area under these peaks is plotted as a function of RF plasma power to the second discharge in figure 4.4, showing a clear decrease in absorbance from surface hydride moieties at increasing input power. In the same plot we show the absorbance from the SiH_x peak at 2100 cm^{-1} as a function of input power for the case of particles collected onto a high transparency stainless steel mesh. The stainless steel mesh is positioned in the optical path of the IR beam and at the centerline of the second reactor. The mesh is also electrically isolated i.e. at a floating potential. Powder is first collected onto the mesh with only the first plasma on. The particles are then exposed to the second plasma at varying powers for 1 second at each power. In this case, the plasma is generated in the same argon-hydrogen mixture and at the same pressure as for the *in-flight* measurement case. The absorbance remains constant over the same range of RF input power. Hydride species are effectively removed from the nanoparticle surface when the particles are freestanding in the plasma, while this does not happen when the particles are supported by the filter mesh. We would like to stress that the plasma exposure time in this case is 1 second, which is much longer than the residence time of the particles in the plasma for the *in-flight* measurement case (200 milliseconds, based on flow velocity). Since the second plasma is generated under nominally identical conditions for these two measurements (in-flight and supported by a mesh), we conclude

that ion bombardment to the particle surface and exposure to plasma-generated UV radiation does not lead to effective abstraction of hydrogen from the particle surface for the conditions of this study. For the particle-on-filter case, the nanoparticles are in contact with a heat sink that prevents significant temperature increase during the 1-second plasma treatment. For the freestanding case, the particles cannot efficiently dissipate the energy generated by recombination reactions occurring at the particle surface because of the low background gas pressure, leading to an increase in nanoparticle temperature. The reduction in surface hydrogen coverage is a result of thermally-induced desorption.

We have carefully verified that any decrease in the absorption from the SiH_x signal is not induced by a decrease in nanoparticle density in the second plasma at increasing RF input power. We have placed a filter downstream of the second reactor and measured the same nanoparticle collection rate (50 mg/hour) whether the second plasma reactor is off or run with an input power of 80 W. Using this production rate we calculate the nanoparticle density in the plasma to be equal to 2×10^{10} cm^{-3}. This is lower than the ion density in the discharge, which we have found to be 1.8×10^{11} cm^{-3} for an input power of 80 W using the electrostatic probe system described above. This suggests that the particles have a unipolar and negative charge distribution during treatment in the second plasma[17]. TEM characterization, not shown here for brevity, also confirms that there are no changes in the particle size and structure during exposure to the second plasma.

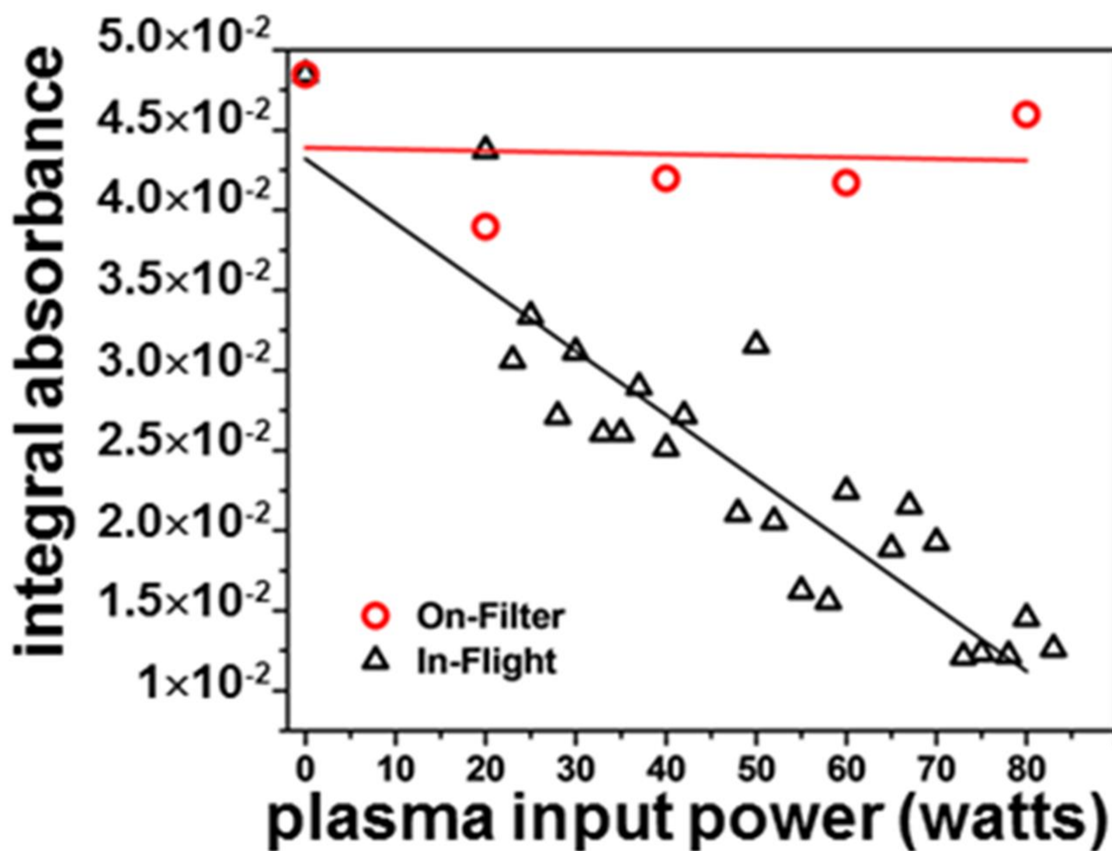

Figure 4.4. Integral absorbance from the 2100 cm-1 peak as a function of second plasma power, for the in-flight case and for the case of particles collected onto a filter placed in the second plasma.

The absorbance from the SiH_x stretching modes at 2100 cm^{-1} is ~$8x10^{-4}$ for the 0 W (second plasma off) case. Using an absorption cross section of $6.35x10^{-19}$ cm^2 [18] for the SiH group, together with the nanoparticle density in the plasma ($2x10^{10}$ cm^{-3}), an absorption length of 30 cm and a 13% fraction of atoms at the surface of a 5 nm particle, we predict the absorbance from SiH to be $9x10^{-4}$, in excellent agreement with the experimental data.

It is possible to use the fractional surface coverage of hydrogen on the particle surface, which can be calculated from the data in figure 4.4 by normalizing over the absorbance at 0 W (without any plasma in the second discharge), to obtain an estimate of the nanoparticle temperature. This can be done by comparing the experimental surface coverage with the predicted hydrogen coverage as a function of temperature and atomic hydrogen flux to the surface. The atomic hydrogen-induced attachment and abstraction rates on silicon surfaces are well characterized and taken from [19]. The thermally induced desorption rate is also well-characterized, and we use the rate measured in [20].

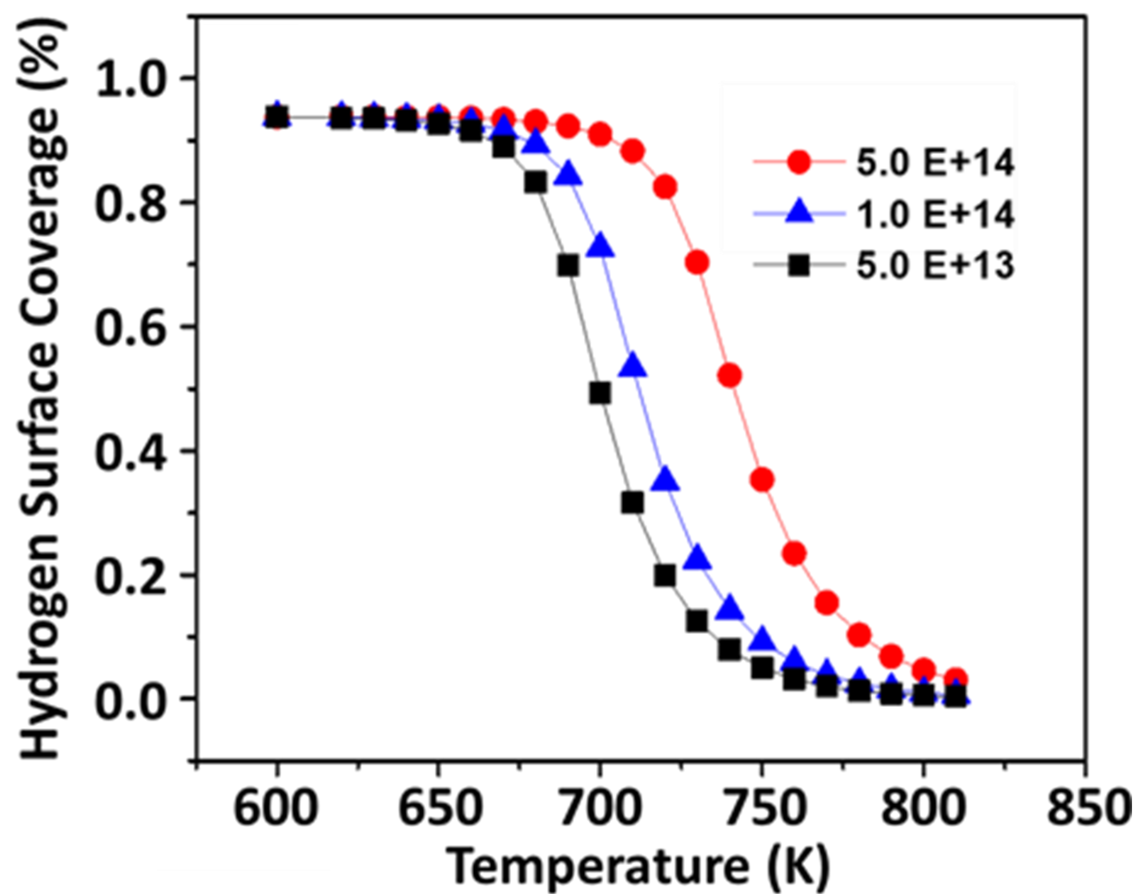

Figure 4.5. Fractional hydrogen surface coverage on a silicon surface as a function of substrate temperature and for different values of atomic hydrogen density in the gas phase.

In figure 4.5 we show the predicted surface coverage as a function of temperature for three different values (5×10^{14}, 10^{15} and 5×10^{15} cm^{-3}) of atomic hydrogen density in the gas-phase. An increase in atomic hydrogen density leads to, as expected, a delay in the onset of thermal desorption. The exponential dependence of desorption rate on temperature leads to a weak dependence of desorption temperature on atomic hydrogen density, with less than a 50K change in temperature (from 660K to 700K at 50% surface coverage) for an order of magnitude change in atomic hydrogen density. Nevertheless, we measure the atomic hydrogen density in the second discharge to obtain a reasonably precise estimate of nanoparticle temperature. The atomic hydrogen density is measured using the line intensity ratio between the 656.27 nm H_α line and the 811.53 nm argon line, under the assumption that the electronic excitation process is dominated by electron-impact induced excitation from the ground level. These lines were selected because they are close in excitation threshold (12.087 eV for the hydrogen line and 13.075 eV for the argon line). The line intensities were measured using the OES set-up described earlier. Branching ratios were calculated from the NIST atomic spectra database [21]. The electron impact induced excitation rates have been calculated using the cross section obtained from [22] for the hydrogen transition and from [23] for the argon transition. The electron energy distribution function (EEDF) has been calculated using the freeware Boltzmann solver BOLSIG+ (version July 2015)[24], under conditions of an argon-hydrogen mixture and with electron temperature varying between 3 eV and 5 eV. The electron temperature T_e is a free parameter since it is not trivial to determine its value

experimentally. The authors in [9], while investigating a very similar system (silicon nanoparticles in an argon-hydrogen plasma), used a Corona model and obtained a good fit between the measured OES data and the predicted line intensities for T_e = 4 eV. The authors in [25] performed Langmuir probe measurements on a similar gas-phase chemistry and also obtained T_e = 4 eV. We conclude that it is reasonable to vary T_e between 3 eV and 5 eV. Figure 4.6 shows the atomic hydrogen density as a function of input power to the second plasma, assuming T_e = 3, 4, and 5 eV.

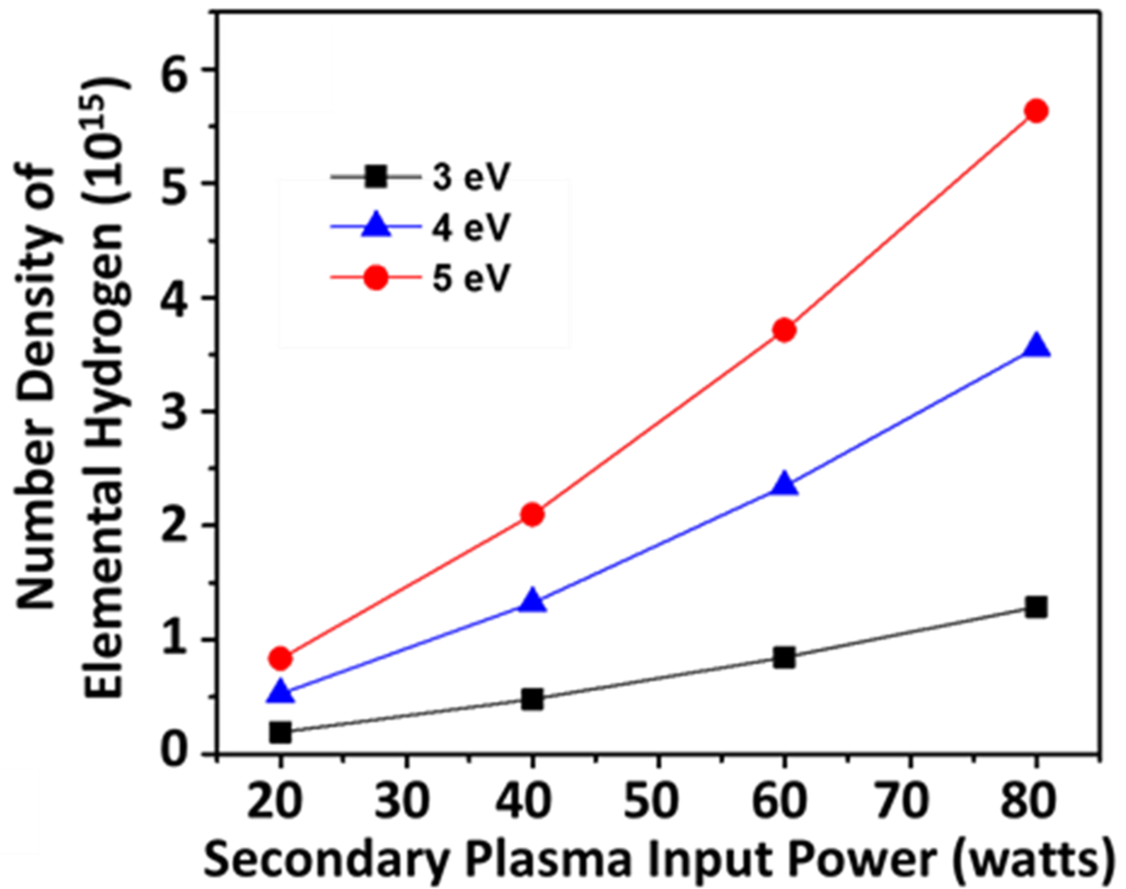

Figure 4.6. Measured atomic hydrogen density in the second plasma as a function of input power, for different values of parameter T_e (electron temperature).

Using these atomic hydrogen densities and the surface coverage derived from figure 4.4, we obtained the nanoparticle temperature shown in figure 4.7. These data are plotted as a function of RF power density in the second discharge. Three sets of data are obtained, each one corresponding to an assumed value of electron temperature. While there is variation depending on the assumed electron temperature value, we consistently estimate the nanoparticle temperature to be in the 650K-750K range, with a linear increase in temperature with RF input power. This is consistent with the theoretical prediction reported in [10], and also consistent with the nanoparticle temperature that we predicted in [26] by measuring the kinetics of structural evolution (from amorphous to crystalline) for silicon nanoparticles immersed in a non-thermal plasma.

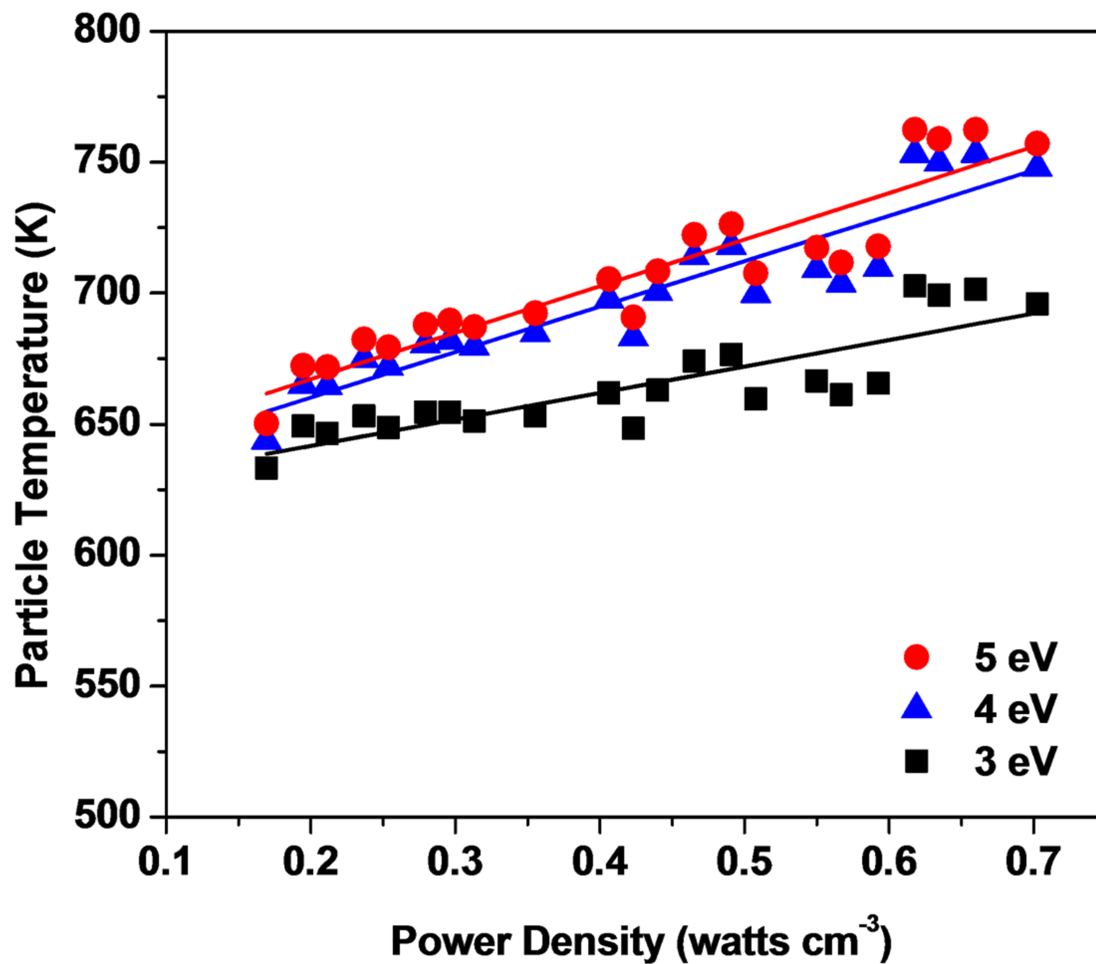

Figure 4.7. Nanoparticle temperature as a function of plasma power density.

4.5 Conclusions

We have used *in-situ*, *in-flight* FTIR to monitor the surface of silicon nanoparticles immersed in a partially ionized gas. We experimentally verified, for the first time, that a thermal effect leads to rapid desorption of hydrogen from the particle surface, and we use this observation to estimate the temperature of nanoparticles as a function of plasma input power. The nanoparticle temperature can be easily controlled by varying input parameters and can exceed the gas temperature by few hundred kelvin, all while the particles remain isolated and freestanding in the gas phase. This work provides additional confirmation that the potential of non-thermal plasmas as a nanopowder synthesis and processing tool remains to be fully explored.

This work was supported by the U.S. Department of Energy, Office of Basic Energy Sciences, Division of Materials Sciences and Engineering under Award No. DESC0008934.

4.6 References

[1] L. Mangolini, Journal of Vacuum Science & Technology B: Microelectronics and Nanometer Structures **31**, 020801 (2013).

[2] D. Coleman, T. Lopez, O. Yasar-Inceoglu, and L. Mangolini, J. Appl. Phys. **117**, 193301 (2015).

[3] O. Yasar-Inceoglu and L. Mangolini, Materials Letters **101**, 76 (2013).

[4] E. Thimsen, M. Johnson, X. Zhang, A. J. Wagner, K. A. Mkhoyan, U. R. Kortshagen, and E. S. Aydil, Nat Commun **5** (2014).

[5] A. Kumar, P. Ann Lin, A. Xue, B. Hao, Y. Khin Yap, and R. M. Sankaran, Nat Commun **4** (2013).

[6] T. Elijah, R. K. Uwe, and S. A. Eray, Journal of Physics D: Applied Physics **48**, 314004 (2015).

[7] E. Thimsen, U. R. Kortshagen, and E. S. Aydil, Chem. Commun. **50**, 8346 (2014).

[8] L. Mangolini, E. Thimsen, and U. Kortshagen, Nano Letters **5**, 655 (2005).

[9] L. Mangolini and U. Kortshagen, Physical Review E **79**, 026405 (2009).

[10] N. J. Kramer, R. J. Anthony, M. Mamunuru, E. S. Aydil, and U. R. Kortshagen, Journal of Physics D: Applied Physics **47**, 075202 (2014).

[11] N. J. Kramer, E. S. Aydil, and U. R. Kortshagen, Journal of Physics D: Applied Physics **48**, 035205 (2015).

[12] R. J. Anthony, D. J. Rowe, M. Stein, J. Yang, and U. Kortshagen, Advanced Functional Materials **21**, 4042 (2011).

[13] N. Braithwaite, J. P. Booth, and C. Cunge, Plasma Sources Sci. Technol. **5**, 677 (1996).

[14] O. Yasar-Inceoglu, T. Lopez, E. Farshihagro, and L. Mangolini, Nanotechnology **23**, 255604 (2012).

[15] D. C. Marra, E. A. Edelberg, R. L. Naone, and E. S. Aydil, J. Vac. Sci. Technol. A **16**, 3199 (1998).

[16] R. Bartlome, A. Feltrin, and C. Ballif, Applied Physics Letters **94** (2009).

[17] U. Kortshagen and U. Bhandarkar, Phys. Rev. E **60**, 887 (1999).

[18] P. Gupta, V. L. Colvin, and S. M. George, Phys. Rev. B **37**, 8234 (1988).

[19] A. Dinger, C. Lutterloh, and J. Küppers, Chemical Physics Letters **311**, 202 (1999).

[20] U. Höfer, L. Li, and T. F. Heinz, Phys. Rev. B **45**, 9485 (1992).

[21] available at: http://www.nist.gov/pml/data/asd.cfm

[22] P. M. Stone, Y.-K. Kim, and J. P. Desclaux, Journal of Research of the National Institute of Standards and Technology **107**, 327 (2002).

[23] J. B. Boffard, B. Chiaro, T. Weber, and C. C. Lin, Atomic Data and Nuclear Data Tables **93**, 831 (2007).

[24] G. J. M. Hagelaar and L. C. Pitchford, Plasma Sources Science and Technology **14**, 722 (2005).

[25] N. Bilik, R. Anthony, B. A. Merritt, E. S. Aydil, and U. R. Kortshagen, Journal of Physics D: Applied Physics **48**, 105204 (2015).

[26] T. Lopez and L. Mangolini, Journal of Vacuum Science & Technology B **32**, 061802 (2014).

Chapter 5

Application of Continuous Flow Non-thermal Plasma Produced Particles for Thermoelectric Application

5.1 Abstract

Continuous flow non-thermal plasma reactors give the ability of controlling size, structure, and surface termination of nanoparticles. This unique capability allows achieving an unprecedented degree of control on the structure of bulk materials obtained via the densification of plasma-produced nanoparticles. In particular, we apply this technique to produce bulk-sized samples of nanostructured silicon and we investigate the influence of nanoparticle processing conditions on transport properties.

5.2 Introduction

Silicon nanoparticles draw considerable attention due to their interesting properties[1] and their broad range of potential applications. These applications include solar cells[2], high powered LEDs[3,4], and thermoelectric devices[5], to name a few. Moreover silicon is the second most abundant element found in the earth's crust, making it an inexpensive semiconductor material and ideal for large-scale applications. Silicon nanoparticles are made in many different ways, such as by mechanical ball milling of bulk samples[6], via laser ablation of silicon targets[7], via pyrolysis of silane in tube furnaces[8], via laser pyrolysis of silane[9], and by non-thermal plasmas[10-12]. Continuous flow non-thermal plasma reactors have been shown to be able to control size[13], structure[10], and surface termination[11] independently of each other by adjusting different plasma input parameters, i.e., power, pressure, gas selection and volumetric gas flow[10-12]. Continuous flow non-thermal plasma reactors also have the ability to be scaled-up allowing for the production of silicon nanopowders at hundreds of milligrams per hour at the lab scale.

Typically, silicon nanoparticle powders are densified using either spark plasma sintering[5] or hot pressing[14,15]. A direct correlation between densification kinetics and particle size, structure, and surface termination has yet to be developed. In addition, a direct correlation between the physical properties of densified samples (such as thermal and electrical transport properties) and the properties of the feedstock powder is missing even for well-established materials such as silicon. The ability to precisely control

nanoparticle size, structure and surface termination before sintering may enable the optimization of the transport properties in bulk nanostructured materials obtained after the sintering of such powders, which in turn may improve the power conversion efficiency in thermoelectric devices.

For the first time silicon nanoparticles produced via continuous flow non-thermal plasmas have been densified by means of hot pressing, i.e., in a high pressure, high temperature process. This contribution will focus on the correlations between initial particle size, structure, and surface termination and the properties of the resulting nanostructured bulk material.

5.3 Experimental setup and procedures

5.3.1 Plasma process parameters

A continuous flow nonthermal plasma reactor (CFNTPR), as reported on earlier in chapters 2-4, has been optimized to create silicon nanoparticles at a rate of 100's of milligrams per hour, this reactor is shown in figure 5.1. The reactor used in this experiment is comprised of three different sections. The first is a 25 cm long quartz tube with a 5 cm diameter, connections are made on either side by ultratorr vacuum fittings. The plasma in this reactor is run with 850 sccm of silane (SiH4, 1.38% by volume in argon). A ring electrode 5 cm long is coupled 2.75 cm upstream to the ultratorr vacuum fitting. The plasma is sustained using a 13.56 MHz power supply and a T-matching network for minimization of the reflected power. The plasma input power is 160 watts and the pressure is maintained at 3.5 Torr via a butterfly valve that is located downstream of the collection point. These conditions produce hydrogen terminated crystalline silicon particles that are 5-10 nm in size. The second part of the reactor is a 70 cm long quartz tube with a 5 cm diameter placed in a MTI model OTF-1200X tube furnace. This section of the reactor is the in-flight annealing stage. The tube furnace is set to either 800 °C, 900 °C, 1000^{0}C or 1100 °C, depending on the desired particle size, see figure 5.2. It is also important to note that particles were created at lower in-flight annealing temperatures, but densified samples produced would have macro cracks due to gas trapping or would shatter upon extraction due to hydrogen embrittlement [ref], as a result the in-flight

annealing temperature was increased, to lessen the amount of hydrogen remaining on the surface of the produced particles[ref].

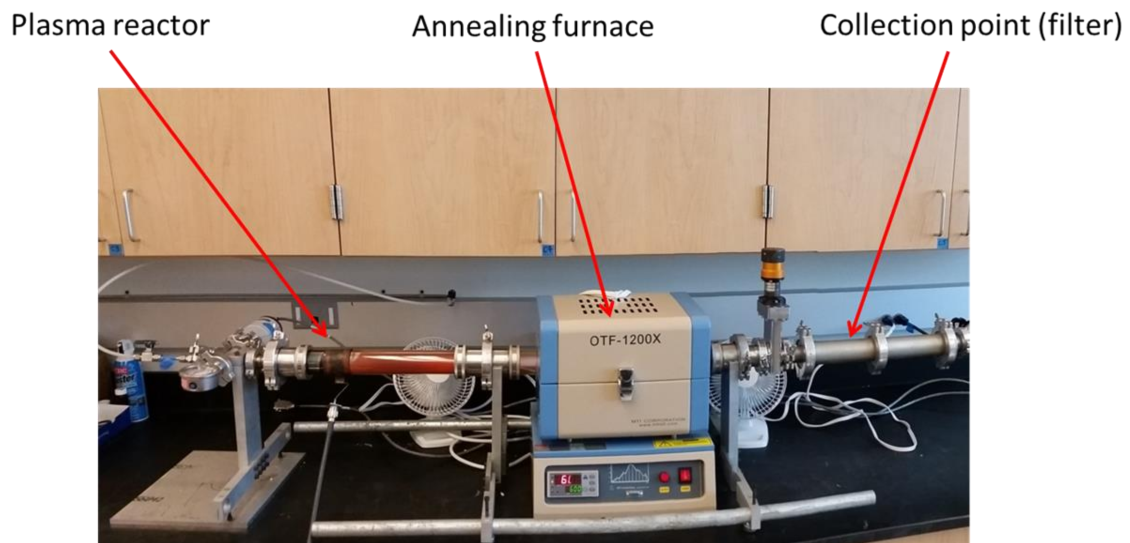

Figure 5.1 Scaled up plasma reactor capable of producing 100’s of milligrams an hour, plasma reactor control structure of particles from amorphous to crystalline, annealing furnace used to control hydrogen surface termination, collection point houses a stainless steel mesh filter between two gate valves allowing for transfer of particles under a controlled environment

In figure 5.2, the particle size distributions dependence on in-flight annealing temperature is shown. The particles produced on the first stage of the reactor are crystalline and hydrogen terminated, for the annealing temperatures used in this study we assume the silicon is near bare surface, SEE figure A.9 in appendix A. The minimization of surface hydrogen on the silicon nanoparticles, returned a densified sample that showed no macro indications of gas tapping or hydrogen embrittlement.

The third section of the reactor is comprised of a stainless steel chamber that holds a stainless steel mesh filter where the produced particles are collected. The filter can be sealed between two gate valves allowing the particles to be sealed in the collection chamber without risk of exposure to air. After particle collection is completed, the particles are transferred to a glove box where they are post-processed in an inert environment, in preparation for densification procedures.

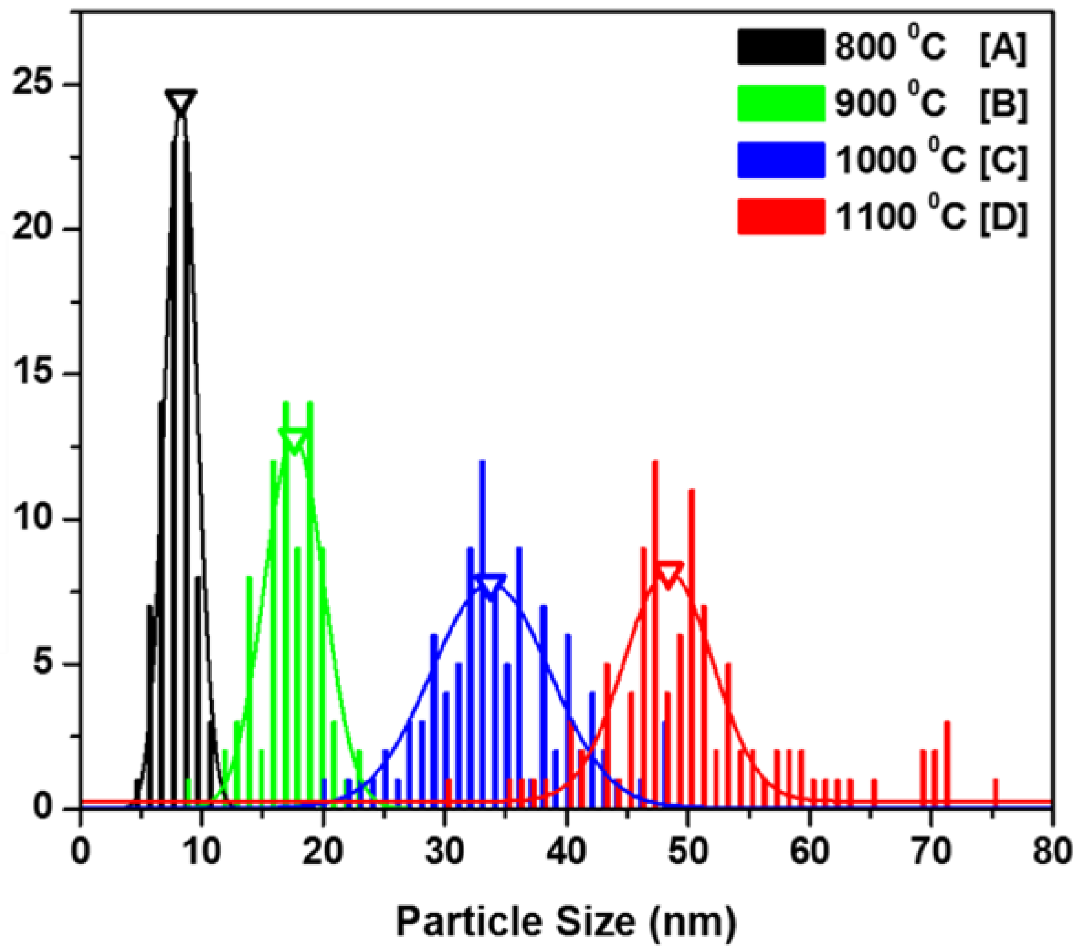

Figure 5.2 Particle size distribution as a function of in-flight annealing temperature. The corresponding lines are Gaussian peak fits with the center depicted by an open triangle.

5.3.2 Powder processing

Powder collected in the filter portion of the jumbo reactor is transferred to the glove box so processing can be done in a controlled environment. Powder transferred to the glove box is taken off of the stainless steel mesh and massed. A typical 2 hour run will produce close to 1000 mg of powder. Most samples made for pressing are 1500 mg. The silicon powder is doped at 2% with fine powder red phosphorous. The red phosphorous used in this system is prepared by placing 2 grams of chunk red phosphorous in a high energy ball mill with two 1.5 cm diameter stainless steel balls and ball milled for 30 minutes. The resulting powder has a uniform consistency and makes mixing with the as produced silicon powder easier.

There are two different methods that the dopant is added to the system, mortar and pestle, and low energy ball milling. For the mortar and pestle method the silicon powder is placed in the mortar first and then the corresponding correct amount of red phosphorus is placed on top. The samples are then vigorously mixed by hand for 30 minutes. The doped powder is then placed into a glass vial with a septa cover and placed in secondary containment until placed in the dye for densification.

For the low energy ball mill method, the silicon powder is massed and placed in a 130 ml glass jar, with 28 grams of 3 mm diameter alumina balls. Red phosphorus is then added to the jar at a 2% molar fraction of silicon. The glass jar is capped and a secondary seal around the bottom of the cover to the glass is made with electrical tape. The glass

jar is placed in 750 ml plastic jar that has a rubber O-ring seal, this allows for secondary containment of the silicon nanoparticles to minimize interaction with an oxygen environment. The plastic jar is taken out of the glove box and placed on a Thumbler's Tumbler rock tumbler, model number A-R1. The low energy ball milled samples are milled for 18 hours at ~100 rev/min. After low energy ball milling is completed the samples are brought back in to the glove box and the powder and alumina balls are separated. The powder is placed in a new glass jar and sealed until placed into a dye for densification.

5.3.3 Dye Preparation

Dyes utilized for the hot pressing densification procedures are made of graphite. The body of the dye is roughly 6” tall and 4” in diameter. A ½” hole is bored all the way through, with a cut out in the bottom where a graphite sleeve is placed, figure 5.3. The graphite sleeve is 3” long and houses the materials that will be densified. The sleeve and spacer pucks that will be in contact with the powder are coated with boron nitride. All graphite spacer pucks are polished and measured with a caliper to assure they are parallel and normal to the radial plane of the dye. Figure 5.3 shows a diagram of the prepared sleeve. The bottom puck is graphite only (A), the next is a piece of grafoil (B), a puck that has been prepared with boron nitride on the side exposed to particles is placed in the sleeve(C), The powder is then placed in the sleeve, followed by another puck that has been treated with boron nitride on the side that will be in contact with the powder(D). Another piece of grafoil is placed above that (E) followed by another spacer puck (F). The sample is cold pressed 1 ton prior to being placed in a hot press. This sleeve assembly is set into the larger dye which is then placed into the hot press. A long plunger is placed above the last puck, long enough to ensure there will be no interference with the press, so the ram will not bottom out during the densification procedure.

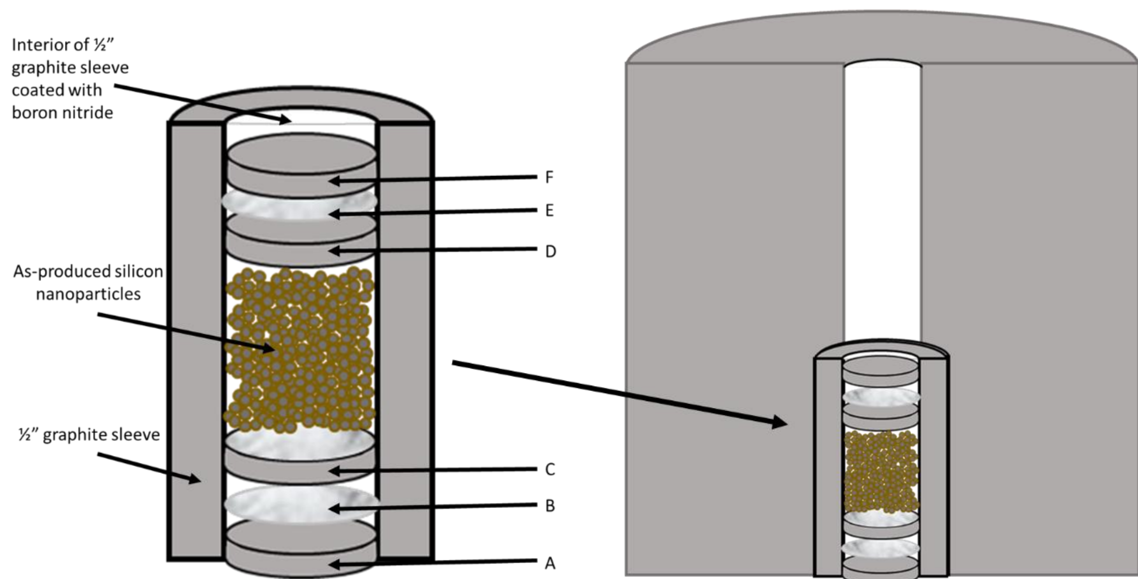

Figure 5.3 Hot press dye and sleeve schematic (A-bottom, F-top) blank graphite spacer, (B, E) grafoil sheet, (C, D) Graphite spacer with one side (facing the silicon particles) coated with boron nitride

Table 5.1 shows the inflight annealing temperatures for the CFNTPR produced powders and their respective pressing parameters. All samples in this study were pressed at 1160 ^{0}C and a pressure 105 MPa. Extracted samples are ~1.25 cm in diameter and are 4-5 mm thick. The samples are cut with a diamond abrasive saw to make them radially parallel. The cut pieces are polished on both sides maintaining parallel. For the data reported here the samples are polished to a 400 grit smooth surface and are on average 1 mm thick for analysis procedures: hall-effect, thermal conductivity, and Seebeck measurements. Before each high temperature measurement the samples are brought up to 1000 ^{0}C for 30 minutes and then quenched in air, resetting the phosphorous dopant in the silicon sample[27].

Table 5.1: In-flight and hot press conditions of CFNTPR produced silicon nanoparticles

Sample Name	Particle In-flight Processes		Hot Press	
	Plasma Power (watts)	Annealing Temperature (^0C)	Temperature (^0C)	Ram Pressure (MPa)
A	160	800	1160	105
B	160	900	1160	105
C	160	1000	1160	105
D	160	1100	1160	105

5.4 Results and discussion

5.4.1 Doping

The doping levels of the produced samples was tracked using two different measurement methods, hall-effect and Seebeck. Figure 5.4 shows the results of the of the high temperature hall-effect measurement, in the form of electrical resistivity. The electrical resistivity of samples D and B seem to be the best of the four, as shown in a plot of room temperature mobility versus carrier concentration in figure 5.5. The electrical resistivity data for Sample D is in good agreement with the room temperature mobility versus carrier concentration data, figure 5.4 and figure 5.5 respectively. The plot shows sample D having a near perfect doping level, with a mobility of 30 $cm^2 V^{-1} s^{-1}$ and a carrier concentration of 5.0 x 10^{20} cm^{-3}. Sample C is the next best sample for electrical resistivity and with a correlating room temperature carrier concentration and mobility values of 25 $cm^2 V^{-1} s^{-1}$ and 5.9 x 10^{20} cm^{-3} respectively. Samples D, C, and B room temperature carrier concentration and mobility values all fall between single crystal silicon doped at a 2% molar fraction and a 30% mobility degradation level. Sample A on the other hand falls below the 30% mobility degradation line and has a higher electrical resistivity than the other three samples, figure 5.4.

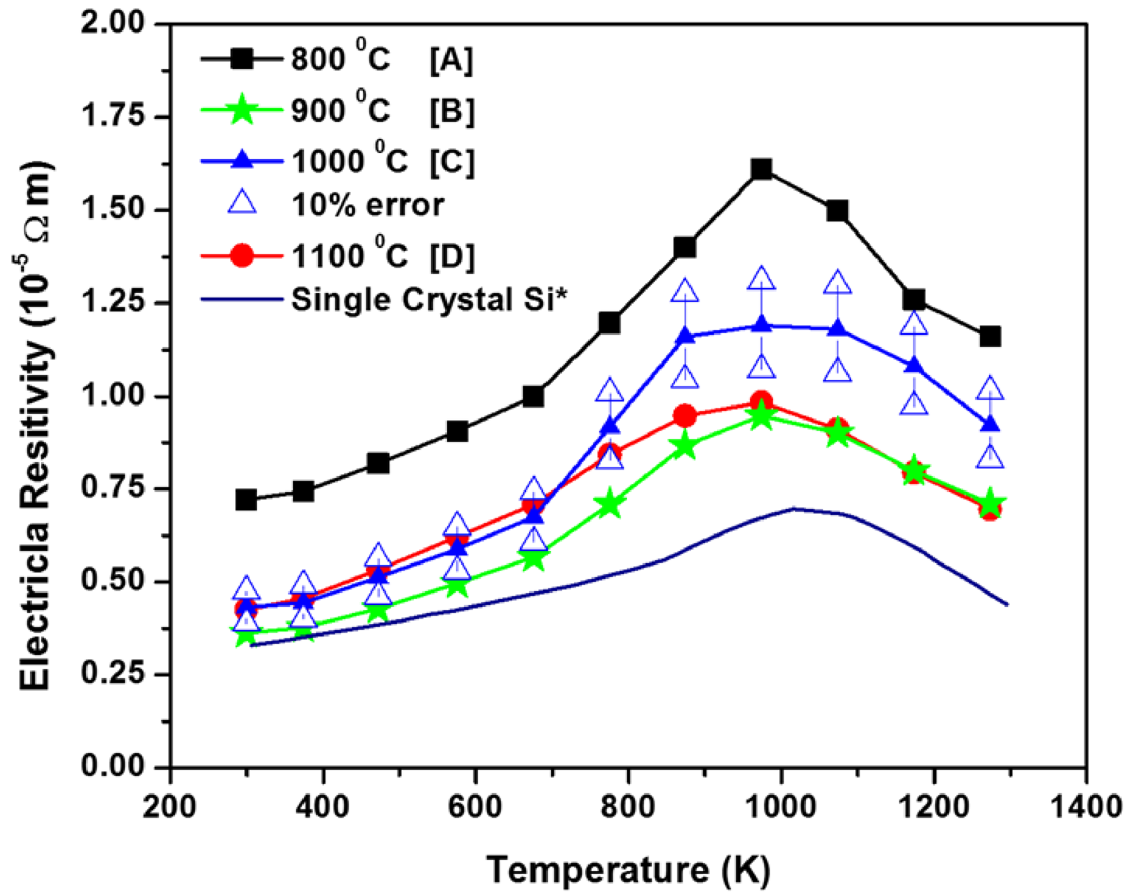

Figure 5.4 Electrical resistivity as a function of temperature, with samples A-D and a calculated reference for single crystal silicon

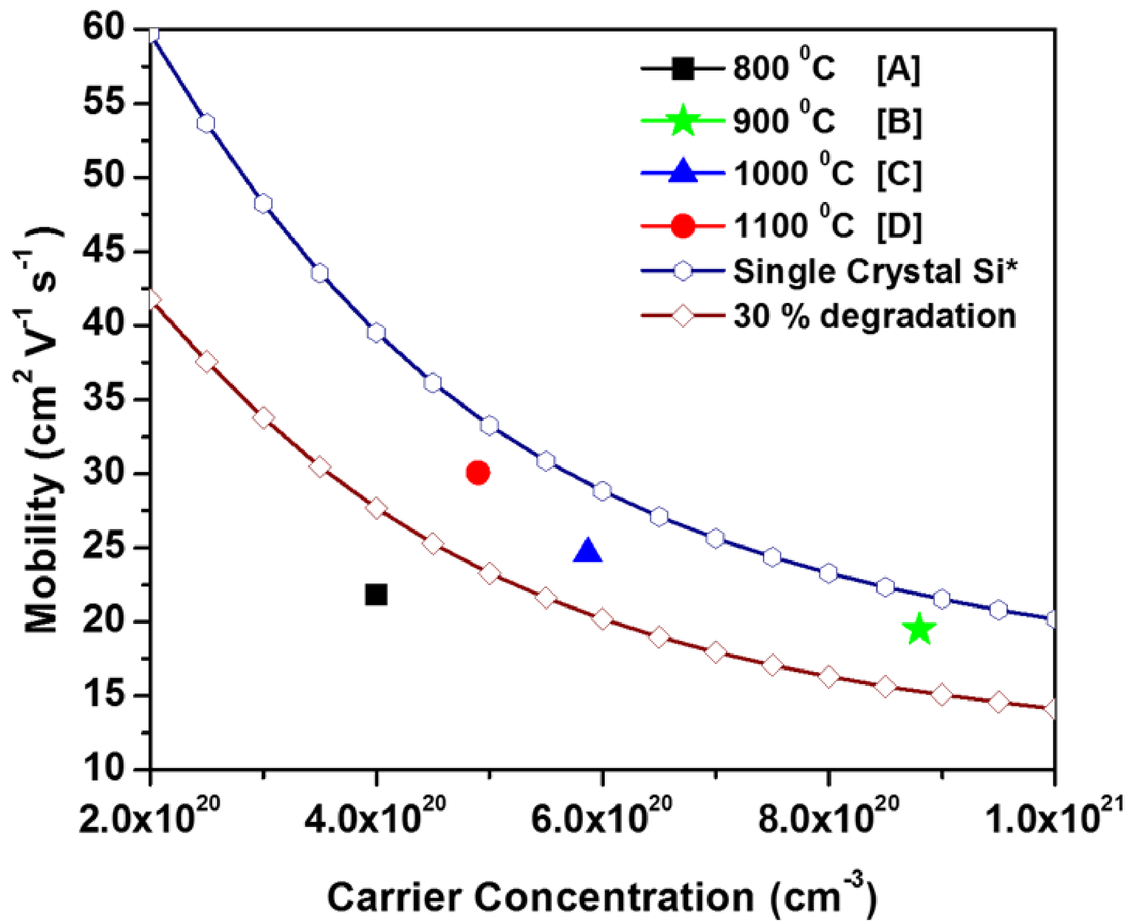

Figure 5.5 Room temperature mobility versus carrier concentration

Figure 5.6 Shows Seebeck coefficient versus temperature. The highest absolute value for the Seebeck coefficient of the group is sample A, this is due to the fact that absolute value of the Seebeck coefficient will increase if doping levels are lowered, i.e. mobility degradation as seen in Sample A. If the mobility of electrons in the system is lowered there exists the ability to create charge build up, in this case n-type, on the cold side of the sample. The charge build up creates a greater delta V while the change in temperature across the sample stays at a relatively low value. This in-turn increases the overall absolute value of the measured Seebeck coefficient. Although this is a good thing for the ZT value of the system, there is a loss to the electrical resistivity, as it is pushed to a higher value, figure 5.4. Sample D again shows the best result, it is important to note that sample B and C are also within the error of values for sample D, until they reach ~900 K. This again is due to the correct doping level of the sample, at ~900 K phosphorous will begin to move back into the silicon matrix[16] and mobility will increase allowing for a decrease in electrical resistivity and Seebeck coefficient values[17], as shown in figures 5.4 And 5.6, respectively.

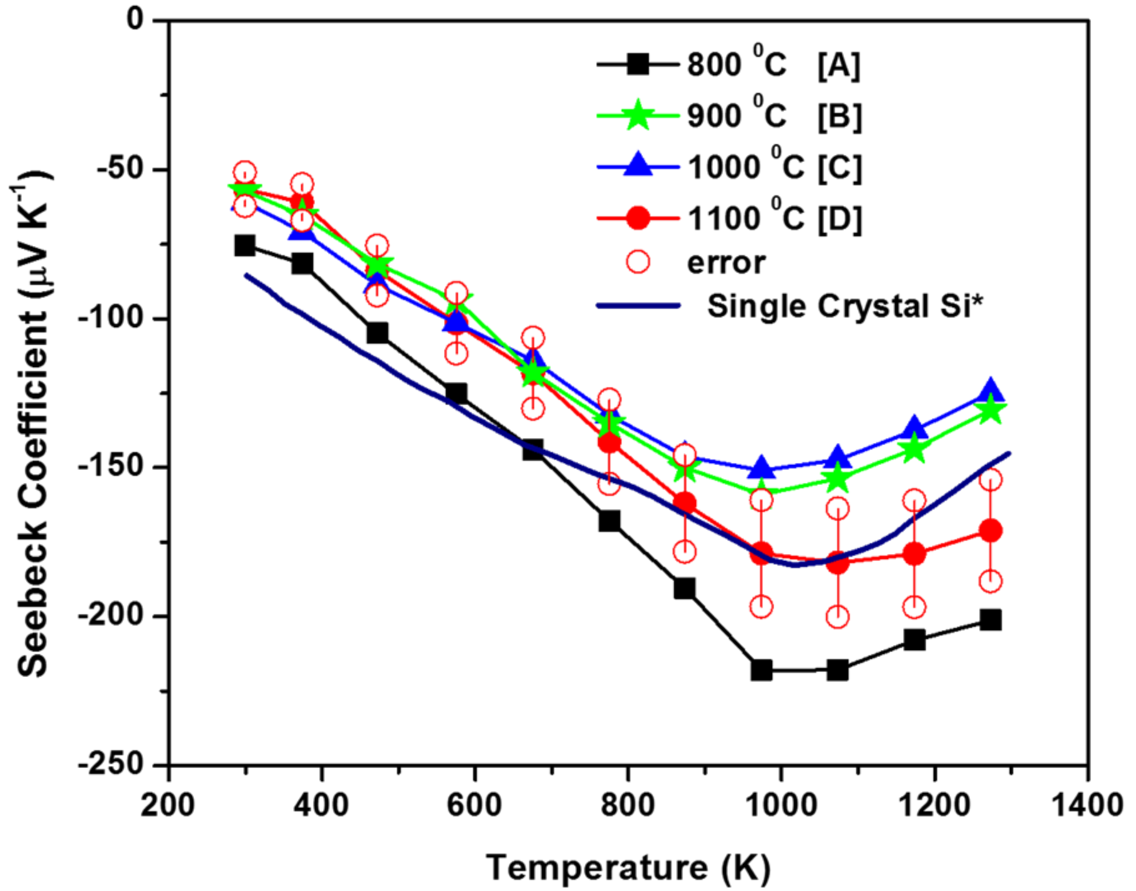

Figure 5.6 Seebeck measurement as a function of temperature for samples A-D and a reference line of single crystal silicon

5.4.2 Thermal Conductivity

Thermal conductivity measurements were made using a laser flash system. Samples are brought to a specified temperature at which a laser flash is used to heat one side of the sample. The measurement made is the time it takes for the colder side of the sample to reach half of the maximum temperature[18]. From this a value for diffusivity is made, see equation 5.1. The diffusivity measurement is then multiplied by density and heat capacity to get thermal conductivity[16].

Equation 5.1

$$\alpha = 0.1388 * \frac{d^2}{t_{1/2}},$$

where α is thermal diffusivity, d is the distance from one side of the sample to the other in the same direction of the laser flash, i.e. the direction in which the heat will flow, $t_{1/2}$ is the time it takes for the the cold side of the sample to reach half of the maximum temperature. Figure 5.7 shows the results of the full thermal conductivity of the measured samples. As shown by the error bars in figure 5.6, which is a 10% instrument error, samples A-D fall within the same relative range for thermal conductivity. Samples A-D are also in the same thermal conductivity range as some the best to date samples of nanostructured bulk silicon produced for thermoelectric applications. The diamond data points refer to a p-type silicon sample produced by Petermann et al.[19] and the pentagon data points refer to a n-type sample produced by Bux et al.[6].

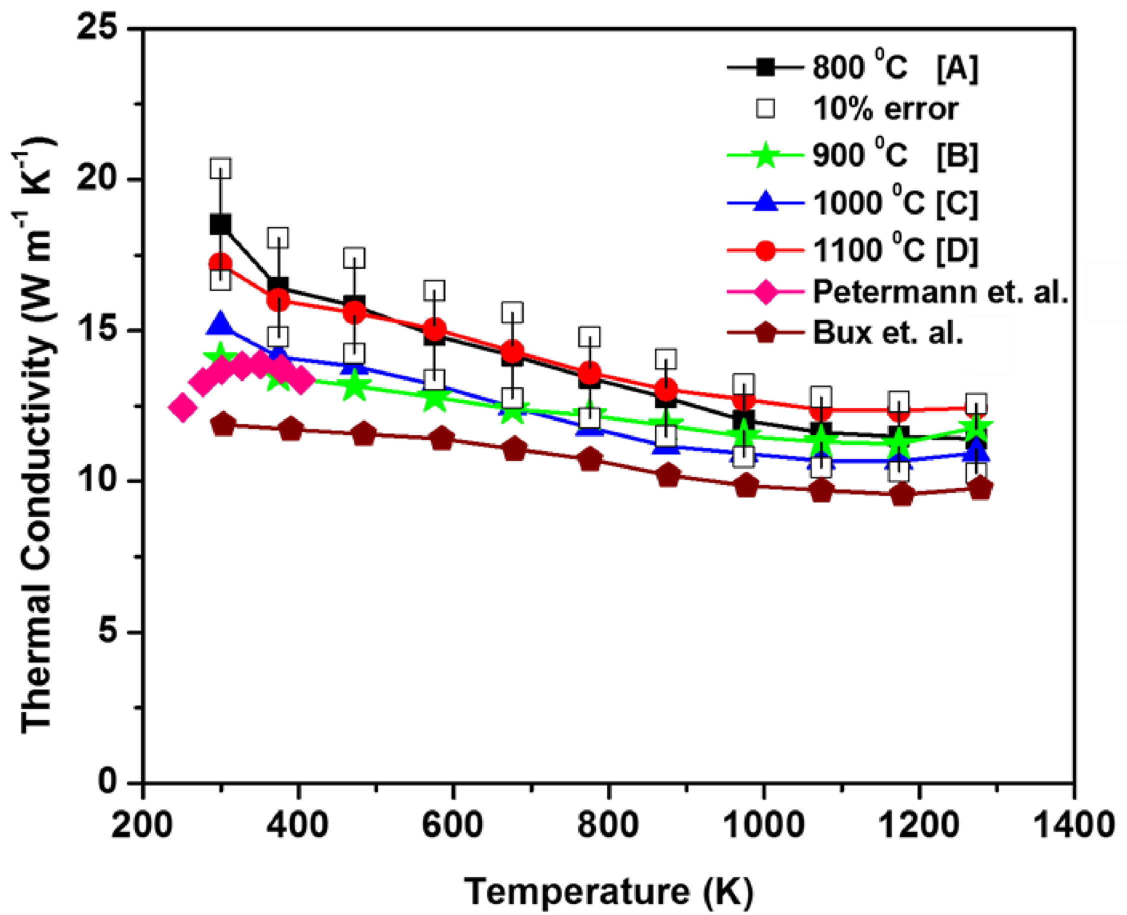

Figure 5.7 Thermal conductivity as a function of temperature for samples A-D, Petermann [19], and Bux [6]

Figure 5.8 shows lattice thermal conductivity as a function of temperature. This value is calculated from the full thermal conductivity measurement using the Weidman-Franc law and Lorenz law[20]. The lattice thermal conductivity is a way to remove electron as a heat carrier form the thermal conductivity measurement. This allows lattice thermal conductivity to give insight into what influences the structure has on the thermal transport. The CFNTPR samples a value for lattice thermal conductivity that is close to a 70% reduction of that observed in a single crystal silicon system. This reduction is assumed to be due to the structure of the CFNTPR produced sample system.

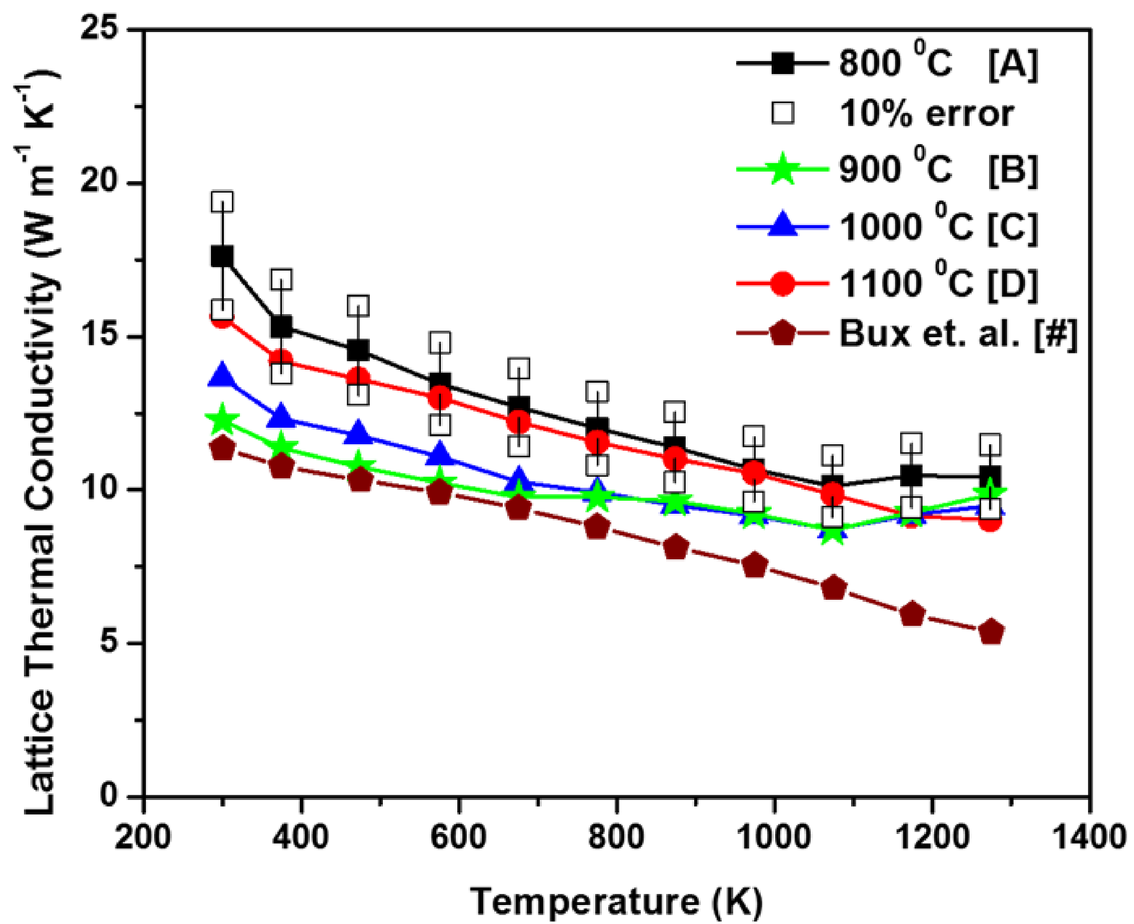

Figure 5.8 Lattice thermal conductivity as a function of temperature for samples A-D and Bux [6]

5.4.3 Figure of merit (ZT)

Figure 5.9 shows the ZT values for samples A-D, produced by a combination of CFNTPR produced powders and hot pressing. Of the CFNTPR samples, D shows the best ZT value, 0.43. Other values shown in figure 5.9: Bux[6] samples; nano-structured at 0.47 and 0.68 both at 1300 K, Petermann[19] 0.15 at 700 K. A value not included in figure 5.9 from a recent publication from the same group of Petermann, Kessler et al[22]. shows a ZT value of 0.32 at 1000. As these two groups are the at the cutting edge of silicon thermoelectric research, the initial ZT value reached with samples A and D are promising for future research in nanostructured bulk silicon systems for thermoelectric applications.

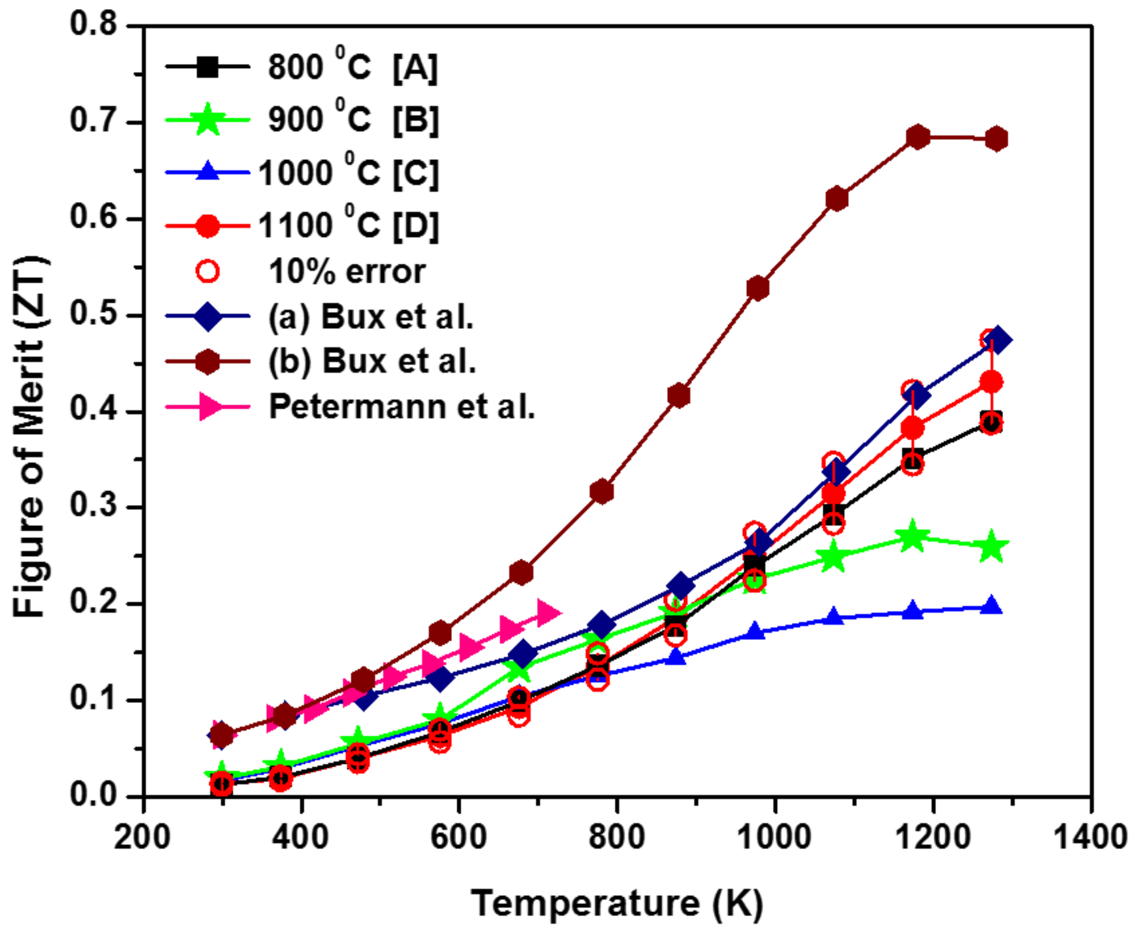

Figure 5.9 Figure of merit (ZT) as a function of temperature for samples A-D, Bux (a) and (b)[6], and Petermann[19]

5.5 Preliminary structural results

Preliminary structural data shows many important and interesting results. First, XRD taken of the bulk samples returns values ranging from 64-93 nm for each of the samples depending on the temperature of the initial in-flight annealing temperature, Figure 5.10C. TEM images in figure 5.10A, show a variety of crystallite sizes ranging from 25-55 nm, which doesn't correspond to the grain size observed by SEM, which is on the order of 100's of nm, figure 5.10B. As we are trying to improve phonon scattering within this system by structure, more structural characterization needs to be done in order to fully understand phonon scattering mechanisms in bulk nanostructured material systems.

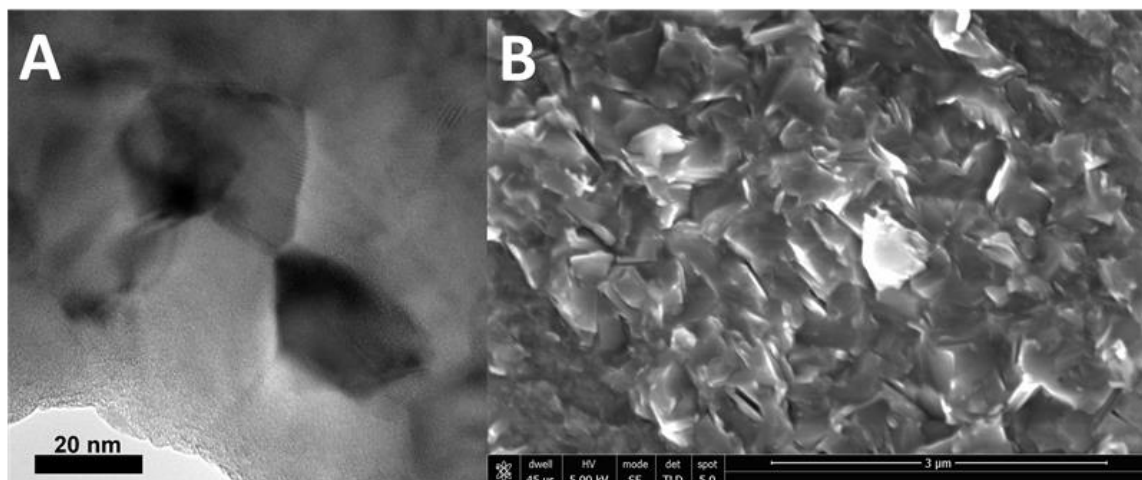

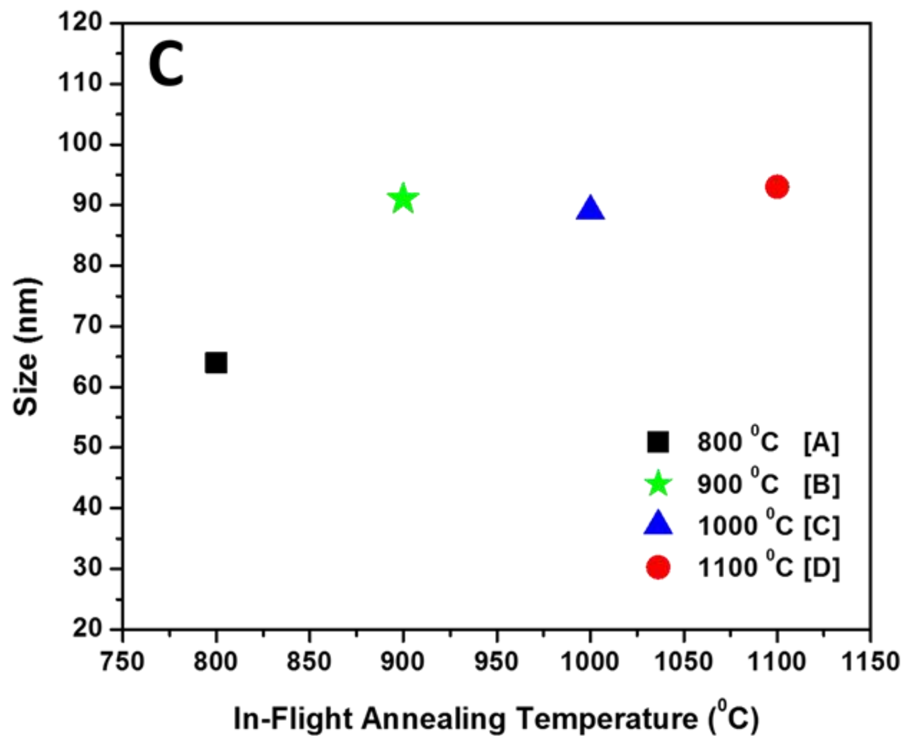

Figure 5.10 (A) bright field TEM image showing crystallites ranging in size from 25-55 nm, (B) SEM image showing intergranular crack propagation with grains in the 100's of nm size range, (C) Scherrer first peak analysis from XRD data showing an estimated crystallite size as a function of in-flight annealing temperature.

5.6 Conclusion

The ability to produce nanocrystals with narrow size distributions, with control over size, structure, and surface termination, allows for the broadening of the parameters used to engineer bulk nanostructured material systems. The success using CFNTPR produced nano-silicon for hot press densification processes has turned out to be very successful. Preliminary ZT measurements are encouraging and show this powder synthesis method and densification process have the ability to be competitive within the thermoelectric research field. As silicon is an established and well characterized material system makes it a great test material that can be applied to other bulk nanostructured materials. Furthermore, non-thermal plasmas allow for the scalable synthesis of a broad range of nanopowders with excellent control over size, structure, and surface chemistry. The ability to take advantage of these systems will advance the understanding of bulk nanostructured materials.

5.7 References

1. L. Mangolini, Journal of Vacuum Science & Technology B: Microelectronics and Nanometer Structures, 2013, 31, 020801)
2. C.-Y. Liu, Z. C. Holman and U. R. Kortshagen, Nano letters, 2009, 9, 449-452
3. K.-S. Cho, et al., Shin, Applied Physics Letters, 2005, 86, 071909
4. K.-Y. Cheng, et al., Nano Letters, 2011, 11, 1952-1956.
5. Garay, J. E. Annual review of materials research 40 (2010): 445-468.
6. Bux, Sabah K., et al. Advanced Functional Materials 19.15 (2009): 2445-2452
7. T. Seto, Y. Kawakami, N. Suzuki, M. Hirasawa and N. Aya, Nano Letters, 2001, 1, 315-318.
8. M. L. Ostraat, et al., J. Electrochem. Soc., 2001, 148, G265-G270
9. X. Li, Y. He, S. S. Talukdar and M. T. Swihart, Langmuir, 2003, 19, 8490-8496.
10. O. Yasar-Inceoglu, et al., Nanotechnology 23, 255604 (2012)
11. Lopez, T., et al. Nanoscale, 2014. 6.3 p.1286-1294
12. Lopez, Thomas, et. al. Journal of Vacuum Science & Technology B 32.6 (2014): 061802.
13. L. Mangolini, E. Thimsen, and U. Kortshagen, Nano Lett. 5, 655 (2005).
14. Yi, Tanghong, et al. Journal of Materials Chemistry 22.47 (2012): 24805-24813.
15. Bux, Sabah K., et al Chemistry of Materials 22.8 (2010): 2534-2540.
16. Slack, Glen A., and D. M. Rowe. "CRC handbook of thermoelectrics." *CRC, Boca Raton, FL* 407440 (1995).

17. Masetti, G., and S. Solmi. "Relationship between carrier mobility and electron concentration in silicon heavily doped with phosphorus." *IEE Journal on Solid-State and Electron Devices* 3.3 (1979): 65-68.

18. Parker, W. J., et al. "Flash method of determining thermal diffusivity, heat capacity, and thermal conductivity." *Journal of applied physics* 32.9 (1961): 1679-1684.

19. Petermann, Nils, et al. "Plasma synthesis of nanostructures for improved thermoelectric properties." *Journal of Physics D: Applied Physics* 44.17 (2011): 174034.

20. Kumar, G. S., G. Prasad, and R. O. Pohl. "Experimental determinations of the Lorenz number." *Journal of materials science* 28.16 (1993): 4261-4272.Bux Adv Mat

21. Kessler, Victor, et al. "Thermoelectric Properties of Nanocrystalline Silicon from a Scaled-Up Synthesis Plant." *Advanced engineering materials* 15.5 (2013): 379-385.

22. Patterson, A. L. "The Scherrer formula for X-ray particle size determination."*Physical review* 56.10 (1939): 978.Sherrer average

Chapter 6

Conclusion and future works

6.1 Conclusions

6.1.1 Continuous flow nonthermal plasma reactors

Continuous flow nonthermal plasmas have very unique properties that allow for the production of very high quality nanoparticles. It has been experimentally determined that the rate of crystallization of amorphous silicon nano particles is a thermally driven process and is size dependent. For particles 7 nm the activation energy is 1 eV, which is half of that found for activation energy of silicon thin films, and is completed at ~1100K and a residence time of 100 milliseconds.

In-situ IR measurements of continuous flow nonthermal plasma reactors, along with the characterization of extracted particles has shed light on to the evolution of precursor gas consumption all the way to structural evolution. All of which occur in less than 130 milliseconds. Comparing the time it takes for crystallization to take place and under the assumption that the phase transformation is due to the heating induced by the recombination of plasma-produced species at the particle surface, an estimated the particle temperature in the plasma was found to be ~1160K.

In-situ, in-flight FTIR used to monitor the surface of silicon nanoparticles immersed in a partially ionized gas, experimentally verified, that a thermal effect leads to rapid desorption of hydrogen from the particle surface. This observation was used to estimate the temperature of nanoparticles as a function of plasma input power. While there is variation depending on the assumed electron temperature value, a consistent estimate of the nanoparticle temperature is in the 650K-750K range, with a linear increase in temperature with RF input power. This provides additional confirmation that non-thermal plasmas as a nanopowder synthesis and processing tool remains to be fully understood.

6.1.2 Nanostructured bulk silicon systems

The ability to produce nanocrystals with control over size, structure, and surface termination, allows for the broadening of the parameters used to engineer bulk nanostructured material systems. The success using CFNTPR produced nano silicon for hot press densification processes has turned out to be very successful. Preliminary ZT measurements are encouraging and show this powder synthesis method and densification process has the ability to be competitive within the thermoelectric research field.

6.2 Future works

6.2.1 Continuous flow nonthermal plasma reactors

A further look into what the dominant species in the plasma is responsible for particle heating needs to done. The question is if the same study was carried out using silicon tetra-chloride ($SiCl_4$), with no addition of hydrogen would an analogous heating of the particle occur? Also if hydrogen were added to the system would it lower the input power needed to heat the $SiCl_4$ produced particles? A similar system as the one presented in chapter 4 would need to be utilized. As a measurement of ion density, and elemental chlorine and hydrogen would need to be taken into account to solve for the temperature the particles could achieve.

6.2.2 Nanostructured bulk silicon systems

Chapter 5 summarized an ongoing study of nanostructured bulk silicon systems and their thermoelectric application. Currently, Samples A-D are beginning a long reset procedure. The samples are placed in an ampule under vacuum and then placed in a tube furnace at 1000 ^{0}C for one week. This has been shown to redistribute the dopant, phosphorous, throughout the system allowing for a more homogenous doping of the sample without inducing any microstructure changes. After which the samples will go through the same thermal and electrical characterization as before. By comparing the electrical and thermal conductivity measurement before and after the long reset will show whether or not non-homogenous doping was an issue.

The ability to control microstructure within bulk systems is currently being looked into. Four new bulk samples were made all using the same in-flight annealing temperature of 800 ^{0}C, so the smallest initial particle size range, 6-11 nm, was used. A temperature swipe of the maximum temperature at which the particles were densified at was used 1010 ^{0}C, 1110 ^{0}C, and 1160 ^{0}C. Initial XRD analysis shows that there exists structural dependence on densification temperature, figure 6.1. More structural characterization needs to be done on all samples to verify the dependence of observed transport phenomenon to the nanostructured bulk system.

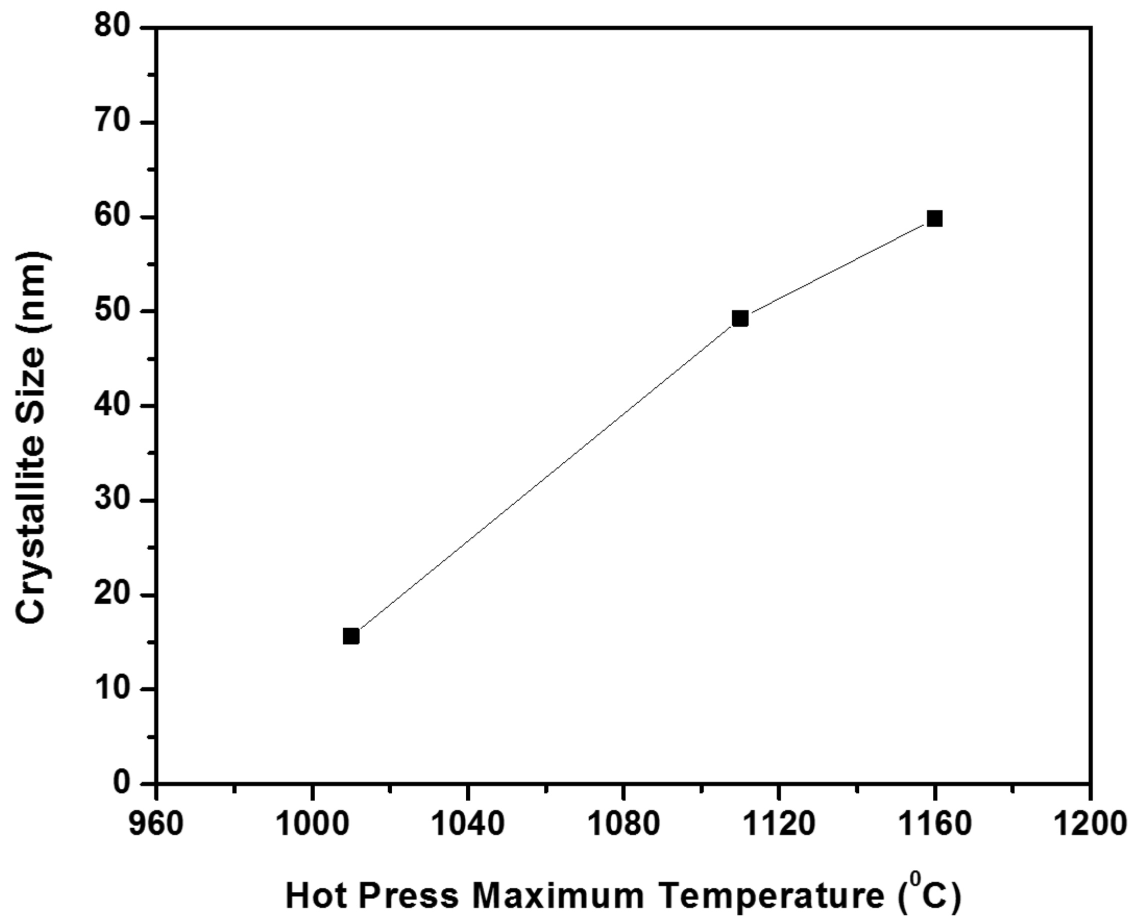

Figure 6.1 Microstructure dependence on hot press maximum temperature

Appendix A

A.1. Supplemental Figures for Chapter 1

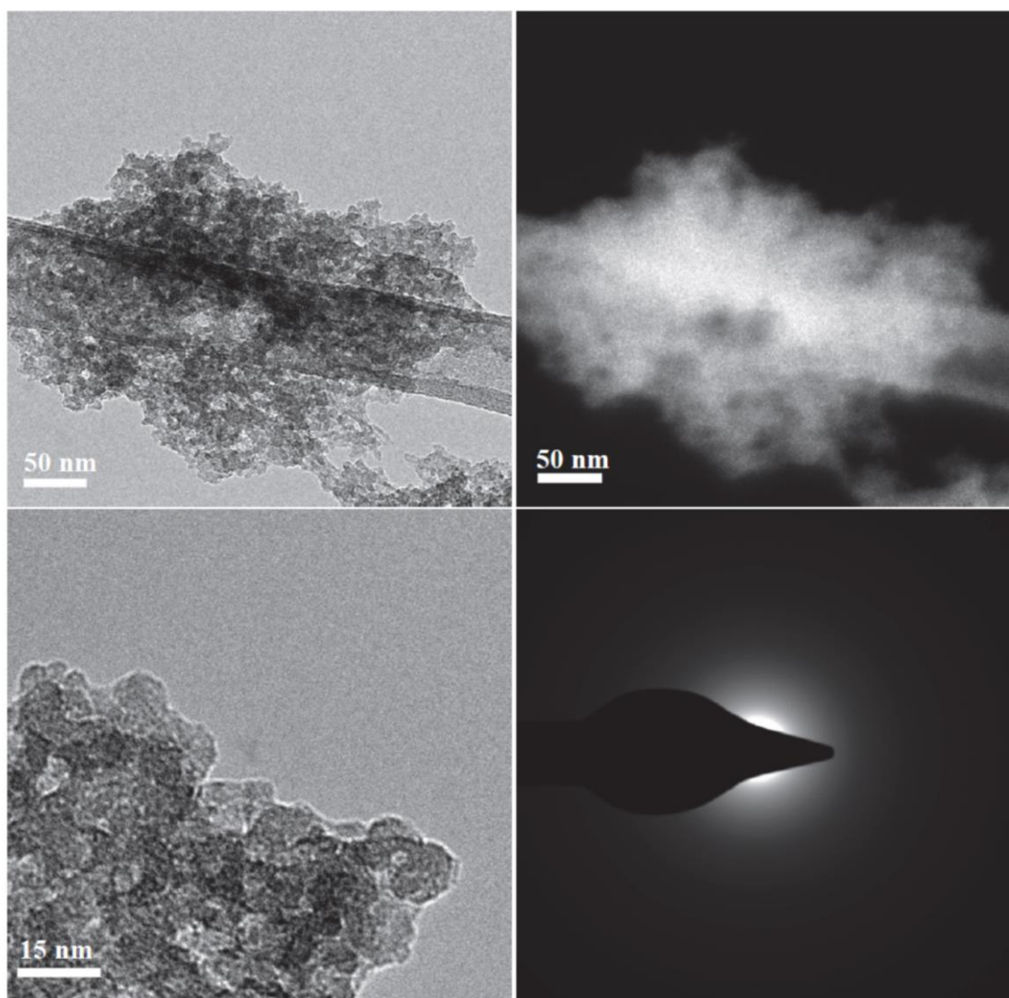

Figure A.1. (a) TEM micrograph of amorphous silicon particles produced under the conditions of 'sample A' (see Table 2.1) without any in-flight annealing. (b) Dark field micrograph of figure (a). (c) higher magnification micrograph for the sample, and (d) corresponding selected area diffraction (SAD) pattern. A lower magnification image was used to generate the diffraction pattern, so that a large number of particles interact with the electron beam. The combination of weak contrast in the dark field image, lack of fringes in the higher magnification image, and weak pattern in the SAD leads to conclude that the particle have an amorphous structure.

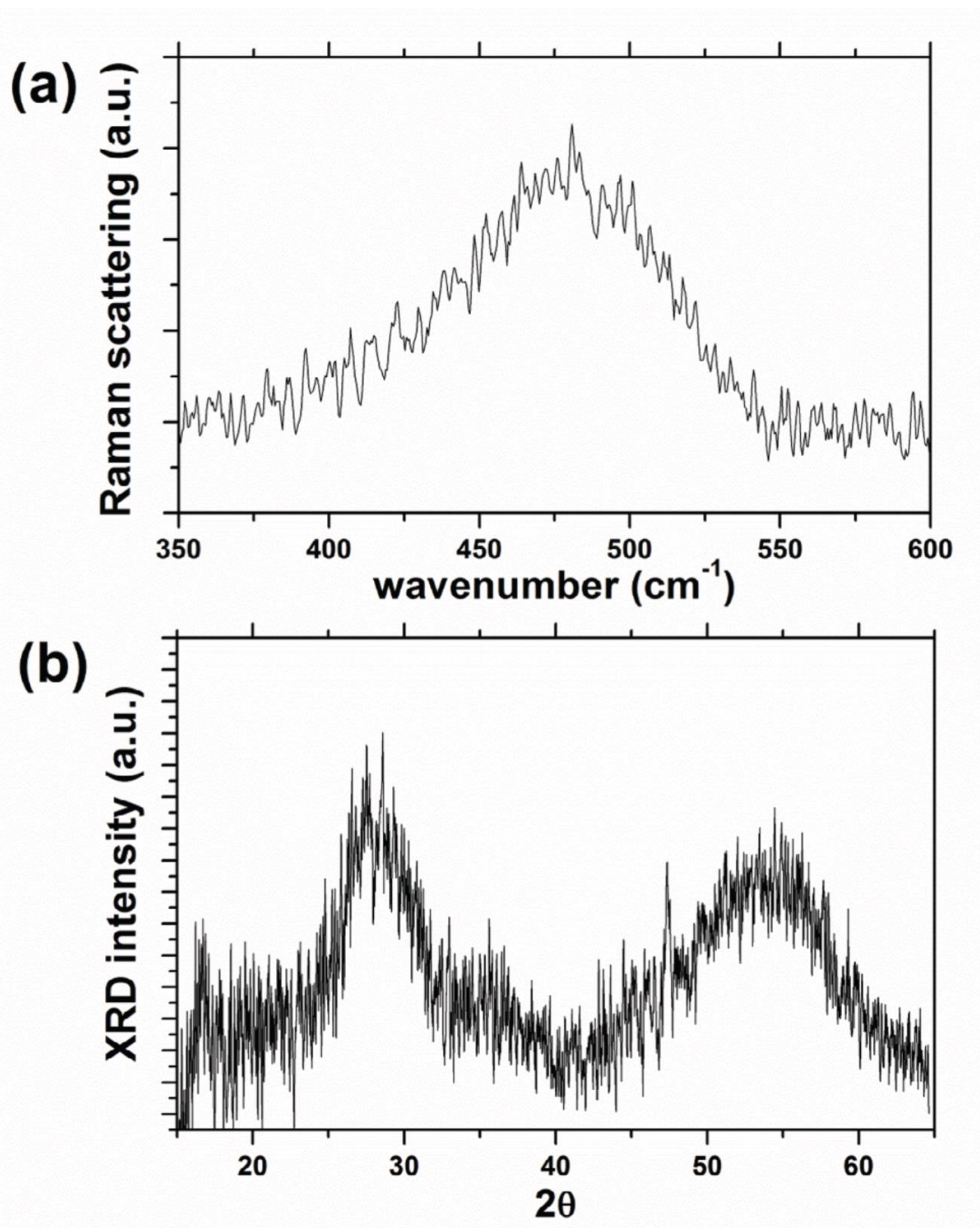

Figure A.2. (a) Raman scattering from samples produced under the conditions of 'sample A' (see table 2.1) without any in-flight annealing. (b) XRD for the same sample of (a). Both Raman and XRD data support the conclusion that the particles have an amorphous structure.

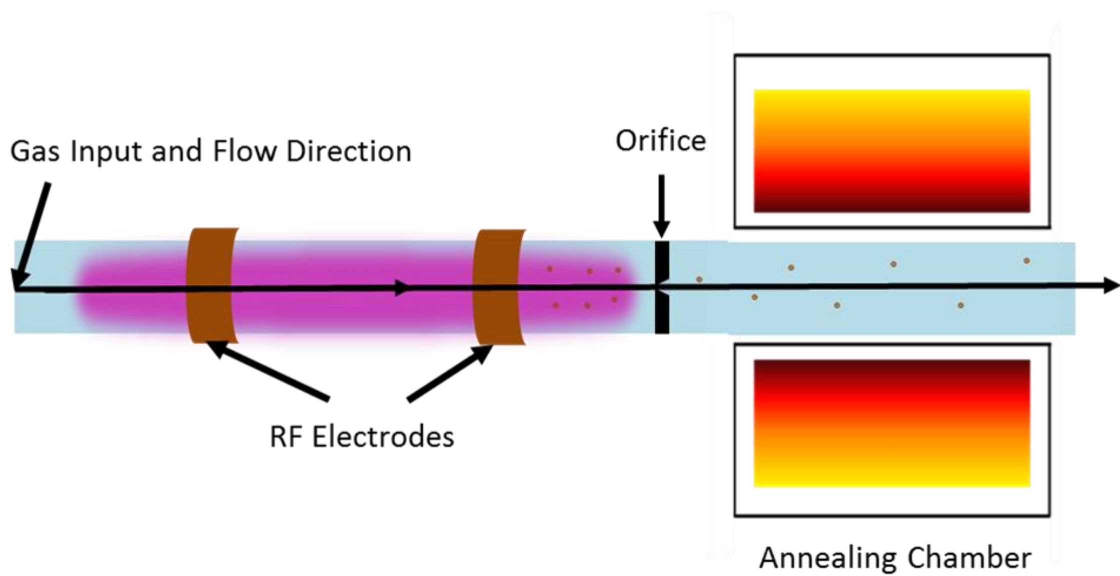

Figure A.3. Schematic of two phase reactor production parameters for the samples produced in this reactor are summarized in Table 2.1. (a) first stage allows for control of size and structure of produced particles (b) second stage annealing chamber with independently controlled temperature and annealing time.

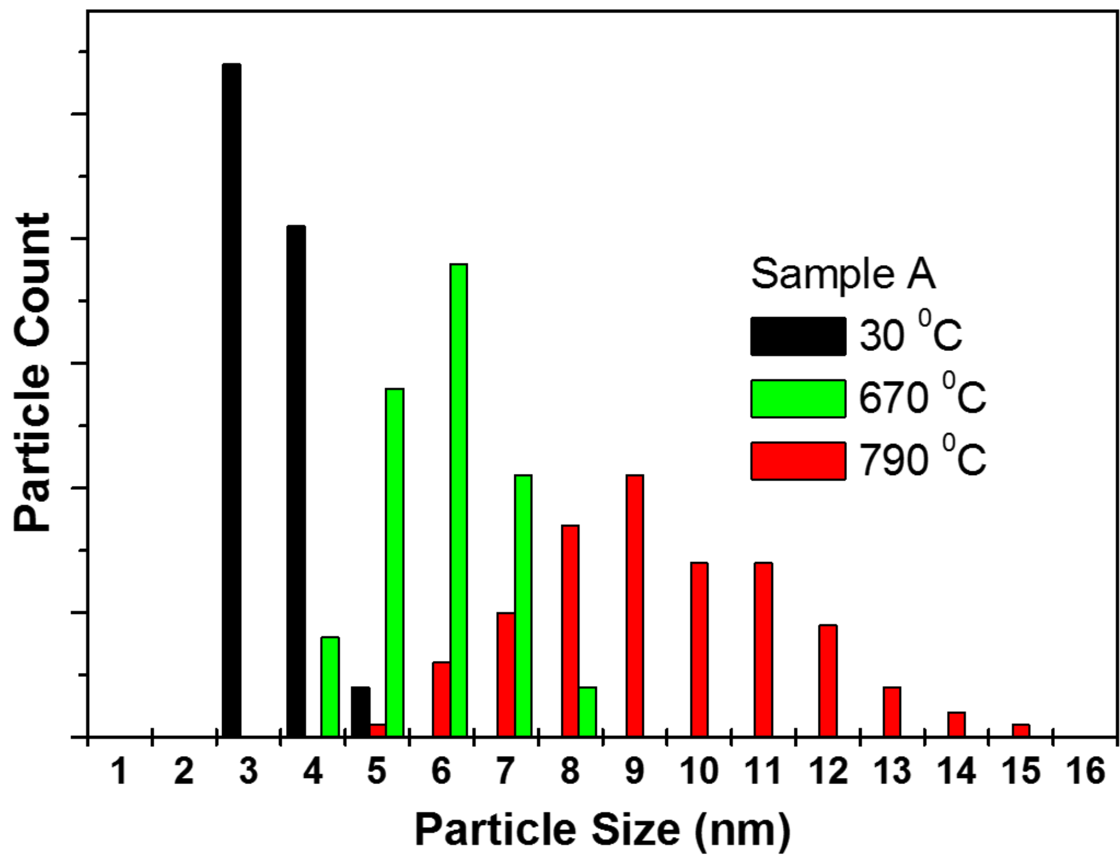

Figure A.4 Particle size distribution of Sample A at three different in-flight annealing temperatures.

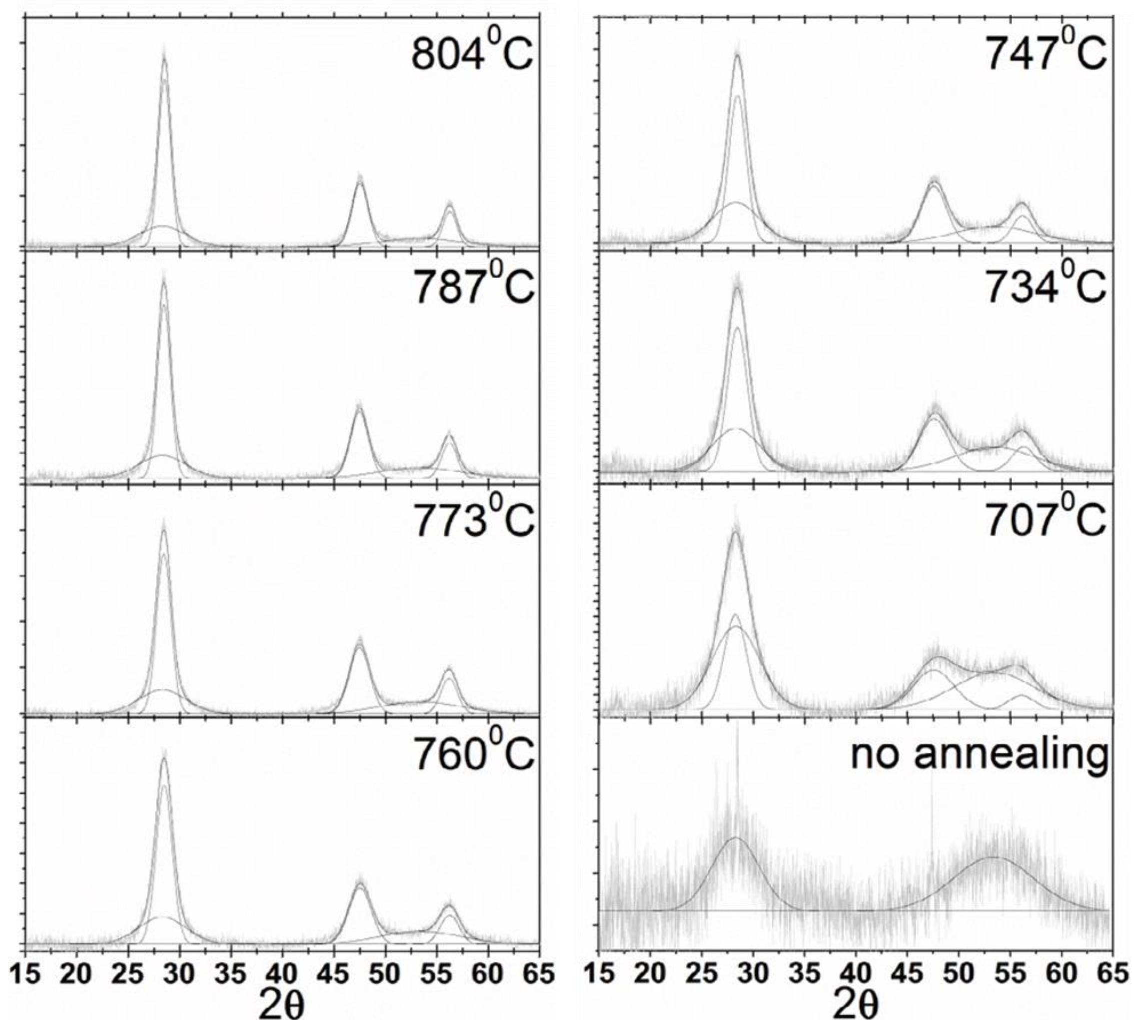

Figure A.5. Fitting of XRD data for the determination of the crystalline fraction. A five peaks procedure is used, with the center and width of the two peaks due to the amorphous phase determined using the XRD data for the sample that has not been annealed (see graph labeled as 'no annealing'). The five peaks fit is then performed by holding constant the position and width for the two peaks corresponding to the amorphous contribution, while fitting their amplitude together with that of the peaks arising from the crystalline structure. The crystalline fraction is quantified by calculating the ratio between the area under the three sharper peaks due to the crystalline structure (from the [111], [220] and [311] lattice planes) over the total area (area from the crystalline peaks summed with the area from the two amorphous features). The in-flight annealing temperatures are clearly labeled on the graphs.

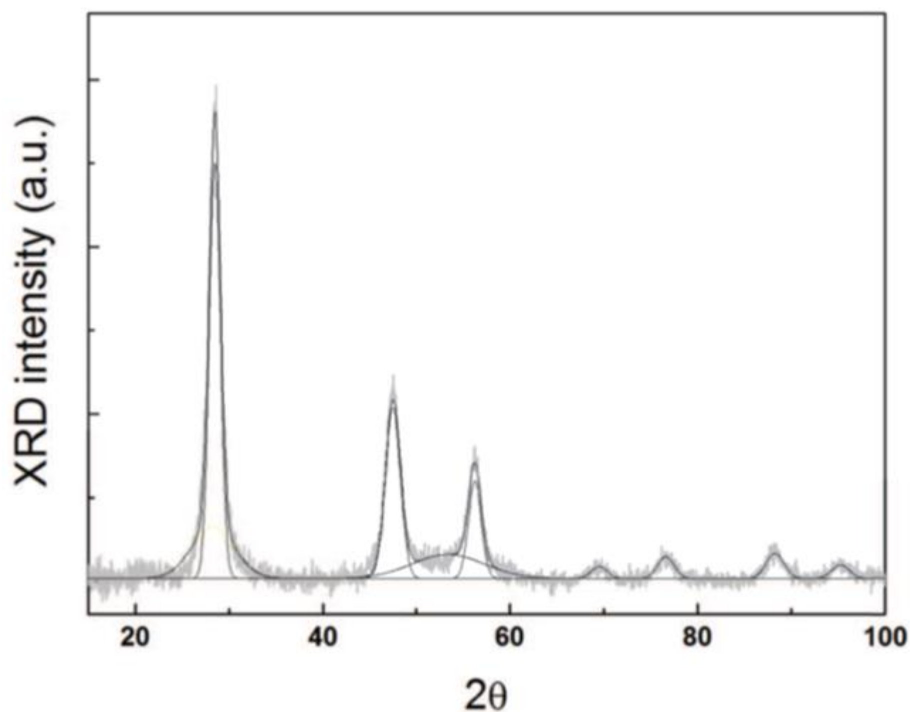

plane	2θ	FWHM
[111]	28.47895	1.4415
[220]	47.48861	1.90036
[311]	56.22458	1.64053
[400]	69.48807	2.01858
[331]	76.58974	2.06393
[442]	88.26317	2.22249
[511]	95.23489	2.17635

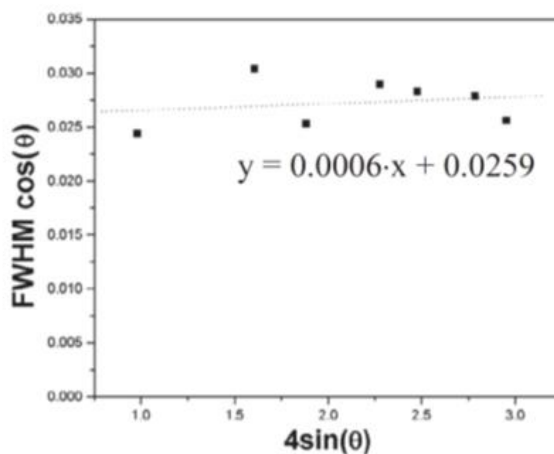

Figure A.6. (top) XRD data for sample produced and annealed under the condition of 'Sample A' (see Table 2.1), annealed at 800^{0}C. The curve fitted using Guassian profiles for each crystalline peak and for the peaks due to amorphous contribution. (bottom left) table with the crystalline peak position and their relative full width- half max (FWHM). (bottom right) Williamson- Hall Plot: a linear fit of the data has negligible slope (proportional to streee acting on the crystal).

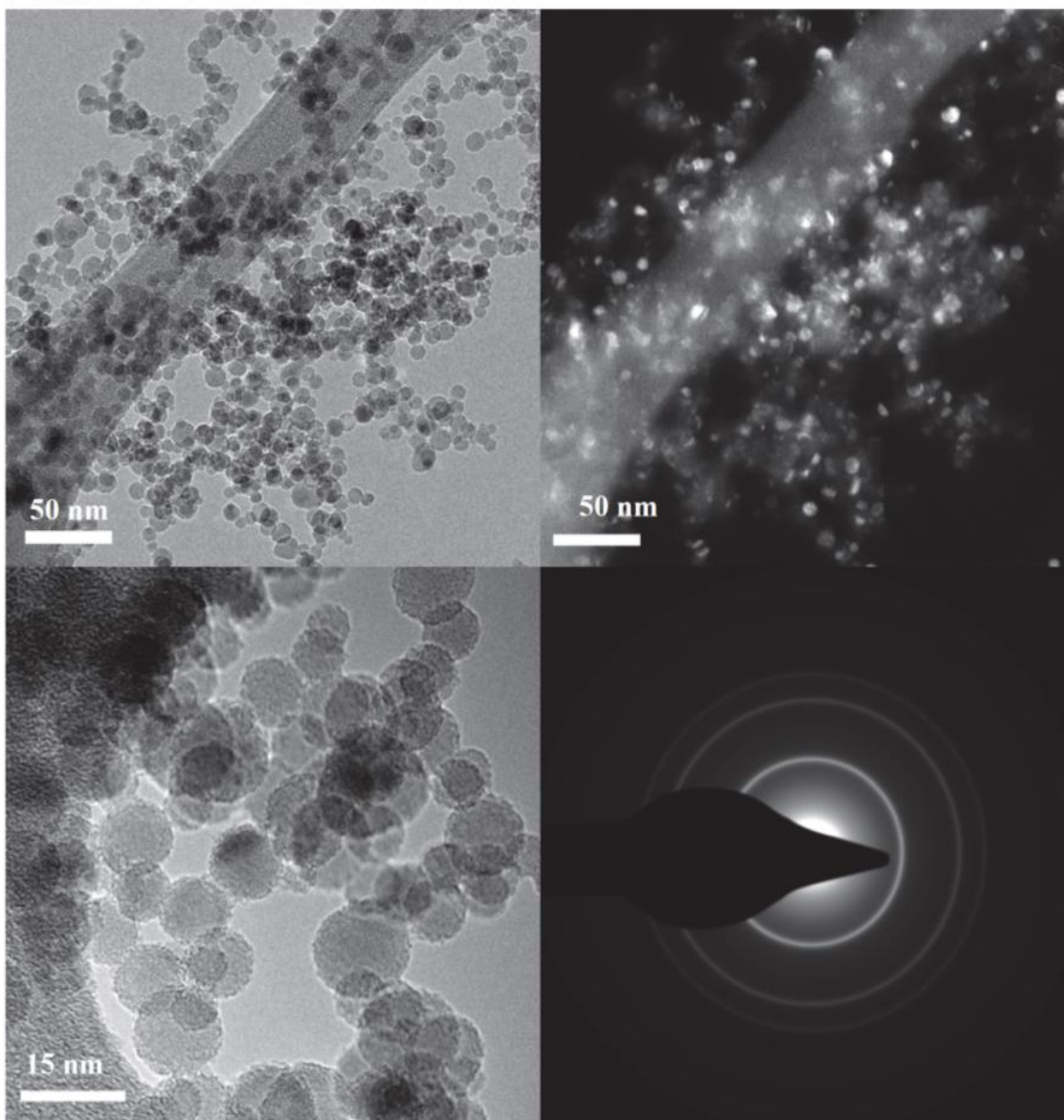

Figure A.7. (a) Bright-field TEM micrograph of particles produced under the conditions of ‘sample A’ (see Table 1) and annealed at 830°C. (b) Dark field micrograph corresponding to (a). (c) Higher magnification micrographs, fringes from the [111] lattice planes are clearly visible. (d) Selected-area diffraction pattern generated using a low-magnification image, so that a large number of particles interact with the electron beam. Rings from the [111], [220] and [311] lattice planes are clearly distinguishable. These images support the conclusion that a very large fraction of the particles have a crystalline structure.

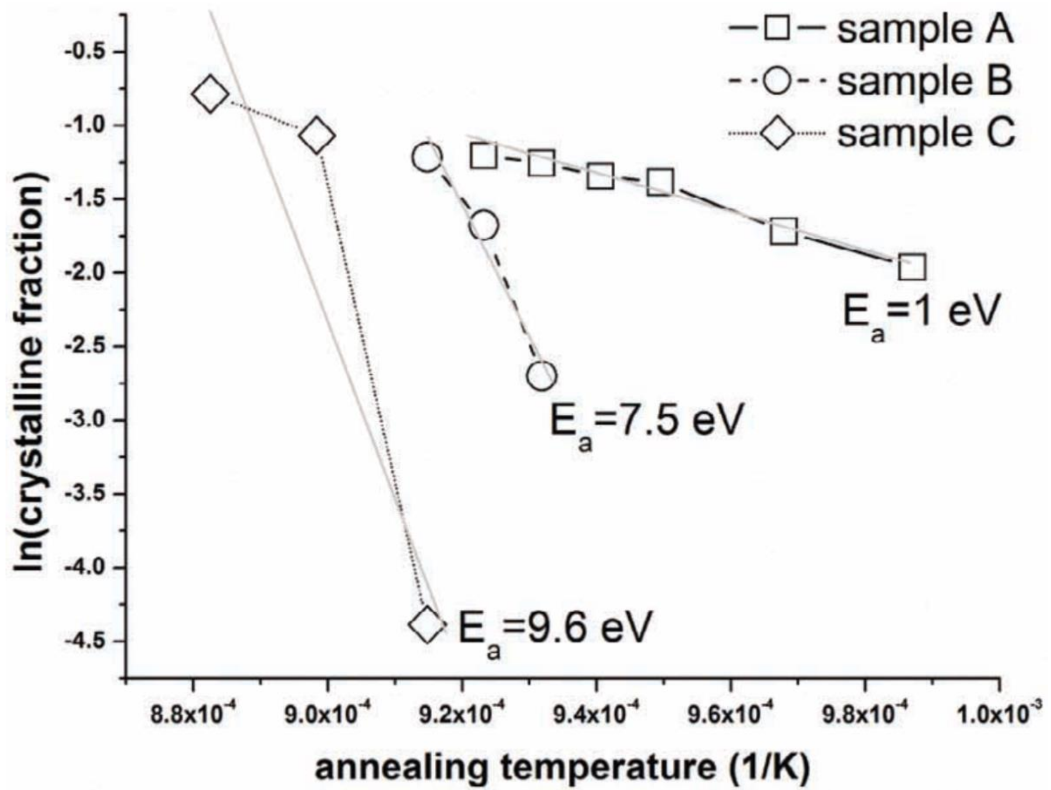

Figure A.8. Arrhenius plot based on the data of figure 5. The activation energy for crystallization is 1 eV for the smaller particle size ranges (see table 2.1), and rapidly increases to 7.5 eV and 9.6 eV for increasingly larger sizes.

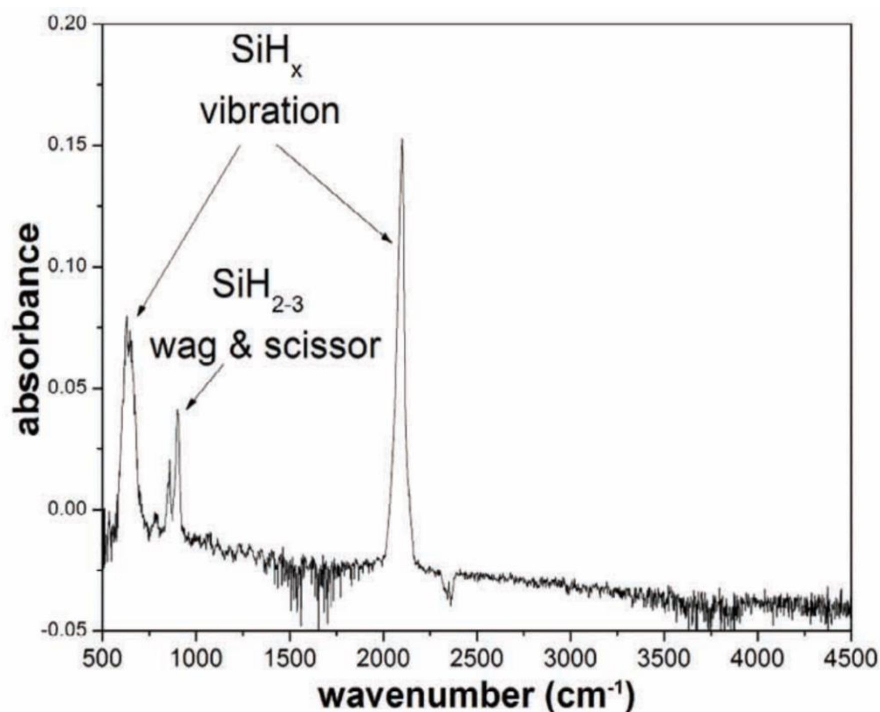

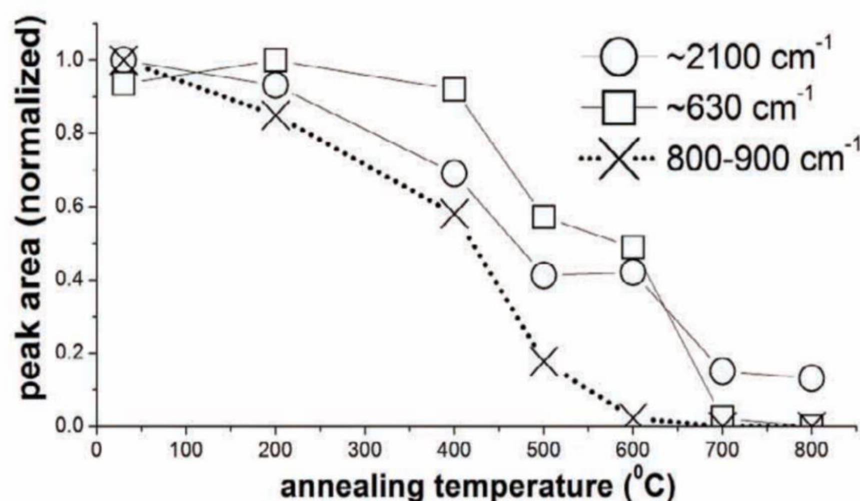

Figure A.9. (top) FTIR absorbance from the plasma produced silicon nanoparticles, produced under the conditions of 'sample A' (see table 2.1) and without any in-flight annealing, as measured *in-situ* before air exposure. (bottom) Variation of the area under the ~2100 cm^{-1} peak, the ~630 cm^{-1} peak and the 800-900 cm^{-1}peaks with respect of the in-flight annealing temperature. The ~2100 cm^{-1} and the ~630 cm^{-1} peaks arise from SiH_x vibrational modes (x=1,2,3) while the 800-900 cm^{-1} peaks arise from SiH_2 and SiH_3 wag and scissor mode. Signal from the 800-900 cm^{-1} peaks diminishes faster than the signal from the ~2100 cm^{-1} and the ~630 cm^{-1} peaks, because of the lower thermal stability of higher surface hydrides.

A.2. Supplemental Equations with explanations for Chapter 2

Equation A.1 RWL

$$I(\omega) = A \cdot \int_0^1 \frac{\exp\left(-q^2L^2/4\right)q^2}{\left[\omega - \omega(q)\right]^2 + \left(\Gamma_c/2\right)^2} dq$$

Where $\omega(q) = \omega_c \cdot (1 - 0.23 \cdot q^2)$, q is the non-demensional wavwnumber, ω is the frequency (in units of cm^{-1}), ω_c = 521 cm^{-1}, L is the non-demensional nanoparticle size and is equal to d/a_0, with d = particle size in nanometers, and a_0 is the lattice constant (0.543 nm for Si). Γ_c is the natural line width for Si at room temperature (4.6 cm^{-1}). A is a scaling factor and a fitting parameter, together with the particle size.

Equation A.2 Paillard

$$I(\omega) = A \cdot \int_{-0.5}^{0.5} \frac{\sin^2(\pi q L) / (1 - q^2 L^2)}{[\omega - \omega(q)]^2 + \left(\Gamma_c / 2 \right)^2} dq$$

Where $\omega(q) = \sqrt{\omega_c^2 - {126100 \cdot q^2} / {|q| + 0.53}}$, q is the non-demensional wavenumber, ω is frequency (in units of cm^{-1}), ω_c= 521 cm^{-1}, , L is the non-demensional nanoparticle size and is equal to d/a_0, with d = particle size in nanometers, and a_0 is the lattice constant (0.543 nm for Si). Γ_c is the natural line width for Si at room temperature (4.6 cm^{-1}). A is a scaling factor and a fitting parameter, together with the particle size.

Equation A.3 Faraci

$$I(\omega) = A \cdot \int_{2\cdot\pi-1}^{2\cdot\pi+1} \frac{\sin\left(\frac{q}{2}\right) \Big/ q\cdot\left(4\cdot\pi^2 - q^2\right)}{\left[\omega - \omega(q)\right]^2 + \left(\frac{\Gamma_c}{2}\right)^2} dq$$

Where $\omega(q) = \sqrt{171400 + 100000 \cdot \left(q \cdot L/_4\right)}$, q is the non-demensional wavenumber, ω is frequency (in units of cm^{-1}), ω_c= 521 cm^{-1}, , L is the non-demensional nanoparticle size and is equal to $d/_{a_0}$, with d = particle size in nanometers, and a_0 is the lattice constant (0.543 nm for Si). Γ_c is the natural line width for Si at room temperature (4.6 cm^{-1}). A is a scaling factor and a fitting parameter, together with the particle size.